THE EFFECTS OF POST-ANNEALING PROCESS ON THE PHYSICAL PROPERTIES OF SILVER-INDIUM-SELENIUM TERNARY SEMICONDUCTOR THIN FILMS DEPOSITED BY ELECTRON BEAM TECHNIQUE

A THESIS SUBMITTED TO
THE GRADUATE SCHOOL OF NATURAL AND APPLIED SCIENCES
OF
MIDDLE EAST TECHNICAL UNIVERSITY

BY

TAHİR ÇOLAKOĞLU

IN PARTIAL FULFILLMENT OF THE REQUIREMENTS
FOR
THE DEGREE OF DOCTOR OF PHILOSOPHY
IN
PHYSICS

AUGUST 2009

Approval of the thesis:

THE EFFECTS OF POST-ANNEALING PROCESS ON THE PHYSICAL PROPERTIES OF SILVER-INDIUM-SELENIUM TERNARY SEMICONDUCTOR THIN FILMS DEPOSITED BY ELECTRON BEAM TECHNIQUE

submitted by **TAHİR ÇOLAKOĞLU** in partial fulfillment of the requirements for the degree of **Doctor of Philosophy in Physics Department, Middle East Technical University** by,

Prof. Dr. Canan Özgen
Dean, Graduate School of **Natural and Applied Sciences** ____________________

Prof. Dr. Sinan Bilikmen
Head of Department, **Physics** ____________________

Prof. Dr. Mehmet Parlak
Supervisor, **Physics Dept., METU** ____________________

Examining Committee Members

Prof. Dr. Çiğdem Erçelebi
Physics Dept., METU ____________________

Prof. Dr. Mehmet Parlak
Physics Dept., METU ____________________

Prof. Dr. Bahtiyar Salamov
Physics Dept., Gazi University ____________________

Prof. Dr. Raşit Turan
Physics Dept., METU ____________________

Assoc. Prof. Dr. Caner Durucan
Metallurgical and Materials Engineering Dept., METU ____________________

Date: August 26th, 2009

I hereby declare that all information in this document has been obtained and presented in accordance with academic rules and ethical conduct. I also declare that, as required by these rules and conduct, I have fully cited and referenced all material and results that are not original to this work.

Name, Last name : Tahir Çolakoğlu

Signature :

ABSTRACT

THE EFFECTS OF POST-ANNEALING PROCESS ON THE PHYSICAL PROPERTIES OF SILVER-INDIUM-SELENIUM TERNARY SEMICONDUCTOR THIN FILMS DEPOSITED BY ELECTRON BEAM TECHNIQUE

Çolakoğlu, Tahir
Ph.D., Department of Physics
Supervisor : Prof. Dr. Mehmet Parlak

August 2009, 148 pages

Ternary chalcopyrite compounds are the semiconductors with suitable properties to be used as absorber materials in thin film solar cells. $AgInSe_2$ is a promising candidate with its several advantages over the widely used $CuInSe_2$. The purpose of this study was to optimize the physical properties of the Ag-In-Se (AIS) thin films that were deposited by e-beam evaporation of $Ag_3In_5Se_9$ single crystal powder for solar cell applications by means of post-annealing process under nitrogen atmosphere.

The as-grown AIS thin films were annealed at 200, 300 and 400°C and their structural, optical, electrical and photoelectrical properties were examined to observe the effects of post-annealing process. Structural characterization of the films was performed by X-ray diffraction (XRD), energy dispersive X-ray spectroscopy (EDS), X-ray photoelectron spectroscopy (XPS) and atomic force microscopy (AFM) analyses. Optical properties of the films were investigated by optical transmittance measurements. Electrical and photoelectrical properties of the films were examined by temperature dependent conductivity, photoconductivity under different illumination intensities and spectral photoresponse measurements.

It was discovered that the annealing of AIS thin films at 200°C resulted in the best physical properties for solar cell applications. The obtained films were polycrystalline with mixed binary and ternary crystalline phases, such as $Ag_3In_5Se_9$, $AgInSe_2$ and InSe, and showed n-type conductivity with room temperature conductivity value of $2.3\text{x}10^{-6}$ $(\Omega\ \text{cm})^{-1}$. The band gap energy of the 200°C-annealed films was determined as 1.68 eV from spectral photoresponse measurements.

The results of the study revealed that the inadequate Ag incorporation and segregation and/or reevaporation of Se atoms at high annealing temperatures were the major problems encountered in producing single phase polycrystalline $AgInSe_2$ thin films. The required stoichiometry of thin films should be maintained during the growth of the films by means of an alternative deposition procedure and the films should be selenized during post-annealing process.

Keywords: Ternary Semiconductor Compounds, Silver Indium Selenide, Solar Cell, Annealing, Optical Absorption, Electrical Conduction Mechanisms, Photoconduction

ÖZ

ÜRETİM SONRASI TAVLAMA İŞLEMİNİN ELEKTRON DEMETİ TEKNİĞİYLE BÜYÜTÜLEN GÜMÜŞ-İNDİYUM-SELENYUM ÜÇLÜ YARIİLETKEN İNCE FİLMLERİN FİZİKSEL ÖZELLİKLERİNE ETKİLERİ

Çolakoğlu, Tahir
Doktora, Fizik Bölümü
Tez Yöneticisi : Prof. Dr. Mehmet Parlak

Ağustos 2009, 148 sayfa

Üçlü kalkopirit bileşikler, ince film güneş pillerinde soğurucu malzeme olarak kullanılmaya uygun yarıiletkenlerdir. $AgInSe_2$, geniş ölçüde kullanılan $CuInSe_2$'e göre avantajları sayesinde gelecek vadeden aday bir malzemedir. Bu çalışmanın amacı, $Ag_3In_5Se_9$ tek kristalinin elektron demeti ile buharlaştırılmasıyla üretilen Ag-In-Se (AIS) ince filmlerin fiziksel özelliklerinin, azot atmosferi altında üretim sonrası tavlama işlemine tabi tutularak güneş pili uygulamaları için optimize edilmesidir.

Üretilen AIS ince filmler, 200, 300 ve 400°C'lerde tavlanmış olup yapısal, optik, elektriksel ve fotoelektrik özellikleri, üretim sonrası tavlama işleminin etkilerini gözlemlemek için incelenmiştir. Filmlerin yapısal karakterizasyonu, X-ışını kırınımı (XRD), enerji dağılımlı X-ışını spektroskopisi (EDS), X-ışını fotoelektron spektroskopisi (XPS) ve atomik kuvvet mikroskopisi (AFM) analizleri sayesinde gerçekleştirilmiştir. Filmlerin optik özellikleri, optik geçirgenlik ölçümleriyle incelenmiştir. Filmlerin elektriksel ve fotoelektriksel özellikleri ise, sıcaklık bağımlı iletkenlik, farklı aydınlık şiddetleri altında fotoiletkenlik ve spektral fototepki ölçümleri ile incelenmiştir.

Güneş pili uygulamaları için en iyi fiziksel özelliklerin, AIS ince filmlerin 200°C'de tavlanmasıyla elde edildiği keşfedilmiştir. Elde edilen filmler, $Ag_3In_5Se_9$, $AgInSe_2$ ve InSe gibi ikili ve üçlü kristal fazlarından oluşan polikristal yapıda olup n-tipi elektriksel iletkenlik göstermiştir. 200°C'de tavlanan filmlerin oda sıcaklığı iletkenlik değeri $2.3\text{x}10^{-6}$ $(\Omega\ \text{cm})^{-1}$ olarak ölçülmüştür ve spektral fototepki ölçümleri ile yasak enerji bant aralığı 1.68 eV olarak tespit edilmiştir.

Bu çalışmanın sonuçları, yetersiz Ag katkısının ve yüksek tavlama sıcaklıkları altında Se segregasyonu ve/veya Se geri buharlaşmasının, tek fazlı polikristal $AgInSe_2$ ince filmlerin üretiminde karşılaşılan temel sorunlar olduklarını göstermiştir. İnce filmler için gerekli olan kimyasal oranın, başka bir üretim yöntemi vasıtasıyla sağlanması ve ince filmlerin üretim sonrası tavlama işlemi sırasında selenlenmesi gerekmektedir.

Anahtar Kelimeler: Üçlü Yarıiletken Bileşikler, Gümüş İndiyum Selenür, Güneş Pili, Tavlama, Optik Soğurma, Elektriksel İletim Mekanizmaları, Fotoiletim

To my parents, brother and wife

and

In memory of my dear friends and colleagues

Oben Sezer

and
Mustafa Çimşit

ACKNOWLEDGMENTS

I would like to express my gratitude to Prof. Dr. Mehmet Parlak for his endless patience, understanding, cooperation and support throughout this study and also to his family. It was a great honor and privilege for me to work under his supervision and to share his knowledge and expertise. During the eight years I studied with him, he has always been a father figure to me and I will never forget his helps. I learned every day a new aspect of scientific discipline and collaboration. Through his invaluable guidance I became accustomed to the required skills that an experimentalist should have. I would like to thank to Prof. Dr. Çiğdem Erçelebi and Prof. Dr. Bahtiyar Salamov for their invaluable suggestions and comments during thesis study. The fruitful contributions of Prof. Dr. Raşit Turan and Assoc. Prof. Dr. Caner Durucan are gratefully acknowledged.

I would also like to present my sincere thanks to Yücel Eke for his kind friendship and for the invaluable technical assistance and cooperation I received.

The financial support supplied by The Scientific and Technological Research Council of Turkey under the scholarship for the Doctorate studies is gratefully acknowledged. Also, this study was supported by The Scientific and Technological Research Council of Turkey under the research grants TBAG-HD/104 (105T539) and TBAG-105T136.

I would like to thank to Prof. Dr. Serhat Özder, Dr. M. Çakmak and Dr. S. Çörekçi for the scientific contributions to the study.

I will always be grateful to my dear friends Mustafa Kulakcı, Hayrettin Un, Barış Manav, Koray Yılmaz, Orhan Karabulut and Murat Kaleli for their precious friendship and brotherhood. I would like to express my sincerest appreciation to my dear friends and lab colleagues Haydar Alıcı, Mustafa Huş, Hakan

Karaağaç, İdris Candan, İlker Yıldız and İlker Doğan. I will always cherish the unforgettable, happy and funny memories of my friends in the bodrum where I spent the best days of my life.

With a deep sense of gratitude, I wish to express and present my sincerest thanks to my parents, my brother and my wife Nilüfer for their encouragement, trust, indulgence and full support whenever and wherever I need. I am and will be grateful to them for giving me the required energy, strength and love to achieve this success. I also thank the family members of my dear friend Oben for their interest and support during the work.

I would like to thank all academic and administrative staff of the Department of Physics, especially Mrs. Sevim Aygar, Mrs. Gülşen Parlak and Mrs. Zeynep Eke for everything they have done concerning the time-consuming bureaucratic tasks.

Finally, I would like to thank all whose direct and indirect support helped me completing my thesis in time.

TABLE OF CONTENTS

ABSTRACT iv

ÖZ vi

ACKNOWLEDGMENTS ix

TABLE OF CONTENTS xi

LIST OF TABLES xiv

LIST OF FIGURES xvi

CHAPTERS

1 INTRODUCTION 1

2 THEORETICAL CONSIDERATIONS 6

- 2.1 Introduction 6
- 2.2 Thin Film Solar Cells 6
  - 2.2.1 Chalcopyrite Based Thin Film Solar Cells 7
- 2.3 Material Properties 8
  - 2.3.1 The Chalcopyrite ($A^I B^{III} C_2^{VI}$) Structure 8
  - 2.3.2 The $Ag_3In_5Se_9$ Structure 12
  - 2.3.3 Electronic Band Structure of $AgInSe_2$ 14
- 2.4 Optical Properties of Semiconductors 15
  - 2.4.1 Optical Constants of Semiconductors 15
    - 2.4.1.1 The Refractive Index and Extinction Coefficient 16
    - 2.4.1.2 Dispersion Relations of Refractive Index 17
  - 2.4.2 Fundamental Absorption in Semiconductors . . . 18
    - 2.4.2.1 Absorption Coefficient 19
- 2.5 Electrical Transport Properties of Semiconductors 23
  - 2.5.1 Electrical Transport Properties in Polycrystalline Semiconductors 25

2.5.1.1 Thermionic Emission of Carriers . . . 27
2.5.1.2 Tunneling 30
2.5.1.3 Hopping Charge Transport 31
2.5.2 Electrical Transport Properties in Amorphous Semiconductors 36
2.6 Photoconductivity in Semiconductors 38
2.6.1 Two-center Recombination Model 39
2.6.2 The Photoconductivity in Chalcogenide Semiconductors 40
3 EXPERIMENTAL TECHNIQUES 43
3.1 Introduction 43
3.2 The Deposition Process of Ag-In-Se Thin Films 44
3.2.1 Substrate Preparation 44
3.2.1.1 Substrate Cleaning 44
3.2.2 Thin Film Geometry 45
3.2.3 Electron Beam Deposition Technique 46
3.3 Post-Annealing Process 50
3.4 Structural Characterization of Thin Films 51
3.4.1 Thickness Measurements 51
3.4.2 X-ray Photoelectron Spectroscopy (XPS) 52
3.4.3 X-ray Diffraction (XRD) 53
3.4.4 Energy Dispersive X-ray Spectroscopy (EDS) . . 54
3.4.5 Atomic Force Microscopy (AFM) 55
3.5 Optical Characterization of Thin Films 55
3.6 Electrical and Photoelectrical Characterization of Thin Films 56
3.6.1 Resistivity Measurements 59
3.6.2 Photoconductivity Measurements 62
3.6.3 Spectral Photoresponse Measurements 63
4 RESULTS AND DISCUSSIONS 65
4.1 Introduction 65
4.2 Structural Characterization of Ag-In-Se Thin Films 65
4.2.1 XRD and EDS Measurements 65
4.2.2 XPS Measurements 72

- 4.2.3 AFM Measurements 81
- 4.2.4 Thickness Measurements 82
- 4.3 Optical Characterization of Ag-In-Se Thin Films 84
  - 4.3.1 Optical Constants of Ag-In-Se Thin Films 86
  - 4.3.2 Dispersion Relations of Refractive Indices for Ag-In-Se Thin Films 90
  - 4.3.3 Fundamental Optical Absorption in Ag-In-Se Thin Films 95
- 4.4 Electrical Characterization of Ag-In-Se Thin Films 100
  - 4.4.1 Temperature Dependent Dark Conductivity Measurements 101
    - 4.4.1.1 Electrical Transport Properties of As-grown AIS Thin Films 102
    - 4.4.1.2 Electrical Transport Properties of AIS Thin Films Annealed at 200°C 109
- 4.5 Photoelectrical Characterization of Ag-In-Se Thin Films . 113
  - 4.5.1 Temperature Dependent Photoconductivity . . . 113
  - 4.5.2 Temperature Dependent Spectral Photoresponse 123
- 5 CONCLUSIONS 132

REFERENCES 138

VITA 147

LIST OF TABLES

TABLES

Table 2.1 The experimentally determined structural and electronic parameters of some $A^IB^{III}C_2^{VI}$-type chalcopyrite semiconductors . . . 11

Table 2.2 Experimentally determined valence band parameters of some $A^IB^{III}C_2^{VI}$ crystals. E_A, E_B and E_C are the energy band gaps from the tops of valence band split to the single conduction band. The Δ_{cf} and Δ_{so} are the amounts of valence band splits due to tetragonal crystalline field and spin-orbit interaction, respectively 12

Table 3.1 Combination of the measured potential differences with respect to the switch positions and applied currents between contact pairs in the resistivity measurements performed by means of the experimental setup shown in Fig. 3.7. 61

Table 4.1 The results of quantitative EDS analysis for the $Ag_3In_5Se_9$ single crystal source and the AIS thin films 67

Table 4.2 The structural parameters calculated by means of computer software Treor90 for the $Ag_3In_5Se_9$ single crystals used as a powder source to deposit the thin films 68

Table 4.3 Decomposition parameters of In 4d photoelectron peak with respect to $4d_{5/2}$ line 76

Table 4.4 Decomposition parameters of In 3d photoelectron peak with respect to $3d_{5/2}$ line 76

Table 4.5 Decomposition parameters of Ag 3d photoelectron peak with respect to $3d_{5/2}$ line 81

Table 4.6 Decomposition parameters of Se 3d photoelectron peak with respect to $3d_{5/2}$ line 81

Table 4.7 The calculated values of refractive index by both EM and CWT methods, extinction coefficient, real and imaginary parts of dielectric constant at 850 nm for the AIS thin films. Cauchy fitting parameters for the dispersion spectra of n for as-grown and annealed AIS thin films. The n, k, ϵ_{re}, ϵ_{im} values were calculated within an accuracy of 2% due to the systematic measurement error of the spectrophotometer 91

Table 4.8 Physical parameters obtained by single oscillator model for as-grown and annealed AIS thin films at different temperatures 95

Table 4.9 Band tail energy width values and the quasicubic model parameters related with the valence band splitting for the as-grown and annealed AIS thin films. The E_{g1}, E_{g2} and E_{g3} values were calculated within an accuracy of 0.03 eV due to inaccuracy in thickness of the films and systematic measurement error 100
Table 4.10 The room temperature conductivity values and the calculated activation energies E_a of the AIS thin films 102
Table 4.11 The calculated values of the pre-exponential factors in the conductivity relations at different temperature regions given in Eqn. 4.20, Eqn. 4.21, Eqn. 4.30, Eqn. 4.31, and Eqn. 4.22, respectively, by using the obtained experimental data for as-grown and annealed AIS thin films at 200°C. 108
Table 4.12 The Mott's parameters calculated by means of Mott's variable range hopping theory for the as-grown and 200°C-annealed AIS thin films in the temperature range of 100-200 K with an average T of 150 K. 108
Table 4.13 The calculated activation energies from temperature dependent photoconductivity measurements for the as-grown and 200°C-annealed AIS thin films. For all types of thin films there are two distinct activation energies at moderate temperature region calculated under the names of E_{β_1} and E_{β_2}. The activation energies for the last two light intensities are calculated from fitting parameters of Fig. 4.30(a) and (b). 117
Table 4.14 The photosensitivity values for AIS thin films under the light flux of 113 mW cm^{-2} at 100 K and room temperature, together with the evaluated trap energy levels with respect to the conduction band. 117
Table 4.15 The band gap energy values and the calculated parameters of the quasicubic model for as-grown AIS thin films 126

LIST OF FIGURES

FIGURES

Figure 2.1 Simplified energy band diagram of a typical p-n heterojunction solar cell (a) at thermal equilibrium in dark and (b) under illumination, open circuit condition. 7

Figure 2.2 Schematic view of a typical chalcopyrite based thin film solar cell structure. Mo is used as a nontransparent back contact, $CuInGaSe_2$ thin film is the p-type absorber material, CdS thin film is used to serve as the window layer and at the top of the structure Indium Tin Oxide layer is deposited as a transparent front contact. . 8

Figure 2.3 The tetragonal unit cell structure for the $AgInSe_2$ chalcopyrite crystal. Each Ag and In atoms are tetrahedrally coordinated to four Se atoms. 9

Figure 2.4 A fragment of $AgInSe_2$ chalcopyrite crystal structure as viewed towards the (110) plane. The solid lines draw the tetragonal unit cell. 10

Figure 2.5 Electronic energy-band structure of $AgInSe_2$ calculated by the empirical pseudopotential method (EPM). The vertical arrows indicate the main interband optical transitions. 14

Figure 2.6 Schematic diagram for (a) a direct transition of excited electrons by photon absorption from the valence band (VB) to the conduction band (CB) and (b) an indirect transition of an excited electron by a photon absorption accompanied by phonon emission (solid arrow with tail) or absorption (dashed arrow with tail) from the VB to CB. 19

Figure 2.7 A typical variation of absorption coefficient as a function of incident photon energy in non-crystalline semiconductors. In region A and B, the optical absorption process is due to the absorption of photons having energy less than band gap between tail and tail states and between tail and extended states, respectively. In region C, the transitions occur between the VB and CB. 23

Figure 2.8 The schematic illustration of the bending in the conduction band of a polycrystalline semiconductor in the vicinity of a grain boundary. 26

Figure 2.9 The schematic representation of hopping transition between two localized states i and j with respective energies E_i and E_j. The Ψ_i and Ψ_j, which are shown as solid and dashed line respectively, correspond to localized wavefunctions of carriers and γ is the localization radius. 32
Figure 2.10 The schematic illustration for two alternative hopping transitions between occupied (circles with solid lines) and empty (solid lines) states. The transitions 1 and 2 correspond to the nearest-neighbor hopping and the variable-range hopping transport of the carriers, respectively. 35
Figure 2.11 The schematic drawing of density of states (DOS) distribution function for a typical amorphous semiconductor. 37
Figure 2.12 The schematic drawing of the characteristic temperature dependence of the photoconductivity of a chalcogenide semiconductor, which has three characteristic temperature portions. 41

Figure 3.1 Shadow mask shapes for (a) thin film production in van der Pauw (Maltese cross) geometry and (b) metal contact production for thin films grown in van der Pauw geometry 46
Figure 3.2 Illustration of an electron beam evaporation source. 1. Hearth, 2. water cooling, 3. magnetic field, 4. accelerated and focused electron beam, 5. solid source of evaporation and 6. the evaporating source. 48
Figure 3.3 Detailed illustration of the electron beam evaporation system utilized for the deposition of AIS thin films. 1. Stainless steel bell jar, 2. sample (substrate) holder, 3. thickness monitor crystal, 4. window, 5. feedtrough, 6. air valve, 7. pirani and penning gauge, 8. rotary pump, 9. e-beam deflection control unit, 10. hearth, 11. water cooling, 12. turbomolecular pump, 13. feedtrough, 14. e-gun, 15. shutter, 16. substrate heater and 17. thermocouple. 49
Figure 3.4 The sketch of the setup for post annealing process of AIS thin films. 1. Pyrex glass jar, 2. thermocouple, 3. hot plate and 4. thin film sample. 51
Figure 3.5 Thin film thickness measurement by means of a diamond stylus of DEKTAK 6M profilometer. R is the radius of curvature of the stylus head, which is 12.5 μm in our measurements, and arrow shows the direction of motion of the stylus during measurement. 52
Figure 3.6 The illustration of the Janis liquid nitrogen, sample-in-vacuum type cryostat. 57
Figure 3.7 Schematic diagram of the experimental setup for resistivity measurements of AIS thin films by means of van der Pauw method. . 60
Figure 3.8 The schematic diagram of the experimental setup for the spectral photoresponse measurements of AIS thin films. All measurement devices and monochromator are controlled by a computer. 1. Concave mirror inside which a halogen lamp exists, 2. collimating lense, 3. shutter, 4. thin film sample and 5. Janis cryostat. 63

Figure 3.9 The power spectrum of the light reaching the thin film samples after passing through the optical setup of spectral photoresponse measurements. 64

Figure 4.1 The EDS pattern of the as-grown Ag-In-Se thin films. 66

Figure 4.2 The XRD diffractogram of the $Ag_3In_5Se_9$ single crystal used as the evaporation source material. 67

Figure 4.3 The XRD patterns of the as-grown and annealed AIS thin films at different temperatures. 69

Figure 4.4 The XRD patterns of the multi-phase AIS thin film structure after annealing at a) 200, b) 300 and c) 400°C. 70

Figure 4.5 XPS spectrum of e-beam evaporated as-grown AIS thin film. . 73

Figure 4.6 The XPS spectra of the as-grown and annealed AIS thin films at different temperatures. 73

Figure 4.7 In 4d core level XPS spectra for a) as-grown AIS thin films and annealed at b) 200°C, c) 300°C and d) 400°C. The squares are the experimental data, the black solid line represents the resulting best fit. 75

Figure 4.8 In 3d core level XPS spectra for a) as-grown AIS thin films and annealed at b) 200°C, c) 300°C and d) 400°C. The squares are the experimental data, the black solid line represents the resulting best fit. 78

Figure 4.9 Ag 3d core level XPS spectrum for as-grown AIS thin films. The squares are the experimental data, the black solid line represents the resulting best fit. 79

Figure 4.10 Se 3d core level XPS spectra for a) as-grown and annealed AIS thin films at b) 200°C. The squares are the experimental data, the black solid line represents the resulting best fit. 80

Figure 4.11 The AFM images of a) the as-grown and annealed AIS thin films at b) 200, c) 300 and d) 400°C. 83

Figure 4.12 Optical transmission spectra for as-deposited and annealed AIS thin films. 85

Figure 4.13 A typical optical transmission spectrum for as-grown AIS thin films with the constructed envelope curves. 87

Figure 4.14 Plots of the refractive index obtained by (a) EM and fitted by Cauchy dispersion equation (solid line) and (b) CWT method (solid line) vs. incident photon energy for as-grown and annealed AIS thin films. 89

Figure 4.15 Dispersion spectra of the real part of the complex dielectric function for the as-grown and annealed AIS thin films at different annealing temperatures. 93

Figure 4.16 Plots of $(n^2 - 1)^{-1}$ vs. $(h\nu)^2$ for as-grown and annealed AIS thin films at 200 and 300°C. 94

Figure 4.17 (a) The semi-logarithmic plot of the absorption coefficient on the incident photon energy for the a typical AIS thin film. The dotted lines represents the borders for Urbach region. The designated points A, B and C show absorption shoulders (local maxima) in the high absorption region. (b) The variation of $Ln(\alpha)$ vs. $(h\nu)$ for the as-grown and annealed AIS thin films. 97
Figure 4.18 The variation of $(\alpha h\nu)^2$ as a function of incident photon energy for (a) as-grown, (b) 200°C-annealed, (c) 300°C-annealed and (d) 400°C-annealed AIS thin films. 99
Figure 4.19 The variation of conductivity as a function of the inverse absolute temperature for the AIS thin films at different annealing temperatures. 101
Figure 4.20 Linearly fitted parts of (a) the plot of Ln(σ) vs. 1000/T variation and (b) the plot of Ln($\sigma T^{1/2}$) vs. T$^{-1/4}$ variation for the as-grown AIS thin films. 104
Figure 4.21 Linearly fitted parts of (a) the plot of Ln($\sigma T^{1/2}$) vs. 1000/T variation, (b) the plot of σ vs. T^2 variation, and (c) the plot of Ln($\sigma T^{1/2}$) vs. T$^{-1/4}$ variation in order to reveal the dominant conduction mechanisms at different temperature regions for AIS thin films annealed at 200°C. 110
Figure 4.22 The variations of the dark conductivity (σ_{Dark}) and the conductivity under illumination (σ_{ϕ}) as a function of inverse absolute temperature for the AIS thin films in both (a) as-grown and (b) 200°C-annealed forms. 114
Figure 4.23 The variation of $\Delta\sigma$ for constant applied electric field of 105 V/cm as a function of inverse absolute temperature at different light intensities for (a) as-grown and (b) 200°C-annealed AIS thin films. . . 116
Figure 4.24 The variation of the photosensitivity as a function of inverse absolute temperature at different light intensities for (a) as-grown and (b) 200°C-annealed AIS thin films. 121
Figure 4.25 The photocurrent-illumination intensity behaviors at different temperatures for (a) as-grown and (b) 200°C-annealed AIS thin films. 122
Figure 4.26 The normalized photocurrent response of the AIS thin films both as-grown and 200°C-annealed at 300 K with the applied electric field strength of 85 V/cm. 126
Figure 4.27 The room temperature spectral distribution of the normalized photocurrent measured under different electric field strengths for the (a) as-grown and (b) 200°C-annealed AIS thin films. 127
Figure 4.28 (a) Energy level diagram for the two discrete traps in the forbidden energy gap of the as-grown AIS thin films and (b) energy band structure of the AIS thin films at Γ point according to allowed transitions. 128
Figure 4.29 The spectral distribution of the normalized photocurrent at different temperatures ranging from 80 to 450 K for (a) as-grown and (b) 200°C-annealed AIS thin films. 129

Figure 4.30 The temperature dependence of photocurrent at different excitation wavelength of incident light with given flux for the (a) as-grown and (b) 200°C-annealed AIS thin films. E_α, E'_α and E''_α are the activation energies discussed in Section 4.5.1. 130

CHAPTER 1

INTRODUCTION

Photovoltaics is the technology that generates electrical energy from semiconductor materials when illuminated with sunlight, through which it is possible to avoid most of the inherent problems assocciated with the current techniques of energy production such as limited availability of energy sources and environmental problems caused by them. Together with these advantages over the conventional techniques, photovoltaics is emerging one of the most powerful alternatives for future mass energy production today especially after the symbolic threshold of 1 GW_p [1] was surmounted in the large-scale production of solar cell modules and almost 3 GW total cumulative power capacity was installed during the year 2004 [2].

Since the first scientific observation of photoconductive property in selenium solid bars in 1873 [3], the extensive scientific studies have been conducted in order to develop efficient solar cell structure to harvest the energy of sunlight. The modern semiconductor photovoltaics started with the production of single crystalline silicon junction solar cells with 6% efficiency in 1954 [4] and developed gradually with an increasing growth speed. Today, about 36% of the semiconductor solar cell production is based on single crystal Si solar cells, 58% of it is based on multicrystalline Si cells, and the remainder is based on thin film solar cell technologies which involve the production of amorphous Si solar cells (4%) and polycrystalline compound solar cells based on CdTe and $CuInSe_2$ (2%) [2]. Although the solar cell production industry is dominated by crystalline Si, the polycrystalline compound solar cells are promising alternatives to replace this

Si-based technology whose main disadvantage lies in the high production cost of electronic grade crystalline Si. Moreover, many polycrystalline thin film semiconductors have such high absorption coefficients that almost all of the photons having higher energy than the forbidden bandgap energy are absorbed within less than 10 μm thin film thickness. On the other hand, the required crystalline Si wafer thickness for the same situation is in between 250-300 μm.

For an efficient solar cell device, an ideal absorber material should meet some specific structural, optical and electrical properties. First of all, the most convenient energy bandgap value should lye in between 1.0 and 1.5 eV. Moreover, the absorber semiconductor material should have high absorption coefficient in the range 10^4 and 10^5 cm^{-1} in the wavelength region of 350-1000 nm. The high quantum efficiency, low recombination rate and long diffusion length for the photo-excited carriers are also required for the ideal thin film compound semiconductor materials [2, 5]. Along with this fact, only a few semiconductor compounds have been the subject of scientific studies and gained the sufficient interest among a large number of compound semiconductor materials because they can satisfy the above-mentioned conditions and are widely available in nature.

I-III-VI$_2$ (I $\equiv$ Ag, Cu; III $\equiv$ In, Ga, Al; VI $\equiv$ S, Se, Te) and I-III$_\mathrm{x}$-III$_{1-\mathrm{x}}$-VI$_2$ ternary and quaternary chalcopyrite semiconductor compounds have proven to attract the technological interest owing to their promises for practical application in the areas of visible and infrared light emitting diodes, infrared detectors, optical parametric oscillators, nonlinear optics, solar cells, optical frequency conversion, second harmonic generation devices and many other electro-optical devices [6–11]. In the production of stable and radiation resistant polycrystalline thin film photovoltaic solar cells, reasonably high power conversion efficiency values have been achieved by using the ternary chalcopyrite semiconductors as an absorber layer [12]. Furthermore, the ability of ternaries to form various solid solutions and to accommodate different dopants has recently led to their emergence as technologically significant materials, including applications in photovoltaic solar cells [13–15]. Their band gaps are ranging from 3.5 eV of $CuAlS_2$ to 1.2 eV of $AgInSe_2$ covering the broad wavelength range from infrared to ultraviolet, which make them attractive materials for light emitting and detector devices [16].

The first all thin-film $CuInSe_2$/CdS heterojunction solar cell device, which had a p-$CuInSe_2$ absorber layer on gold-coated glass substrate and a CdS window layer, was fabricated with an 5.7% efficiency in 1976 [17] and starting from this time, polycrystalline thin film $CuInSe_2$ solar cells began to receive a lot of scientific attention. The main reasons lying behind this interest in these ternary semiconductor compounds are the nature of their chemical structure and the possibility to tune their forbidden bandgap energies [2, 18]. Both the grain boundaries and the film surfaces are intrinsically well passivated that results in a low recombination rate for excess charge carriers due to their chemical structure. Therefore, the low recombination velocity at the grain boundary region makes it possible to attain high solar cell efficiencies even for the polycrystalline thin films having grain sizes of the order of about a μm [18]. Additionally, the bandgap energies can be tailored by chemical methods such as by replacing Se by S and by adding Ga into the structure to form the quaternary phase of $CuIn_xGa_{1-x}Se_2$. In fact, $CuInGaSe_2$ (CIGS) solar cell energy conversion efficiency of more than 19.5% has been already achieved [19].

On the other hand, there are also some problems associated with $CuInSe_2$ (CIS) and CIGS polycrystalline thin films one of which is that Cu atoms sometimes cause shorting effects in photovoltaic devices because of its larger diffusion coefficient [20]. To get rid of this problem in CIS and CIGS structures, Cu has been replaced by Ag and Ga (In) [21]. Additionally, it is observed that the efficiency of the CIGS thin film solar cells decreases as the band gap energy is increased above 1.3 eV by changing the Ga/(In+Ga) ratio in the structure [22]. Alternatively, the $AgInSe_2$ ternary chalcopyrite semiconductors have several advantages over the CIS and CIGS. Specifically, $AgInSe_2$ has a bandgap energy of 1.20 eV, which is wider than that of CIGS [23], and the band gap energy value can be increased up to 1.7 eV by Ga incorporation to form $AgIn_xGa_{1-x}Se_2$ (AIGS) structure [22] and a melting point of 780°C, which is lower than that of CIGS by 200°C and therefore $AgInSe_2$ can have better performance than $CuInSe_2$ for solar cell applications. A solar sell efficiency of 7.5% was reported for the p-$AgInSe_2$/n-CdS solar cell structure where $AgInSe_2$ thin film was used as an absorber material [24]. Moreover, 9% efficient p-$AgInSe_2$/n-Si solar cells were successfully produced by evaporating $AgInSe_2$ single crystal targets through laser deposition technique on n-Si substrates [25]. Furthermore, an efficiency of energy conversion of the solar cell based on $AgIn_{0.5}Ga_{0.5}Se_2$ thin films was obtained as more than 8% [22]. However, the number of scientific studies on polycrystalline $AgInSe_2$ thin films is small in comparison to those of $CuInSe_2$ thin films.

Accordingly, this thesis work was intended to investigate the dependence of the physical properties of Ag-In-Se (AIS) ternary semiconductor thin films deposited by electron beam evaporation on the annealing at different temperatures. The main purpose is to optimize the physical properties of AIS thin films by means of the post-depositional improvement technique, which is annealing under inert gas environment at different temperatures in this thesis, in order to prepare a useful thin film absorber material for solar cell applications. Therefore, in this work, the results of the systematic studies on the structural properties of the thin films grown without intentional doping by electron beam (e-beam) evaporation of $Ag_3In_5Se_9$ single crystal under the high vacuum condition are presented. The structural characterization of the deposited films were analyzed by means of X-ray diffraction (XRD) measurements, X-ray photoelectron spectroscopy (XPS), atomic force microscopy (AFM) and energy dispersive X-ray spectroscopy (EDS). The post-annealing under the nitrogen environment in the temperature range of 100-400°C were studied to deduce the effects of annealing on the structural properties of the thin films. Due to the requirement to have the complete knowledge of the optical constants of thin films over a wide wavelength range; especially for solar cell applications, one of the main aims in this study is to determine the optical properties of e-beam evaporated AIS thin films on glass substrates, both as-grown and annealed samples at different temperatures, through optical transmission measurements. Furthermore, the effect of thermal annealing process at different temperatures under the nitrogen atmosphere on the electrical and electro-optical properties of Ag-In-Se (AIS) thin films was studied by means of temperature dependent conductivity measurements, temperature dependent photoconductivity measurements as a function of illumination intensity and temperature dependent spectral photoresponse measurements over the wavelength (λ) range of 380-1050 nm in the temperature range of 100-450 K.

In the second chapter of the thesis, the theoretical fundamentals required to explain the physical properties of Ag-In-Se (AIS) thin films are presented and in the third chapter, the experimental procedures on the deposition of AIS thin films and the details of the measurement techniques and setups are given and explained. In the chapter four, the structural, optical, electrical and electrooptical properties of the deposited AIS thin films annealed at different temperatures are discussed over the results obtained as a result of the characterization of thin films. Finally, general conclusions and the interpretations of the results are made in the last chapter.

CHAPTER 2

THEORETICAL CONSIDERATIONS

2.1 Introduction

This chapter is intended as a brief presentation of the main physical properties of ternary semiconductor materials containing the respective IB-IIIA-VIA group elements and the basic physics of the theoretical approaches to explain the experimental results obtained by means of rigorous structural, optical and electrical characterization process. Therefore, this chapter is aimed at providing a basic theoretical background for the chapters that follow.

2.2 Thin Film Solar Cells

Solar cells are devices that convert the energy of sunlight into electricity and they consist of a semiconductor forming a rectifying junction either with another semiconductor or with a metal. In other words, the solar cell structure is basically a p-n junction diode or a Schottky diode. Furthermore, p-n junctions can be classified as homojunctions and heterojunctions according to whether the semiconductor materials that form the junction is the same or different.

Photovoltaic energy conversion in a solar cell structure involves two essential steps. In the first step, the semiconductor material absorbs the incoming photons as long as the energy of the photons are larger than that of the band gap of the semiconductor. In this process, the absorbed photons are converted into electron-hole pairs. In the second step, the photogenerated electron-hole pairs are separated by the internal electric field of the junction, thus, electrons drift to one electrode and holes to the other one [26,27]. Fig. 2.1 shows the schematic energy band diagrams of a typical p-n heterojunction solar cell at thermal equilibrium in dark and under illumination.

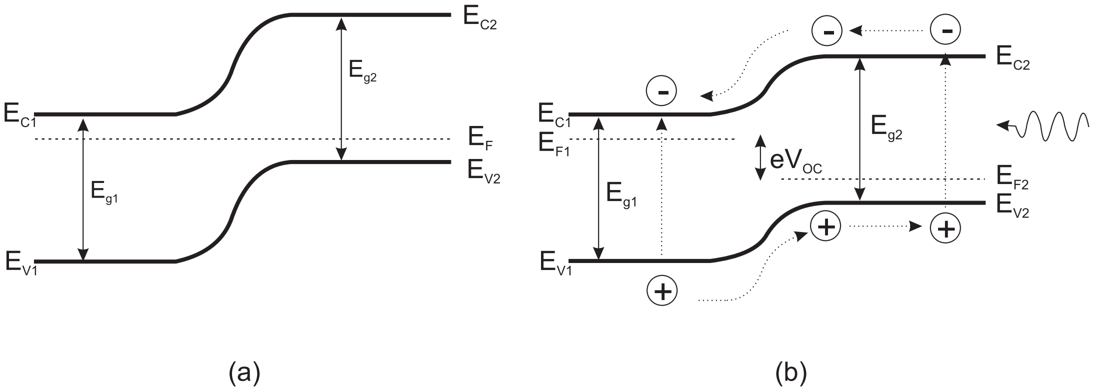

Figure 2.1: Simplified energy band diagram of a typical p-n heterojunction solar cell (a) at thermal equilibrium in dark and (b) under illumination, open circuit condition.

2.2.1 Chalcopyrite Based Thin Film Solar Cells

A typical thin film solar cell structure consists of a number of thin films sequentially deposited onto a rigid or flexible substrate material as shown in Fig. 2.2. The first thin film is expected to serve as a nontransparent back contact. The absorber p-type thin film, which is chalcopyrite semiconductor in this case, is deposited onto the back contact. This absorber thin film absorbs most of the incident sunlight and generates photocurrent. Moreover, the deposition of an n-type thin film, (typically CdS) which serves as a window layer, forms the heterojunction and finally the last thin film to be deposited is n-type wide band gap transparent front contact, which is usually transparent conductive oxide film [28].

The most advanced and widely used absorber materials are $CuInSe_2$-based chalcopyrite semiconductors. In many solar cell applications, $CuInGaSe_2$ thin films are deposited as an absorber layer by Ga incorporation into $CuInSe_2$ chalcopyrite structure in order to obtain optimum band gap energy value.

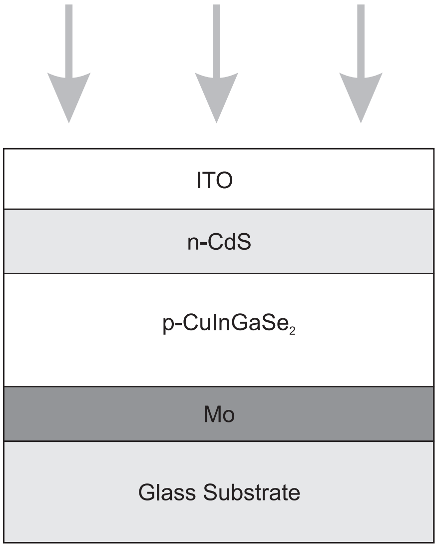

Figure 2.2: Schematic view of a typical chalcopyrite based thin film solar cell structure. Mo is used as a nontransparent back contact, $CuInGaSe_2$ thin film is the p-type absorber material, CdS thin film is used to serve as the window layer and at the top of the structure Indium Tin Oxide layer is deposited as a transparent front contact.

2.3 Material Properties

2.3.1 The Chalcopyrite ($A^I B^{III} C_2^{VI}$) Structure

The chalcopyrite $A^I B^{III} C_2^{VI}$ crystal phase ($A \equiv \mathrm{Cu, Ag}$, $B \equiv \mathrm{Al, Ga, In, Tl}$, and $C \equiv \mathrm{S, Se, Te}$) belongs to the space group $I\bar{4}2d$ with tetragonal unit cell, which includes four formula units of the phase. The name of the phase originates from the mineral chalcopyrite, $CuFeS_2$, whose crystal structure is the prototype for the $A^I B^{III} C_2^{VI}$ crystal structure [6]. In such a structure, each cation atoms, A and B, is tetrahedrally coordinated to four anion atoms, C, while each C atom is tetrahedrally coordinated to two A atoms and two B atoms in an orderly fashion. As implied by the tetrahedral coordination, the bonding among the atoms is dominantly covalent with sp^3 hybrid bonds. However, the ionic contribution to the bonding can not be ignored since atoms are distinct.

The conventional tetragonal unit cell is constructed by the following distribution of the atomic coordinates in unit cell vector basis system;

- 4 A atoms in a positions; $0\ 0\ 0$, $0\ \frac{1}{2}\ \frac{1}{4}$
- 4 B atoms in b positions; $0\ 0\ \frac{1}{2}$, $0\ \frac{1}{2}\ \frac{3}{4}$
- 8 C atoms in d positions; $u\ \frac{1}{4}\ \frac{1}{8}$, $\bar{u}\ \frac{3}{4}\ \frac{1}{8}$, $\frac{3}{4}\ u\ \frac{7}{8}$, $\frac{1}{4}\ \bar{u}\ \frac{7}{8}$

where u is defined as the anion displacement parameter whose ideal value is $\frac{1}{4}$, and the positions $(0\ 0\ 0)$ and $(\frac{1}{2}\ \frac{1}{2}\ \frac{1}{2})$ are equivalent positions. All 16 atomic positions in the unit cell can be obtained by the addition of these equivalent positions to the a,b and d coordinates given above (see Fig. 2.3 and 2.4).

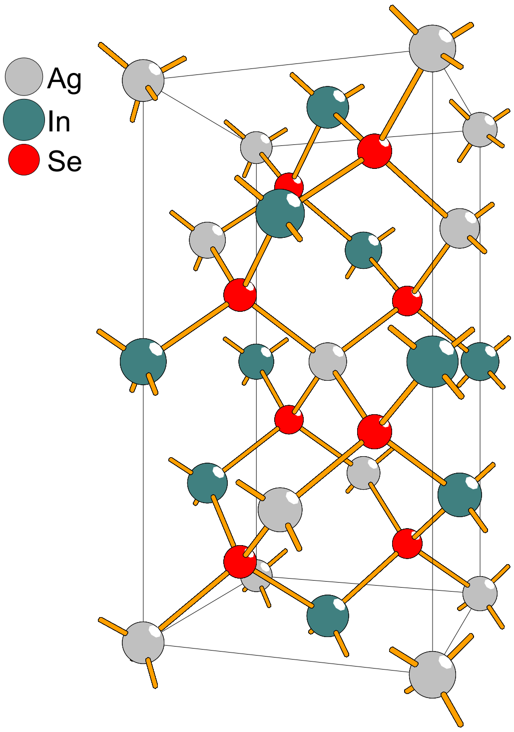

Figure 2.3: The tetragonal unit cell structure for the $AgInSe_2$ chalcopyrite crystal. Each Ag and In atoms are tetrahedrally coordinated to four Se atoms.

The chalcopyrite structure, which has a c/a ratio approximately equal to 2, is perceived as a superlattice of the zincblende structure because the random

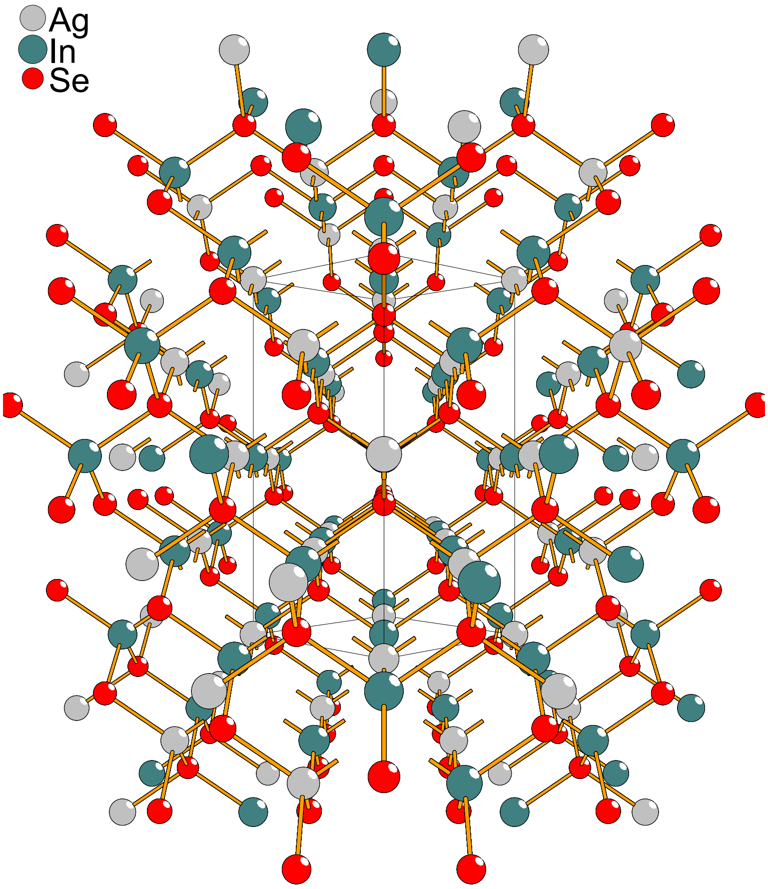

Figure 2.4: A fragment of $AgInSe_2$ chalcopyrite crystal structure as viewed towards the (110) plane. The solid lines draw the tetragonal unit cell.

distribution of the cation atoms, A and B, in the unit cell would result in the cubic zincblende structure [6, 10].

The chalcopyrite $A^{I}B^{III}C_2^{VI}$ semiconductor compounds can be described as the ternary analogs of the $D^{II}C^{VI}$ binary compounds ($D \equiv \mathrm{Zn}, \mathrm{Cd}$). In other words, the ternary crystal structure can be constructed from the binary phases by well-arranged substitution of the other group elements in order to reach the electron-to-atom ratio of 4. Therefore, the tetragonal superlattice is derived from the ordered arrangements of cation atoms in the $D^{II}C^{VI}$ binary structure.

The tetragonal unit cell in a chalcopyrite structure is characterized by a tetragonal distortion along the c-axis, which is caused by ordering and defined as $\eta = c/2a$, and the anion displacement parameter u, which precisely determines the anion atom position. The value of u parameter depends on the difference between the $A-C$ and $B-C$ chemical interactions. Table 2.1 lists some of the known compounds exhibiting chalcopyrite structure and related experimentally obtained structural and electronic parameters for them [6, 29].

Table 2.1: The experimentally determined structural and electronic parameters of some $A^I B^{III} C_2^{VI}$-type chalcopyrite semiconductors

Ternary Phase	a (Å)	c/a	u	E_g (eV)	Reference
$CuAlTe_2$	5.964	1.975	0.250	2.06	[30]
$CuGaSe_2$	5.596	1.966	0.243	1.68	[31]
$CuInSe_2$	5.782	2.009	0.235	1.04	[32]
$AgGaSe_2$	5.985	1.793	0.278	1.83	[32]
$AgInSe_2$	6.090	1.916	0.250	1.24	[30]
$AgGaTe_2$	6.283	1.897	0.260	1.20	[30]

The energy band structure of $A^I B^{III} C_2^{VI}$ semiconductors differs from that of $D^{II} C^{VI}$ zincblende binary compounds in some aspects. The uppermost valence bands of $A^I B^{III} C_2^{VI}$ chalcopyrite semiconductors are seriously influenced by the hybridization of noble metal *d*-levels and anion *p*-levels in the valence band [18, 33–35]. The *p*-*d* hybridization in these chalcopyrite compounds causes the direct energy band gaps to have lower values with respect to those in the $D^{II} C^{VI}$ analogs by amounts up to 1.6 eV. For example, Shay et al. [36] performed an electroreflectance measurement at 77 K as a result of which it was found that the lowest energy band gap of $AgInSe_2$ is 1.24 eV which is around 0.6 eV less than that of the binary analog CdSe.

As a result of several electroreflectance measurements in which the transitions from the *d*-levels to the bottom of the conduction band are observed, the noble metal *d*-levels in the valence band is proved to exist [6].Furthermore, the fivefold degeneracy is completely removed due to the existence of spin-orbit interaction and the tetragonal crystal field. In other words, the removed degeneracy in the valence band leads to the splitting of the valence band structure and the band-to-band transitions are now realized from three closely spaced valence bands to a single conduction band. The experimentally observed valence band parameters of some $A^I B^{III} C_2^{VI}$ semiconductor crystals are tabulated in Table 2.2.

Table 2.2: Experimentally determined valence band parameters of some $A^I B^{III} C_2^{VI}$ crystals. E_A, E_B and E_C are the energy band gaps from the tops of valence band split to the single conduction band. The Δ_{cf} and Δ_{so} are the amounts of valence band splits due to tetragonal crystalline field and spin-orbit interaction, respectively

Ternary Phase	E_A (eV)	E_B (eV)	E_C (eV)	-Δ_{cf} (eV)	Δ_{so} (eV)	Ref.
$CuGaS_2$	2.43	2.55	2.55	0.12	0.00	[37]
$CuGaSe_2$	1.68	1.75	1.96	0.09	0.23	[33]
$CuInSe_2$	1.04	1.04	1.27	-0.006	0.23	[36]
$AgGaSe_2$	1.83	2.03	2.29	0.25	0.31	[38]
$AgInS_2$	1.87	2.02	2.02	0.15	0.00	[36]
$AgInSe_2$	1.24	1.33	1.60	0.12	0.30	[36]

2.3.2 The $Ag_3In_5Se_9$ Structure

As a ternary semiconductor compound $Ag_3In_5Se_9$ belongs to the $A_3^{I}B_5^{III}C_9^{VI}$-type semiconductor family which are the noncubic ternary analogs of $A_2^{III}B_3^{VI}$-type crystalline structures [11]. Along with this fact, these two-cation ternary semiconductor compounds are produced by manipulating the sites of In atoms in the binary analog In_2Se_3 semiconductor crystals together with monovalent Ag atoms, thanks to the distinctive chemical properties of In_2Se_3 [11]. Clearly, the $Ag_3In_5Se_9$ semiconductor compounds having 4.24 electrons per atom [39] are the isostructural derivatives of In_2Se_3 binary compounds with 4.80 electrons per atom which is accomplished by replacing the tetrahedral In cations by Ag atoms [10]. According to the studies, $Ag_3In_5Se_9$ ternary compounds crystallize in hexagonal [40] and tetragonal (chalcopyrite) structure having the lattice constants of $a = 6.714$, $b = 6.714$ and $c = 10.430$ Å with possible space group of either P4 or P4mm (c/a ratio is 1.55) [41]. Density of the single crystals was determined from tetragonal lattice parameters as 5.71 g/cm^3. The relatively low melting point of 825 °C enables the easier preparation of the single crystals and reduces the degree of contamination significantly during growth cycle of the crystal. Furthermore, the low-frequency current oscillations in the temperature range between 77 and 230 K revealed that the $Ag_3In_5Se_9$ crystals include three deep levels situated at 0.12, 0.73 and 1.09 eV below the bottom of the conduction band [42].

The energy band structure of the $Ag_3In_5Se_9$ ternary semiconductor alloy is similar to that of the binary analog In_2Se_3 semiconductor compound [6]. Although the constituent atoms of the $Ag_3In_5Se_9$ ternary compounds are arranged principally in analogy with In_2Se_3 structure, there exist some distinctive aspects of this crystalline structure due to the noncubic crystal structure. One of these aspects is the compression of crystal lattice along the z-axis ($c < 2a$). Another aspect includes the distortion of the anion sites away from symmetrically related positions. Moreover, the arrangement of the two different cations, Ag and In, leads to the doubling of the unit cell in the z-direction [6]. All these structural considerations are proved to be applicable since the calculated forbidden energy band gap in $Ag_3In_5Se_9$ ternary compounds is very close to the energy band gap in the binary analog In_2Se_3 semiconductor compounds which is 1.3 eV, which indicates that the binary-ternary analogy is plausible [43]. Both compounds are direct band gap semiconductors which means the top of the valence bands and the bottom of the conduction bands lie along the Γ-point. The dominant contributions of the noncubic crystalline field associated with the built-in lattice compression and the spin-orbit interaction to the energy band structure of the $Ag_3In_5Se_9$ crystal cause almost the complete removal of the degeneracy of both the p- and d-like valence bands [6,8,10]. Consequently, the valence band structure undergoes only two energy splittings; i) Crystal-field and ii) Spin-orbit splittings of the valence band. In other words, the fundamental absorption edge is characterized by three different interband transitions. The lowest interband transition energies from the valence subbands to the conduction band are experimentally determined by Huseynov et al. [44] as 1.30, 1.41 and 1.80 eV.

2.3.3 Electronic Band Structure of $AgInSe_2$

$AgInSe_2$ is a direct-bandgap semiconductor. Fig. 2.5 shows the calculated electronic energy-band structure of $AgInSe_2$ where the calculations are based on the empirical pseudopotential method (EPM) [45]. The vertical arrows in Fig. 2.5 indicate the locations of the dominant interband optical transitions where $\Gamma = 2\pi/a(0, 0, 0)$, $S = 2\pi/a(1, 0, 0)$, $N = 2\pi/a(1, 1, 0)$, $P = 2\pi(1/a, 1/a, 1/2c)$, and $L = 2\pi(1/a, 0, 1/2c)$.

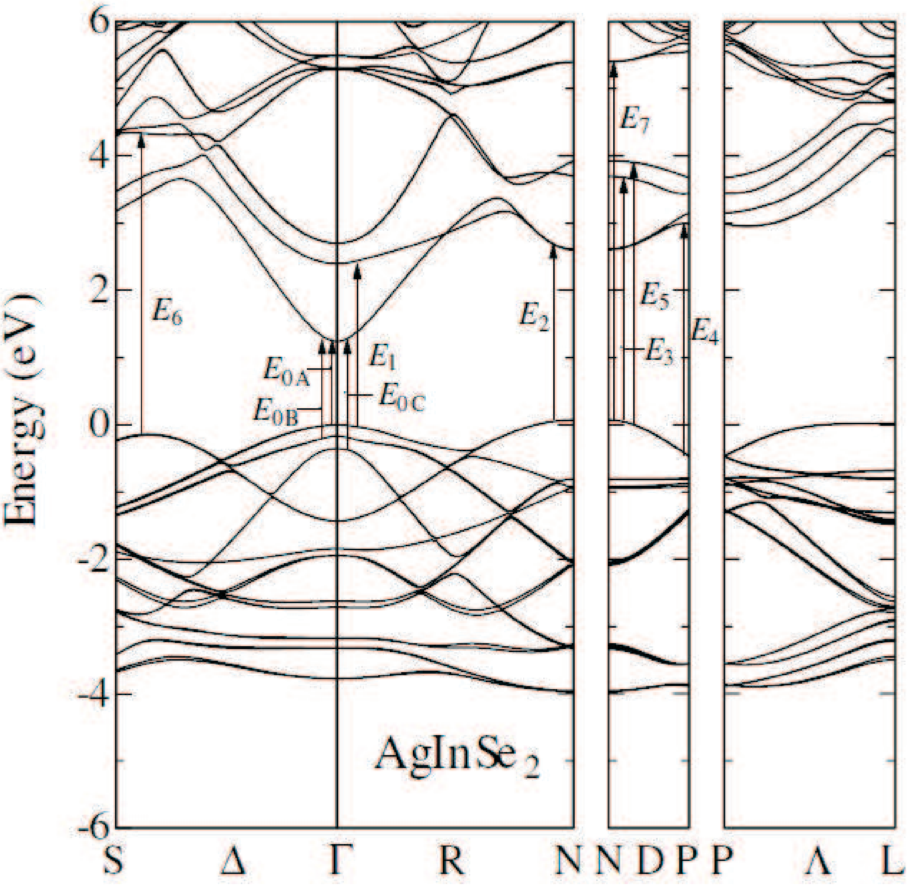

Figure 2.5: Electronic energy-band structure of $AgInSe_2$ calculated by the empirical pseudopotential method (EPM). The vertical arrows indicate the main interband optical transitions.

There are three distinct transitions at Γ-point which are designated as $E_{0\mathrm{A}}$, $E_{0\mathrm{B}}$ and $E_{0\mathrm{C}}$ and the corresponding calculated energy values are 1.24, 1.32 and 1.60 eV, respectively. The optical transition E_1 represents the transition from the highest valence to the second lowest conduction band at the Γ-point. The E_2 transition can be originating from transitions near the N-point. Additionally, The E_3 and E_5 transitions correspond to the transitions at the N-point. Similarly, the transition E_4 is principally at the P- and S-points, while the E_6 transition is the one at the S-point. At higher energy, the E_7 transition is due to the transition at the N- and Γ-points [45].

2.4 Optical Properties of Semiconductors

The characteristics of light when passing through semiconductor materials are influenced by their optical properties, in other words, the propagation vector or intensity of light is modified by the semiconductors. The refractive index (n) and the extinction coefficient (k) corresponding to light intensity attenuation or absorption coefficient (α) are two of the most important optical properties of semiconductors and in general, they are named as *optical constants*. The following subsection will include the theoretical discussions of the complex refractive index, the dispersion relations of n and k or the wavelength dependencies of them and the relations between them.

2.4.1 Optical Constants of Semiconductors

The refractive index of semiconductors as an important optical constant is generally depends on the wavelength of electromagnetic wave and this dependence is expressed by dispersion relations. The complex refractive index corresponds to the materials in which an electromagnetic wave loses energy. In such a complex expression, the real part is the refractive index (n) and the imaginary part is the extinction coefficient (k).

2.4.1.1 The Refractive Index and Extinction Coefficient

The refractive index (n) of an optical or dielectric medium is defined as

$$n = \frac{c}{v} \tag{2.1}$$

where c is the velocity of light in vacuum and v is its velocity in the medium. By using Maxwell's equations and Eqn. 2.1, the Maxwell's famous relation of the refractive index for a material

$$n = \sqrt{\varepsilon\mu} \tag{2.2}$$

where ε is the static dielectric constant or relative permittivity and μ the relative permeability. The refractive index turns into a complex function of wavelength of light when attenuation of intensity of light propagating through a material due to various energy loss mechanisms such as phonon generation, free carrier absorption, scattering etc. occurs. The complex refractive index for nonmagnetic materials is expressed as

$$\tilde{N} = n + ik = \sqrt{\varepsilon} = \sqrt{\varepsilon_{re} + i\varepsilon_{im}} \tag{2.3}$$

where ε_{re} and ε_{im} are the real and imaginary parts of ε, respectively and they can be related to n and k through

$$\varepsilon_{re} = n^2 - k^2 \tag{2.4}$$

$$\varepsilon_{im} = 2nk \tag{2.5}$$

and also n and k are related to ε_{re} and ε_{im} by the expressions

$$n = \sqrt{\frac{1}{2}(\sqrt{\varepsilon_{re}^2 + \varepsilon_{im}^2} + \varepsilon_{re})} \tag{2.6}$$

$$k = \sqrt{\frac{1}{2}(\sqrt{\varepsilon_{re}^2 + \varepsilon_{im}^2} - \varepsilon_{re})} \tag{2.7}$$

respectively. By using the Kramers-Kronig relations between the real and the imaginary parts of ε, the dispersion relation of ε_{re} can be obtained if the frequency ω dependence of ε_{im} is known, and vice versa. The Kramers-Kronig relations for the relative permittivity are given as

$$\varepsilon_{re}(\omega) = 1 + \frac{2}{\pi} P \int_0^\infty \frac{\omega^{'} \varepsilon_{im}(\omega^{'})}{\omega'^2 - \omega^2} d\omega^{'} \tag{2.8}$$

$$\varepsilon_{im}(\omega) = -\frac{2\omega}{\pi} P \int_0^\infty \frac{\varepsilon_{re}(\omega^{'})}{\omega'^2 - \omega^2} d\omega^{'} \tag{2.9}$$

where P is the Cauchy principal value of the integral and the singularity at $\omega^{'} = \omega$ is avoided. Eventually, the complex refractive index is expressed as

$$n(\omega) = 1 + \frac{2}{\pi} P \int_0^\infty \frac{k(\omega^{'})}{\omega^{'} - \omega} d\omega^{'} \tag{2.10}$$

$$k(\omega) = -\frac{2}{\pi} P \int_0^\infty \frac{n(\omega^{'})}{\omega^{'} - \omega} d\omega^{'} \tag{2.11}$$

as long as $n(\omega)$ and $k(\omega)$ obey the f-sum rule [46].

2.4.1.2 Dispersion Relations of Refractive Index

There exist several theoretical models in order to describe the wavelength dependence of refractive index and the most widely used dispersion relations are listed as follows

- ***Cauchy dispersion relation:*** Cauchy's dispersion formula is generally used in the visible region of spectrum for various optical materials and applies to normal dispersion, where n decreases with increasing wavelength λ. The n as a function of λ is given as

  $$n = A + \frac{B}{\lambda^2} + \frac{C}{\lambda^4} + ... \tag{2.12}$$

  where A, B and C are material–specific constants.

- ***Sellmeier dispersion relation:*** Sellmeier equation describes the wavelength dependence of the refractive index as an empirical relation. n is expressed as a function of λ in the form of a series of single-dipole oscillator terms as

$$n^2 = 1 + \frac{A_1\lambda^2}{\lambda^2 - \lambda_1^2} + \frac{A_2\lambda^2}{\lambda^2 - \lambda_2^2} + \frac{A_3\lambda^2}{\lambda^2 - \lambda_3^2} + ... \tag{2.13}$$

where $\lambda_1, \lambda_2, \lambda_3, ...$ and $A_1, A_2, A_3, ...$ are constants and called as Sellmeier coefficients which can be determined by fitting Eqn. 2.13 to the obtained experimental data.

- ***Wemple-DiDomenico dispersion relation:*** Wemple-DiDomenico dispersion equation is a semi-empirical formula derived within the framework of single-oscillator model in order to determine the refractive index values for the photon energies below the interband absorption edge. The relation is given as

$$n^2 = 1 + \frac{E_o E_d}{E_o^2 - (h\nu)^2} \tag{2.14}$$

where E_o is the single-oscillator energy, E_d is the dispersion energy which is a measure of the average strength of interband optical transitions, ν is the frequency of light incident on the material and h is the Planck constant. Although, Eqn. 2.14 gives approximate results, it is widely used by many experimental physicists due to simplicity [46].

2.4.2 Fundamental Absorption in Semiconductors

Fundamental absorption of electromagnetic radiation in semiconductors happens by means of the photoexcitation of an electron from the valence band to conduction band, which is also called as band-to-band absorption of radiation. In such an absorption process, the absorbtion of a photon creates an electron in the conduction band leaving a hole in the valence band. This physical process requires the energy and momentum conservation. There exist two distinct fundamental absorption processes which are called direct and indirect band-to-band transitions in crystalline semiconductors. On the other hand, only direct transitions are favorable and physically meaningful in amorphous semiconductors.

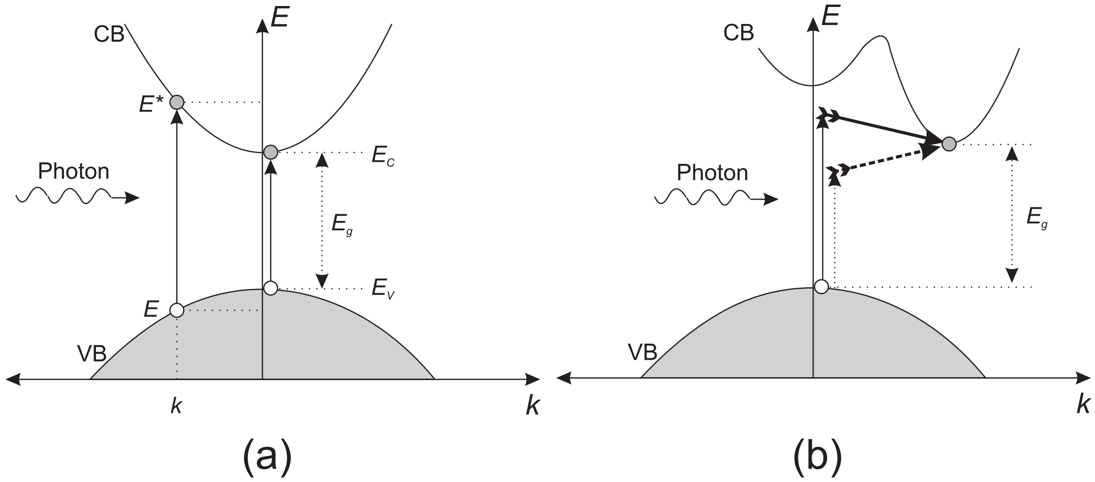

Figure 2.6: Schematic diagram for (a) a direct transition of excited electrons by photon absorption from the valence band (VB) to the conduction band (CB) and (b) an indirect transition of an excited electron by a photon absorption accompanied by phonon emission (solid arrow with tail) or absorption (dashed arrow with tail) from the VB to CB.

In a direct transition process, an electron is photoexcited without accompanied by phonons. During such a transition, the electron's $\overrightarrow{k}$-vector does not change since the momentum of incident photon is negligibly small as compared to the electron momentum. As it is shown in Fig. 2.6(a), a direct transition is represented in a E vs. k diagram as a vertical transition of the electron from the valence band with an energy E and wavevector $\overrightarrow{k}$ to the conduction band with a final energy E^* and wavevector $\overrightarrow{k}^*$ where $|\overrightarrow{k}| = |\overrightarrow{k}^*|$. The energy difference $(E^* - E_C)$ corresponds to the kinetic energy of the excited electron which is expressed as $(\hbar k)^2/(2m_e^*)$ where m_e^* is the electron effective mass. Similarly, $(E_V - E)$ is the kinetic energy of the hole created in the valance band after direct transition which is equal to $(\hbar k)^2/(2m_h^*)$ where m_h^* is the effective mass of the hole.

2.4.2.1 Absorption Coefficient

The optical absorption coefficient for interband electronic transitions can be written as

$$\alpha(\omega) = B \int \frac{N_V(E - \hbar\omega) N_C(E)}{\hbar\omega} dE \tag{2.15}$$

where B is a constant including the square of the transition matrix element as a factor, N_V and N_C are the density of states in the valence and conduction band, respectively and the integration is performed over all pairs of states in the valence $N_V(E)$ and conduction states $N_C(E)$. The absorption coefficient expressed in Eqn. 2.15 is actually derived from the rate of absorption described quantum mechanically by the Fermi's golden rule in which the probability per unit time of finding an electron in an eigenstate Ψ_f given that it is initially in Ψ_i is written by the formula

$$W_{i \to f} = \frac{2\pi}{\hbar} \left| \int d\overrightarrow{r} \Psi_f^* H^{'} \Psi_i \right|^2 \delta(\hbar\omega - E_f + E_i) \tag{2.16}$$

where $H^{'}$ is the harmonic perturbation Hamiltonian of the form $2V(r) cos\omega t$. Therefore, the absorption coefficient in Eqn. 2.15 can be generally expressed by the equation

$$\alpha = \frac{1}{ncV\omega} \left(\frac{2\pi e}{m_e^*} \right)^2 \int_{E_C}^{E_V + \hbar\omega} |p_{CV}|^2 N_C(E) N_V(E - \hbar\omega) dE \tag{2.17}$$

where n is the real part of the refractive index, V is the volume of the semiconductor material and p_{CV} is the transition matrix element of the electron-phonon interaction between the extended bands. However, it is difficult to solve the integral in Eqn. 2.17 analytically. For this reason, p_{CV} is evaluated by using dipole approximation for crystalline materials whereas it is chosen as a constant for amorphous materials. After evaluation of the integral as a result of mentioned approximations, near the band edges where the density of states in the extended bands can be approximated as a parabolic band, the absorption coefficient for direct transition is calculated as a function of photon energy as

$$\alpha\hbar\omega = A^{'} (\hbar\omega - E_g)^{1/2} \tag{2.18}$$

where the constant $A^{'} \approx (e^2/nch^2 m_e^*)[2m_e^* m_h^*/(m_e^* + m_h^*)]^{3/2}$ and E_g is the direct energy band gap [47]. Furthermore, a two-step process is required in an indirect optical transition in which the momentum conservation is maintained by a phonon interaction with the excited electron. In order to realize an indirect optical transition a phonon with energy E_p is either emitted or absorbed as shown in Fig. 2.6(b). By using the parabolic band approximation and Bose-Einstein statistics that defines the number of phonons by the equation

$$N_p = \frac{1}{e^{\frac{E_p}{k_B T}} - 1} \tag{2.19}$$

where k_B is the Boltzmann constant and T is the absolute temperature, the absorption coefficient for a transition with phonon absorption is derived as

$$\alpha_a \hbar\omega = \frac{A^{'}(\hbar\omega - E_g - E_p)^2}{e^{\frac{E_p}{k_B T}} - 1} \tag{2.20}$$

for $\hbar\omega > E_g - E_p$. Since the probability of phonon emission is proportional to $1 + N_p$, the absorption coefficient for a transition with phonon emission is found to be as

$$\alpha_e \hbar\omega = \frac{A^{'}(\hbar\omega - E_g + E_p)^2}{1 - e^{-\frac{E_p}{k_B T}}} \tag{2.21}$$

for $\hbar\omega > E_g + E_p$ [46,47].

Therefore, the overall absorption coefficient is expressed as

$$\alpha = \alpha_a + \alpha_e \tag{2.22}$$

for photon energies $\hbar\omega > E_g + E_p$. Since the phonon density is very small at very low temperatures as the temperature dependence is expressed in Eqn. 2.20, the values of α_a are also small.

In the light of the discussions for absorption phenomena in semiconductors, the photons having less energy values than the band gap energy are not supposed to be absorbed for direct transitions and therefore a steeply rising absorption edge is expected for crystalline semiconductor materials. However, for non-crystalline semiconductors, an exponentially increasing absorption edge is observed for the photons of energy less than the band gap energy, $\hbar\omega > E_g$ due to localized band tail states. In other words, the band edges at the E_V and E_C do not have well-defined cut-off energies. In non-crystalline semiconductors, there are localized energy states below the conduction band and above the valence band whose densities decay sharply with energy values away from the band edges, which is described as band tailing. Furthermore, the photons of energy less than band gap energy can excite the electrons occupying states in the valence band to tail states below conduction band, eventually an absorption edge is expected to vary exponentially as a function of photon energy. This phenomena is expressed by Urbach's rule [48] as

$$\frac{d(Ln\alpha)}{d(\hbar\omega)} = \frac{1}{k_B T} \tag{2.23}$$

where α depends on the photon energy exponentially and absorption edge in this region is called as Urbach's tail. If the parabolic band approximation is used for the valence band and the density of states of the tail states below the conduction band at some energy E is expressed as

$$N = N_o e^{\frac{E}{E_o}} \tag{2.24}$$

where E_o is an empirical parameter describing the distribution of the states and is in units of energy, then by using Eqn. 2.17 the absorption coefficient dependence on the photon energy is found to be as

$$\alpha = \alpha_o e^{\frac{(\hbar\omega - E_O)}{\Delta E}} \tag{2.25}$$

where α_o, E_o and ΔE, which is called as Urbach width, turn out to be material-dependent constants. As the observation of Urbach's tail in non-crystalline semiconductors is attributed to band tail states due to strong internal fields arising from ionized impurities and structural defects, also both structural temperature-induced disorder in crystals act as a mechanism leading to Urbach exponential absorption tail [46, 49, 50].

As a matter of fact, in non-crystalline semiconductor materials, the optical absorption process is described characteristically by three different transitions

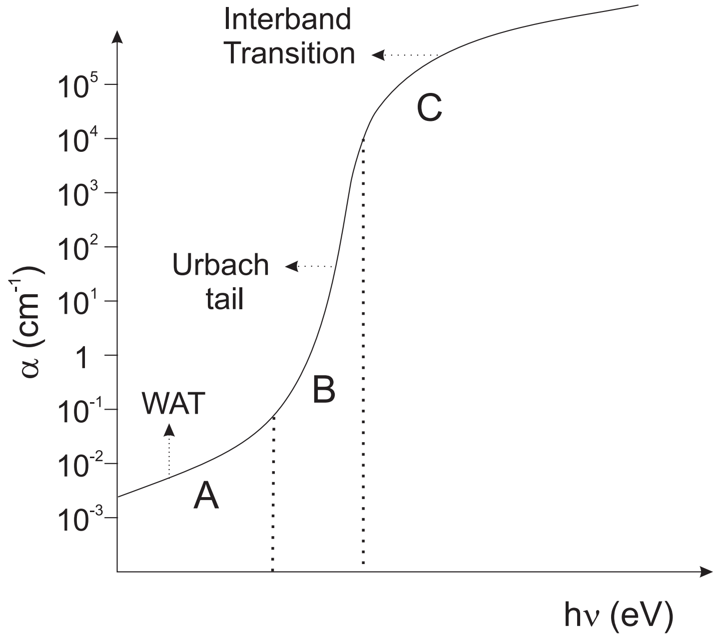

Figure 2.7: A typical variation of absorption coefficient as a function of incident photon energy in non-crystalline semiconductors. In region A and B, the optical absorption process is due to the absorption of photons having energy less than band gap between tail and tail states and between tail and extended states, respectively. In region C, the transitions occur between the VB and CB.

corresponding to

- excitations from tail states to tail states (describes weak absorption tail (WAT) in Region A in Fig. 2.7, where typically $\alpha < 10^{-1} cm^{-1}$),
- excitations from tail states to extended states (describes Urbach's tail in Region B in Fig. 2.7, where typically $10^{-1} < \alpha < 10^{4} cm^{-1}$),
- excitations from extended states to extended states (Region C in Fig. 2.7, where typically $\alpha > 10^{4} cm^{-1}$).

2.5 Electrical Transport Properties of Semiconductors

The band theory of semiconductors, which results in determination of single-electron eigenstates (Bloch waves) and energies forming energy bands separated by forbidden energy band gaps, serves as a theoretical base for the development of electrical transport theory in crystalline semiconductors. In general, the electrical transport in a semiconductor involves the sum of contributions from all carrier types; electrons and holes. According to a simple model, which is virtually valid for many semiconductor materials, the electrical conductivity of a semiconductor containing two contributions is expressed as

$$\sigma = ne\mu_e + pe\mu_h \tag{2.26}$$

where μ_e and μ_h are electron and hole mobilities, respectively. Also, n and p refer to the number of electrons per unit volume in the conduction band and the number of holes per unit volume in the valence band, respectively. Moreover, the mobility of a carrier type is defined as the drift velocity of carrier per unit electric field and by using the relaxation-time approximation the mobilities can be written as

$$\mu_e = \frac{e\tau_e}{m_e^*} \tag{2.27}$$

and

$$\mu_h = \frac{e\tau_h}{m_h^*} \tag{2.28}$$

where $1/\tau_e$ and $1/\tau_h$ are defined as the scattering rates for the electrons in the conduction band and the holes in the valence band, respectively [51]. Furthermore, the temperature dependence of the electrical conductivity is mostly due to the rapidly changing number of free carriers over a wide temperature range. The above-mentioned model predicts the n and p when impurities are present by using the law of mass action, which is given as

$$np = C'T^3 e^{-\frac{E_g}{k_B T}} \tag{2.29}$$

where C' is a constant depending on the structural details of valence and conduction band extrema and the conservation law together, which is defined as

$$n - p = N_D - N_A \tag{2.30}$$

where N_D and N_A are the densities of donors and acceptors, respectively.

In the case of a non-crystalline semiconductor, in which static disorder modifies the electron wavefunctions and energy spectrum of the semiconductor, the generalized equation for electrical conductivity at finite temperatures, which is based on the Boltzmann transport theory, can be expressed as

$$\sigma = \int \sigma(E) \left(-\frac{\partial f(E)}{\partial E} \right) dE \tag{2.31}$$

where $f(E)$ is the electron distribution function, $\sigma(E)$ is the energy-dependent conductivity and the integration is performed over the extended states in the conduction band (in case of n-type semiconductor) [52].

2.5.1 Electrical Transport Properties in Polycrystalline Semiconductors

The distinguishing structural characteristic of the polycrystalline thin film semiconductors is the formation of *grain boundaries* which separate small single crystal regions (called as grains or crystallites) within the film structure. As a matter of fact, polycrystalline thin film semiconductor structure is an aggregate of small single crystals with sizes having typical values between 10 nm and 10 μm which are in a close contact with each other, however, the contact regions (boundaries) are misaligned crystallographically. Furthermore, the size of grains within the films dominantly depends on the material and the film growth conditions. Therefore, due to this misaligned grains, the grain boundary regions contain high densities of dislocation defects. In other words, these interface regions (sometimes called inner surfaces) contain high densities of electronic states which can trap electronic charges and cause a bending in energy bands within the grains. In fact, the electrical conduction in polycrystalline semiconductors is governed mainly by the grain boundary potentials built due to this distinguished structural formation [53, 54].

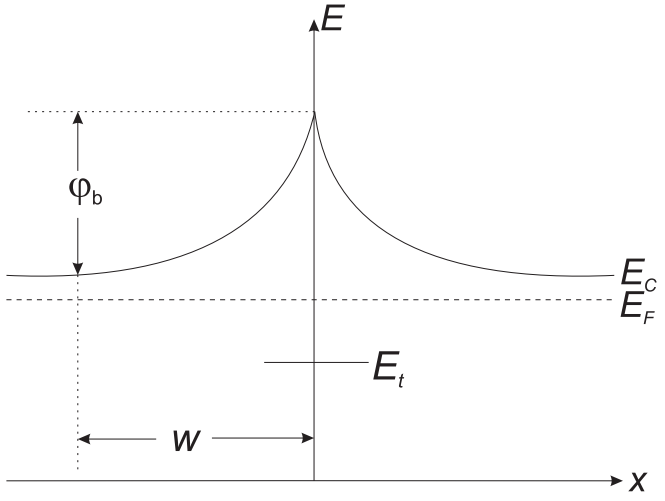

Figure 2.8: The schematic illustration of the bending in the conduction band of a polycrystalline semiconductor in the vicinity of a grain boundary.

For an n-type polycrystalline semiconductor, at normal temperature values, electrons, which are liberated by means of thermal ionization of shallow donor atoms, exist in the conduction band of grain structure. These free electrons can reach the grain boundary regions and be spatially localized after being captured by the defect states. Therefore, these localized negative charges keep the free electrons away from the boundary regions by repelling them due to Coulombic forces and produce a depletion region. That is to say, in the conduction band energy diagram, the formation of this depletion region is depicted as a band-bending as illustrated in Fig. 2.8. Assuming a uniform distribution of donor atoms with a volume density N_D (m^{-3}) within grain structure, the conduction band energy as a function of position in the depletion region can be expressed by the relation

$$E_C = E_C^o + \left(\frac{e^2 N_D}{2\varepsilon\varepsilon_o}\right) x^2 \tag{2.32}$$

where ε is the relative dielectric constant of the polycrystalline semiconductor film. By making use of this equation, the total band-bending φ_b can be written as

$$\varphi_b = \frac{e^2 N_D w^2}{2\varepsilon\varepsilon_o} \tag{2.33}$$

where w is the width of the depletion region. If the trap energy E_t lies well below the Fermi level as shown in Fig. 2.8 and the traps are assumed to be all filled with electrons, then the surface density (N_t (m^{-2})) of the interface traps can be expressed as

$$N_t = 2N_D w \tag{2.34}$$

and by eliminating w in Eqn. 2.33 a new expression for the band-bending in terms of N_D and N_t as

$$\varphi_b = \frac{e^2 N_t^2}{8\varepsilon\varepsilon_o N_D} \tag{2.35}$$

and this band-bending is a crucial potential barrier for free electrons to surmount in order to contribute to the electrical conduction in the polycrystalline semiconductor thin film.

In order to explain the electrical conduction in polycrystalline semiconductors, several theoretical models were proposed by taking the band-bending and potential barrier formation due to the defects in the grain boundary regions into consideration. The most complete and convincing theoretical approaches are presented in the following subsections in order to explore the different current conduction mechanisms which are each dominant at different temperature regions.

2.5.1.1 Thermionic Emission of Carriers

At relatively high temperatures, the free carriers in the conduction band of the grain structures can gain enough thermal energy to surmount the potential barrier formed at the grain boundary region in order to maintain the electrical conduction. Therefore, the term *thermionic emission of carriers* refers to this thermal excitation process of the carriers over the top of the grain boundary potential barrier. As mentioned above, this type of current conduction mechanism dominates in terms of the contribution to electrical conductivity of polycrystalline semiconductors at high temperature region. Because, at sufficiently high temperature values, the electrical current flowing through the polycrystalline semiconductor is controlled mainly by the rate at which free charge carriers in the conduction band of a grain are thermally excited over the grain boundary potential barrier into the conduction band of the neighbor grain when especially the potential barrier width is too wide for tunneling probability to be almost zero. As a general assumption, the contribution of the free carriers tunneling through the potential barriers to the electrical conduction can be neglected in theoretical calculations for undoped and slightly doped polycrystalline semiconductors since both the potential barrier height and width decrease significantly in highly doped polycrystalline semiconductors.

Several theoretical models have been proposed by Volger [55], Petritz [56], and Berger [57] in order to explain the current transport properties of polycrystalline semiconductors at thermionic emission regime. However, so far the most comprehensive theoretical model, which is relatively the most complete and consistent with the experimental results, has been analytically developed by Seto [58] under the name of *The Grain Boundary Trapping Model.* The model was based upon the physical structure, charge distribution scheme and energy band structure of the polycrystalline semiconductors with basic assumptions that i) grains are chosen to be identical, ii) only one type of impurity atoms, which are uniformly distributed with a volume concentration N (m^{-3}) concentration, exists, iii) the grain boundary thickness is assumed to be negligibly small and traps with surface concentration N_t (m^{-2}) are located at energy E_t, and iv) the traps are initially neutral and become charged by trapping free charge carriers.

Seto's calculations for the one-dimensional p-type polycrystalline semiconductors start with to solve Poisson equation for the grain boundary region and solution for the region reaches

$$V(x) = V_v^o + \left(\frac{q^2 N}{2\varepsilon\varepsilon_o}\right) x^2 \tag{2.36}$$

where V_v^o is the potential of the valence band edge as found in Eqn. 2.32 apart from the type of semiconductor. The critical doping level at which the two depletion regions from either side of the grain meet at the center of the grain with size L can be calculated by using Eqn. 2.34 as

$$N_c = \frac{N_t}{L} \tag{2.37}$$

and therefore, by using the corresponding band-bending value calculated from Eqn. 2.35, the potential barrier energy can be expressed as

$$E_b = q\varphi_b = \frac{q^2 L^2 N}{8\varepsilon\varepsilon_o} \tag{2.38}$$

and eventually the average carrier concentration calculated for the grain region is found to be

$$p_{av} = \left(\frac{N_v}{qL}\right)\left(\frac{2\pi\varepsilon\varepsilon_o kT}{N}\right)^{1/2} exp\left(\frac{E_b + E_F}{kT}\right) erf\left[\frac{qL}{2}\left(\frac{N}{2\varepsilon\varepsilon_o kT}\right)^{1/2}\right] \tag{2.39}$$

and thermionic emission current density can be written as

$$J = qp_{av}\left(\frac{kT}{2\pi m^*}\right)^{1/2} exp\left(-\frac{q\varphi_b}{kT}\right)\left[exp\left(\frac{qV_G}{kT}\right) - 1\right] \tag{2.40}$$

where V_G is the voltage drop across the bulk of the grain. For sufficiently small values of V_G, ($qV_G \ll kT$), the conductivity is calculated from the Eqn. 2.40 as

$$\sigma = q^2 L p_{av}\left(2\pi m^* kT\right)^{-1/2} exp\left(-\frac{q\varphi_b}{kT}\right) \tag{2.41}$$

and by considering two doping density regimes, the conductivities are calculated by substituting the Eqn. 2.39 into the Eqn. 2.41 as

$$\sigma \sim exp\left[-\frac{(E_g/2 - E_F)}{kT}\right],\ NL < N_t \tag{2.42}$$

and

$$\sigma \sim T^{-1/2} exp\left(-\frac{E_b}{kT}\right),\ NL > N_t \tag{2.43}$$

by taking the effective mobility of the carriers as

$$\mu = \mu_o exp\left(-\frac{q\varphi_b}{kT}\right) = qL\left(2\pi m^* kT\right)^{-1/2} exp\left(-\frac{q\varphi_b}{kT}\right) \tag{2.44}$$

where μ approaches the value of μ_o when the doping level increases in which case φ_b goes to zero [58, 59].

2.5.1.2 Tunneling

At relatively low temperatures, free carriers in the conduction band of the grains can not be excited thermally over the grain boundary potential barrier. In this case, the explanation for the tendency of electrical conduction to reach a saturation at low temperatures comes from the concept of quantum mechanical tunneling of the carriers through high but narrow potential barriers. The tunneling currents in polycrystalline semiconductors have been worked out rigorously and several theoretical approaches have been developed so far for example by Seager [60] and Garcia [61]. The tunneling current density is calculated by Simmons [62] by means of WKB (Wentzel-Kramers-Brillouin) approximation, which is utilized when the potential energy is a slowly varying function of position, as

$$J_t = J_o\left(\frac{FT}{sin(FT)}\right) \tag{2.45}$$

where J_o is the tunneling current density at 0 K, T is the transmission coefficient for tunneling through a barrier given by

$$T \cong exp\left[-\frac{2}{\hbar}\int_0^d \sqrt{2m(V_o - E)}dx\right] \tag{2.46}$$

where $(V_o - E)$ is the effective barrier height and d is the barrier width [63]. Moreover, F in Eqn. 2.45 is given by

$$F = \frac{2\pi^2 k(2m^*)^{1/2} d}{h < \Phi >^{1/2}} \tag{2.47}$$

where $< \Phi >$ is the mean barrier height of the grain boundary potential. Therefore, the corresponding conductivity can be written by using the relation $\sigma_t = J_t L/V$ as

$$\sigma_t = \sigma_o \frac{FT}{sin(FT)} \tag{2.48}$$

and for sufficiently small values of FT, the conductivity σ_t relation turns out to be as

$$\sigma_t = \sigma_o \left[1 + \left(\frac{F^2}{6} \right) T^2 \right] \tag{2.49}$$

where σ_o is the conductivity at 0 K.

2.5.1.3 Hopping Charge Transport

At lower temperatures, the concentration of charge carriers occupying extended states above the bottom of conduction band is too low to control the electrical conductivity of the semiconductor. However, the hopping carrier transitions between localized states might make an essential and decisive contribution to the charge transport. In fact, the hopping transport mechanism determines the electrical conduction in polycrystalline semiconductors in the range of temperatures well below room temperature. In this charge transport regime, a sequence of tunneling transitions of charge carriers happens as if a series of them hops between randomly distributed localized defect sites. Each site is characterized by a spatially localized electronic state with an energy level E. The energy distribution of the randomly distributed localized states for electrons (for n-type semiconductor case) with concentration N_o is determined by the density of states (DOS) function given as

$$g(E) = \frac{N_o}{E_o} G \left(\frac{E}{E_o} \right) \tag{2.50}$$

where E_o is the energy scale of the DOS distribution. For an electron, tunneling transition probability to jump from a localized state i to a localized state j, which is lower in energy, can be constructed as

$$P_{ij} = \nu_o exp \left(- \frac{2R_{ij}}{\gamma} \right) \tag{2.51}$$

where R_{ij} is the spatial separation between the states i and j, γ is the localization length characterizing the exponential decay of the electron wave function of the localized state and ν_o is the pre-exponential factor depending on the electronic interaction mechanism (usually assumed to be the interactions of electrons with phonons) causing the hopping transition. Such a transition is illustrated schematically in Fig. 2.9. In most calculations, the factor ν_o is assumed for the disordered structure to be of the order of the phonon frequency $\sim 10^{13}$ s^{-1} [64].

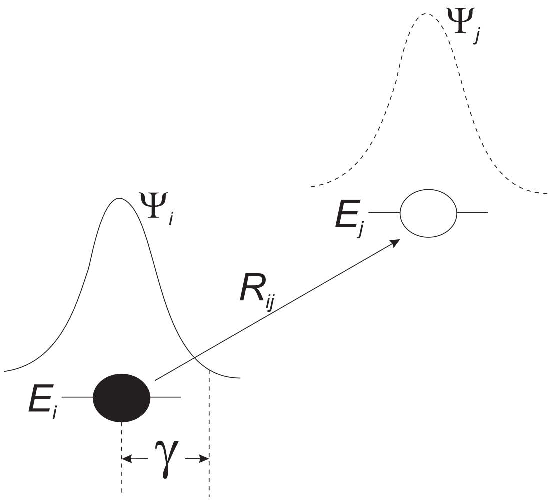

Figure 2.9: The schematic representation of hopping transition between two localized states i and j with respective energies E_i and E_j. The Ψ_i and Ψ_j, which are shown as solid and dashed line respectively, correspond to localized wavefunctions of carriers and γ is the localization radius.

When a transition of an electron occurs from a localized state i to a higher energy localized state j, the transition probability depends on the energy difference between the states, therefore this energy difference must be met such as by absorbing of a phonon with the required energy. In this case, the transition probability in Eqn. 2.51 is modified as [65]

$$P_{ij}(R_{ij}, E_i, E_j) = \nu_o exp\left(-\frac{2R_{ij}}{\gamma}\right) exp\left(-\frac{E_j - E_i + |E_j - E_i|}{2kT}\right) \qquad (2.52)$$

which is valid for the case of the transition from an occupied state to an empty one. In thermal equilibrium, the Fermi statistics determines the occupation probabilities of the localized states with different energies and further modifies the Eqn. 2.52

$$P_{ij} = \nu_o exp\left(-\frac{2R_{ij}}{\gamma}\right) exp\left(-\frac{|E_i - E_F| + |E_j - E_F| + |E_j - E_i|}{2kT}\right) \tag{2.53}$$

by adding the relative energy positions of sites i and j with respect to the Fermi energy E_F. The theoretical description of the hopping conduction can now be formulated by means of Eqn. 2.53 together with the Eqn. 2.50. If it is assumed that the electronic states are strongly localized and the inequality $N_o\gamma^3 \ll 1$ is satisfied, the electrons prefer to hop between the sites that are spatially nearest and when this type of hopping occurs the charge transport regime is called as *the nearest-neighbor hopping* (NNH). This type of conduction mechanism is favorable especially when thermal energy kT is larger than the energy scale E_o of the DOS. In such a case, the energy dependent terms in Eqn. 2.52 and 2.53 do not contribute critically and the average transition rate can be constructed by weighting Eqn. 2.51 with the probability to find the nearest neighbor at some spatial position R_{ij} and integrating it over all possible distances as

$$< P >= \nu_o \int_0^\infty exp\left(-\frac{2R}{\gamma}\right) N_o exp\left(-\frac{4\pi}{3}R^3 N_o\right) 4\pi R^2 dR \simeq \pi\nu_o N_o \gamma^3 \tag{2.54}$$

and if it is assumed that Eqn. 2.54 can be used to describe the mobility and conductivity of charge carriers, the result will lead an erroneous conclusion that the mobility and conductivity are linearly dependant on the concentration of localized states N_o [66]. In order to correct the calculations, the critical distance $R = R_c$ is found that a continuous hopping path is possibly found through the infinite system via localized sites with relative separations $R \leq R_c$ and R_c is given in three-dimensional space by the relation [64, 66]

$$\frac{4\pi}{3} N_o R_c^3 = B_c \tag{2.55}$$

where $B_c = 2.7$ is the average number of neighboring localized sites that can be found within the distance smaller than R_c. By inserting R_c into Eqn. 2.51, the conductivity can be described in the form

$$\sigma = \sigma_o exp\left(-\frac{\xi}{\gamma N_o^{1/3}}\right) \tag{2.56}$$

where σ_o is the pre-exponential factor and $\xi = 1.73$. Therefore, correct concentration dependence of the conductivity in NNH regime is defined as in Eqn. 2.56. As a result, if only spatial factors make the transitions favorable and the temperature of the semiconductor is rather at high values then NNH transport mechanism can well explains the charge transport phenomena through localized states within the band gap energy. Mott [67] put forward the concept of *the variable-range hopping* (VRH) that can explain the charge transport via a system of randomly distributed localized states at low temperature region. Mott argues that at low temperatures, the most efficient charge transport can happen between the localized states with energy levels near the Fermi level because of the strong possibility that the occupied and empty states with close energies can be found within the energy range located near the Fermi level. The distinction between NNH and VRH transport mechanisms of the carriers are illustrated schematically in Fig. 2.10.

The energy width W of the efficient narrow energy range, which is symmetric with respect to the Fermi level, can be written as

$$g(E_F)WR^3(W) \simeq 1 \tag{2.57}$$

which is similar to the criterion used in Eqn. 2.55 for NNH. Therefore, typical hopping distance can be calculated as a function of the energy width as

$$R(W) \simeq [g(E_F)W]^{-1/3} \tag{2.58}$$

and by substituting this into Eqn. 2.52, the typical transition rate can be obtained as

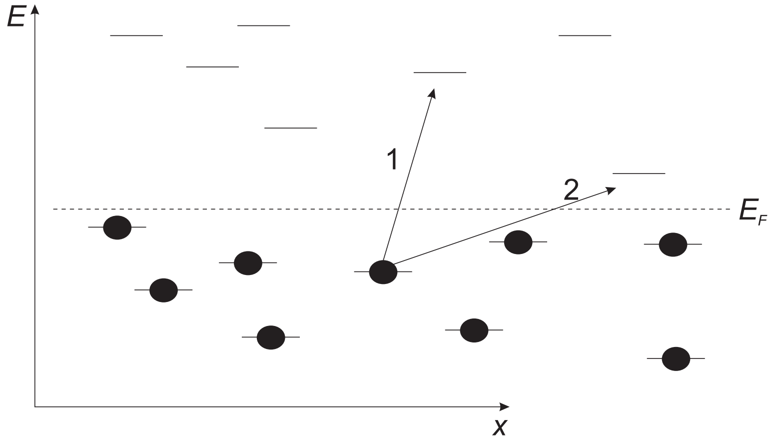

Figure 2.10: The schematic illustration for two alternative hopping transitions between occupied (circles with solid lines) and empty (solid lines) states. The transitions 1 and 2 correspond to the nearest-neighbor hopping and the variable-range hopping transport of the carriers, respectively.

$$P_{VRH} = \nu_o exp\left(-\frac{2}{[g(E_F)W\gamma^3]^{1/3}} - \frac{W}{kT}\right) \tag{2.59}$$

and the energy width W providing the maximum transition (hopping) rate can be maximized by equating the derivative of Eqn. 2.59 with respect to W to zero and the optimal energy width W is given by

$$W = \left[\frac{2kT}{3g^{1/3}(E_F)}\right]^{3/4} \tag{2.60}$$

and finally, the Mott's famous formula for the temperature dependent conductivity for VRH conduction regime at low temperatures is given by [67]

$$\sigma = \sigma_o exp\left[-\left(\frac{T_o}{T}\right)^{1/4}\right] \tag{2.61}$$

where T_o is the characteristic temperature defined as

$$T_o = \frac{\beta}{kg(E_F)\gamma^3} \tag{2.62}$$

where the numerical value of β is calculated to be in between 10.0 and 37.8 after various theoretical studies in three-dimensional physical systems [64, 68].

2.5.2 Electrical Transport Properties in Amorphous Semiconductors

Amorphous semiconductors are characterized by a complete lack of long-range order in arrangements of constituent atoms. Therefore, the electrical properties of amorphous semiconductors differ in description as compared to crystalline and polycrystalline ones.

The energy band gap, which is the most important parameter for a semiconductor, is also a characteristic property for an amorphous semiconductor and it is strongly dependent on the methods and conditions used to deposit it. However, the electronic states are described in terms of a broad density of states (DOS) function which is continuous throughout the band gap [67] as shown in Fig. 2.11. The band edges are much less sharp than in the crystalline semiconductor case, and states extends into the gap from both the conduction and valence band to form a tailing of states, which is called as *band tail states.* In fact, due to this tailing of states, the Fermi level is pinned in the vicinity of the middle of the gap, which means that the free carrier concentrations in either of the bands are very low. Also, the carrier mobility values are very low because of the absence of periodicity and only the electrons having greater energy than a certain value of E_C in the conduction band are mobile. On the other hand, the electrons with energies less than E_C are localized. Therefore, together with the corresponding energy value in the valence band E_V, *the mobility gap* is defined as the difference between the two energy values. The mobility gap functions as the band gap in crystalline semiconductors, however in principle, the optical and mobility gaps are expected to be different [67, 69].

Also, theoretical works on the description of the electrical conductivity in amorphous semiconductor are more complicated than in crystalline case, Mott and Davis [67] proposed theoretical models for conductivity at different temperature regions. After several detailed calculations, it was suggested that the conductivity in the conduction band states above mobility gap (for energies greater than E_C) depends on energy. The conductivity of an amorphous semiconductor

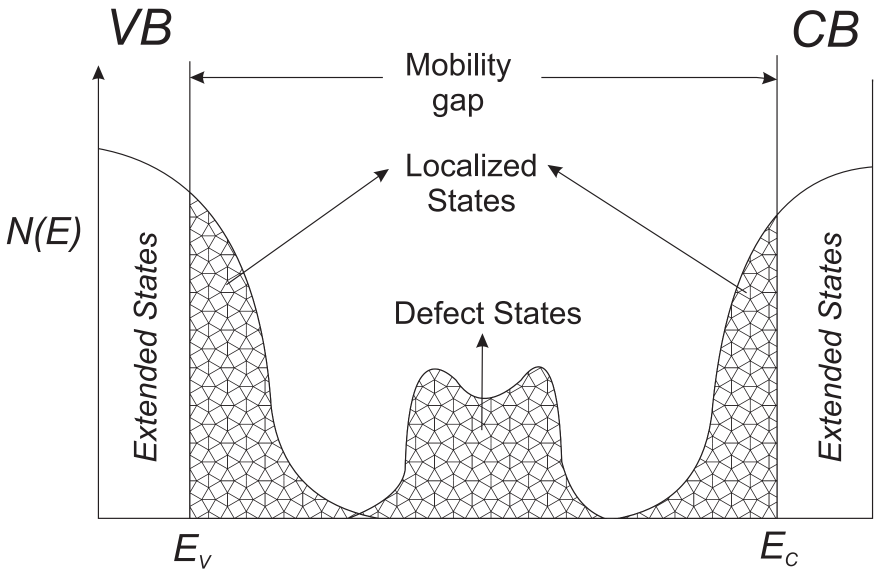

Figure 2.11: The schematic drawing of density of states (DOS) distribution function for a typical amorphous semiconductor.

decreases to a limiting value, which is named as the minimum metallic conductivity depending on the spacing between the constituent atoms, as the energy values approach E_C. The minimum metallic conductivity is defined as

$$\sigma_{min} \sim 10^4 a \tag{2.63}$$

where a is the spacing between atoms and the electron mobility above the band edge can be suggested as

$$\mu_{band} = \frac{\sigma_{min}}{qN} \tag{2.64}$$

where N is the effective density of states in the conduction band. At relatively high temperature values, the electrical conductivity is dominated by the electrons in the extended states above E_C with the thermal activation energy which is equal to $(E_C - E_F)$ and the Fermi level is pinned well below E_C. Therefore, the conductivity can be written in the form

$$\sigma_{extended} = \sigma_o exp\left[-\frac{(E_C - E_F)}{kT}\right] \tag{2.65}$$

where σ_o is the pre-exponential factor. On the other hand, at low temperature at which electrons can not have the thermal activation energy, the electrical conduction may be maintained by the electrons occupying the band tail states with energies less than E_C by phonon-assisted hopping between neighbor sites. Then, the hopping conductivity at low temperature is given as

$$\sigma_t = \sigma_T exp\left[-\frac{(E_T - E_F)}{kT}\right] \tag{2.66}$$

where E_T is the average energy of these band tail states and σ_T is the pre-exponential factor, which is smaller than σ_o in Eqn. 2.65. Furthermore, at very low temperatures, Mott's variable range hopping (VRH) conduction, which is discussed in detail in section 2.5.1.3, is valid and in this case the conductivity is given as

$$\sigma_{VRH} = \sigma_v exp\left[-\left(\frac{T_o}{T}\right)^{1/4}\right] \tag{2.67}$$

where σ_v is the corresponding pre-exponential factor.

2.6 Photoconductivity in Semiconductors

The photoconductivity is defined as the difference between the measured conductivity under illumination, σ_ϕ, provided that the photon energy of light exceeds the band gap energy, and the dark conductivity, σ_{Dark}, which can be written as

$$\sigma_{ph} = \sigma_\phi - \sigma_{Dark}. \tag{2.68}$$

The increase in the conductivity of semiconductors is caused by the generation of free carriers after absorption of photons with energies greater than the band gap energy. However, this increase in conductivity will not continue indefinitely as the light exposure continues. The process of *recombination* limits the rate of generation of free carriers. When a free electron traveling through the crystal lattice, if it passes near a valence band hole, a mutual elimination of both electron and hole occurs due to Coulomb attraction between them by satisfying chemical bonding energy requirement. The recombination process, which is the opposite of the generation of free carriers, produces a balance between generation and recombination resulting in a *steady state photoconductivity* condition. Assuming that the equilibrium electron density of the semiconductor is always much larger than the density of the generated carriers upon light exposure, the probability for an electron and hole to recombine is proportional to the product of their densities which can be written as

$$-\frac{dn}{dt} = Anp = An_o p \tag{2.69}$$

where n_o is the equilibrium density of electrons and A is a constant. Therefore, the equation for an excess carrier density as a function of time can be found by solving Eqn. 2.69 as

$$n(t) = n(0)exp\left(-\frac{t}{\tau}\right) \tag{2.70}$$

where τ is the recombination lifetime and given as

$$\tau = (An_o)^{-1} \tag{2.71}$$

which is defined as the time taken for an excess carrier to recombine. In the steady state condition, the rates of generation and recombination are equal, then the steady state photoconductivity can be obtained as

$$\sigma_{ph} = q\phi_p \alpha \mu \tau \tag{2.72}$$

where α is the absorption coefficient of the semiconductor and ϕ_p is the incident photon flux. Therefore, the photoconductivity is directly proportional to the light flux and the product $\mu\tau$, which is a material dependent parameter. Moreover, the generation rate of free carriers is defined as , $G \approx \phi_p \alpha$.

2.6.1 Two-center Recombination Model

The characteristic physical phenomena observed, when the two recombination centers are present within the band gap of semiconductors with noticeably different capture coefficients, can be listed as the following [70, 71]

- *i*) Supralinear photoconductivity
- *ii*) Photoconductivity saturation
- *iii*) Thermal quenching of photoconductivity
- *iv*) Negative photoconductivity.

The two-center model can describe the unusual photoconductive behavior of the semiconductors when the condition that the exponent $\gamma > 1.0$ is observed in the relation $\Delta n \propto G^{\gamma}$, which is actually the formal definition of supralinear photoconductivity. In supralinear photoconductivity regime, the semiconductor becomes more photosensitive with increasing light flux which implies the increase in lifetime of excess carriers with increasing flux [70].

The photoconductivity encounters an abrupt decrease above a critical temperature, the value of which depends linearly on the incident photon flux. This effect is called as *thermal quenching* and many experimental works proved that the observation of supralinear photoconductivity and thermal quenching of photoconductivity is the characteristic of the photoconductive properties of the semiconductors with two recombination centers.

In highly photosensitive semiconductors, further increase in light flux above a certain critical limit can result in the saturation of the photoconductivity satisfying the condition $\tau \propto G^{-1}$. Furthermore, negative photoconductivity, which is the decrease in conductivity upon illumination of light, is observed in some specific semiconductor materials. In this phenomena, photoexcited carriers are captured and localized at imperfection sites in the steady state condition [70].

2.6.2 The Photoconductivity in Chalcogenide Semiconductors

Simmons and Taylor [72, 73] introduced a theory which shows that the temperature dependence of photoconductivity, which is illustrated in Fig. 2.12, has three distinct temperature ranges which are;

- *i*) high-temperature range (R_{HT}) in which σ_{ph} increases and finally reaches a maximum value at T_c with decreasing temperature and photoexcitation is low ($\sigma_{ph} < \sigma_{Dark}$),
- *ii*) moderate-temperature range (R_{MT}) including the temperatures $T < T_c$. In this range, σ_{ph} decreases as temperature decreases with an activation energy less than that of the σ_{Dark} ($\sigma_{ph} > \sigma_{Dark}$),
- *iii*) low-temperature range (R_{LT}) in which σ_{ph} is independent of temperature ($\sigma_{ph} > \sigma_{Dark}$).

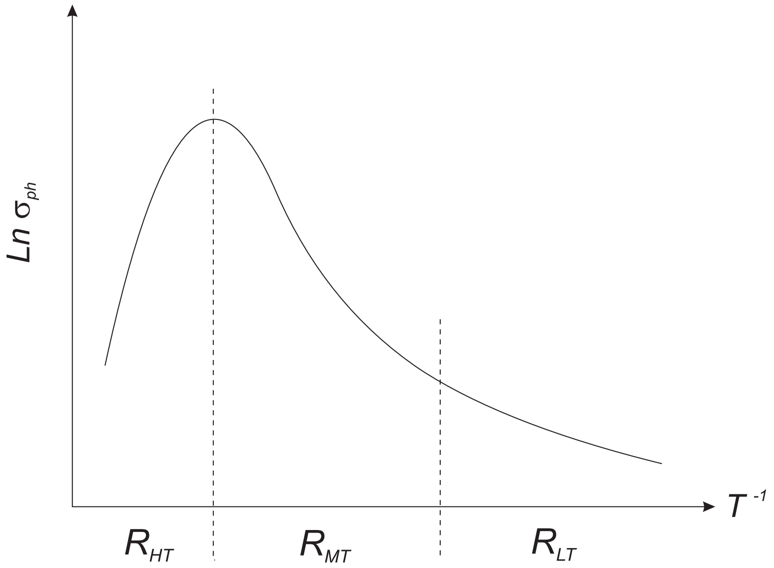

Figure 2.12: The schematic drawing of the characteristic temperature dependence of the photoconductivity of a chalcogenide semiconductor, which has three characteristic temperature portions.

The theory proposed by Simmons and Taylor predicts well the variation of σ_{ph} as a function of temperature for n-type chalcogenide semiconductors in the moderate-temperature range, R_{MT}, where σ_{ph} is thermally activated, as follows;

$$\sigma_{ph} = e\mu_n \left[\frac{GN_o}{v\sigma_t N_t}\right]^{1/2} exp\left[-\frac{(E_c - E_{t1})}{2kT}\right] \tag{2.73}$$

where v is the thermal velocity of electrons, σ_t is the capture cross section corresponding to trap energy level E_{t1}, k is the Boltzmann constant. N_o is a density of state value equal to both N_c and N_v which are the effective density of states in the conduction and valence band, respectively. N_t is the density of trap states. The expression $(E_c - E_{t1})/2$ can be written as the photoconductivity activation energy at R_{MT}, E_{MT}. Furthermore, the photoconductivity activation energy at R_{HT} where thermal quenching is observed is indicated as E_{HT}. Moreover, this model suggests the information about the energy levels of two discrete sets of localized states in the forbidden gap by following relations [73, 74]

$$E_{t1} = 2E_{MT} \tag{2.74}$$

$$E_{t2} = E_a + E_{HT} \tag{2.75}$$

where E_a is the dark conductivity activation energy and the trap positions defines the energy difference from the bottom of conduction band.

CHAPTER 3

EXPERIMENTAL TECHNIQUES

3.1 Introduction

In this chapter, the physical background and aspects of the deposition procedure, post-deposition heat treatment application and the implemented characterization techniques for Ag-In-Se (AIS) thin films are presented as a short introduction to the concepts. It is intended to give brief information about the physical nature of the methods and techniques which were utilized during the production, physical improvement and characterization of the films. Therefore, special physical and technical issues requiring deeper investigation about the related subjects are excluded and can be readily reached through given references in the section.

The section starts with the explanations of deposition process of the films including the details of subsections which are substrate preparation, thin film geometries to be deposited and general properties of the electron beam physical vapor deposition system. Then, the details of post-deposition heat treatment system follows. Finally, the presentation of physical descriptions for the characterization techniques revealing the structural, optical, electrical and photoelectrical properties of the deposited AIS thin films will complete the section.

3.2 The Deposition Process of Ag-In-Se Thin Films

3.2.1 Substrate Preparation

The substrate material, which can be rigid or flexible, serves as the base upon which thin film layers of intended chemical compounds are deposited and should ensure certain physical requirements. In order to obtain high quality thin films, the substrate material should satisfy the physical properties of

- providing deposited thin films with the sufficient mechanical support,
- having a satisfactory surface smoothness and a homogeneous structure,
- adequate thermal endurance in order to guarantee to survive without interfering thin film properties after implementation of necessary thermal processes,
- chemical stability and inert character to the compounds of thin films,
- appropriate electrical insulation (practically should have high electrical resistance $> 10^{14}\,\Omega\,\mathrm{cm}$) to prevent current leakages and to witstand high voltage applications without breakdown [75].

In the light of the above-mentioned requirements, the AIS thin films were deposited onto soda lime glass substrates which are abundantly available in the market and commercially cheap. The glass substrates obtained in the form of microscope slides, were prepared as squares of dimensions 25 mm x 25 mm that have compatible dimensions with those of nests of the substrate holder by means of a diamond cutter tool.

3.2.1.1 Substrate Cleaning

Cleaning of the soda lime glass substrates is a crucial step before thin film deposition process. The glass pieces should be throughly cleaned by means of a careful cleaning process in which the removal of the contaminants on the substrate surface is realized. Otherwise, the contaminants on the glass surface would possibly interfere with thin film growth mechanism which results in undesirable thin film properties and instabilities [76].

The cleaning process of the soda lime glass substrates includes the steps as follows;

- The glass pieces are first immersed in a dilute solution of chemical detergent prepared from highly pure water to dissolve the unwanted contaminants like protein and oil molecules from the surface.
- The same step of solvent cleaning is repeated in the same solution kept in this time at a temperature of about 100^oC.
- Then, the solution containing the glass substrate pieces is put into ultrasonic cleaner to increase the effectiveness of solvent cleaning.
- The glass pieces are rinsed in hot pure water in order to remove the layer of residue on the surface due to detergent solution.
- The glass pieces are immersed in a boiling diluted H_2O_2 solution to remove organic contaminants from glass surface by dissolving them.
- Then, H_2O_2 solution containing the glass pieces is put into ultrasonic cleaner to increase the effectiveness of the process.

After completing the cleaning process, the clean glass substrates are immersed in pure methanol and kept in it till thin film deposition process starts. The glass substrates are removed from methanol and dried by blowing nitrogen gas upon them before placing them into holder before thin film deposition.

3.2.2 Thin Film Geometry

The geometry of deposited thin films is an important factor influencing the electrical and photoelectrical characterization of the films. An appropriate thin film geometry should be chosen for accurate determination of electrical and photoelectrical parameters of the films. Therefore, the AIS thin films were deposited in the shape of Maltese cross whose mask shape is shown in Fig. 3.1(a) for electrical characterization in order to utilize van der Pauw resistivity measurement technique.

The ohmic metal contacts to the deposited films were formed in the vacuum by thermal evaporation of pure indium (In) through suitable copper mask whose shape is pictured in Fig. 3.1(b).

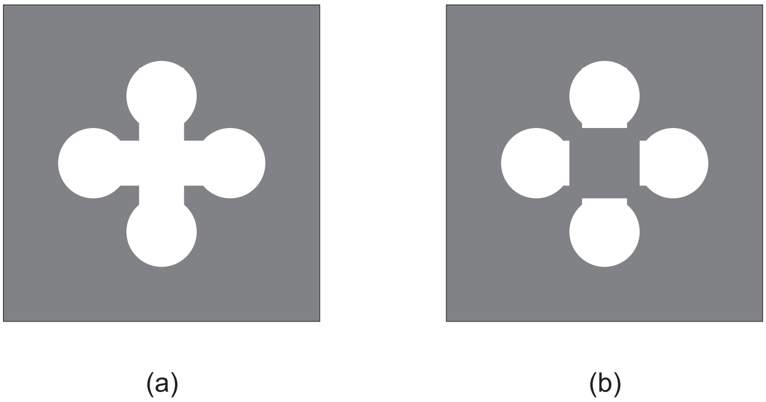

Figure 3.1: Shadow mask shapes for (a) thin film production in van der Pauw (Maltese cross) geometry and (b) metal contact production for thin films grown in van der Pauw geometry

3.2.3 Electron Beam Deposition Technique

The determination of suitable deposition technique is directly assigned by the aimed deposited thin film properties, the application of the film, the temperature optimization of both source and substrate materials, the issues of compositional and thickness uniformity, the deposition rate and the commercial costs. Therefore, the desired composition and microstructure of thin films can be achieved by choosing a suitable deposition technique together with taking the limitations arising from source and substrate materials into account.

Today, most of the practical thin film deposition processes requires a vacuum environment and the physical vapor deposition (PVD) technique is one of the oldest and widely used thin film deposition process in a vacuum chamber. The essence of thin film deposition mechanism for PVD encloses the making a source material evaporate or sublime through heating under vacuum, then the condensation of the evaporated molecules onto a substrate surface to produce a film. According to types of evaporation mechanisms used to evaporate source material in PVD systems, the classification of PVD technique is made as follows;

1. Thermal evaporation, in which source material is heated by wounded heating coil around the quartz source tube,
2. Electron beam evaporation, in which source material is heated by means of an electron gun,
3. Sputtering, in which source material is evaporated by high-energy ionized gas bombardment.

In an electron beam (e-beam) evaporation process, a high-intensity beam of electrons, which are generated by thermionic emission from a current carrying filament, are accelerated through application of high voltage in order to obtain electron energy values up to 15 keV and focused onto source material to be evaporated within a small localized area as shown in Fig. 3.2. The energetic electrons melt the exposed region of material and material evaporates from source and condenses onto substrate surface as a layer.

EB-PVD process provides many desirable properties like relatively high deposition rates (up to 100 μm/minute), low contamination, readily adjustable compositional and uniformity control [77]. The deposition rate can be adjusted by changing the energy and intensity of the electron beam. Moreover, the composition and structure of deposited thin films can be changed by controlling the growth parameters and source material compositions. Since the high-energy electron beam is focused on a small localized area on the source material, possible alloy formation with the crucible material is avoided, thus, potential contamination during evaporation process is only limited by the contaminants existent

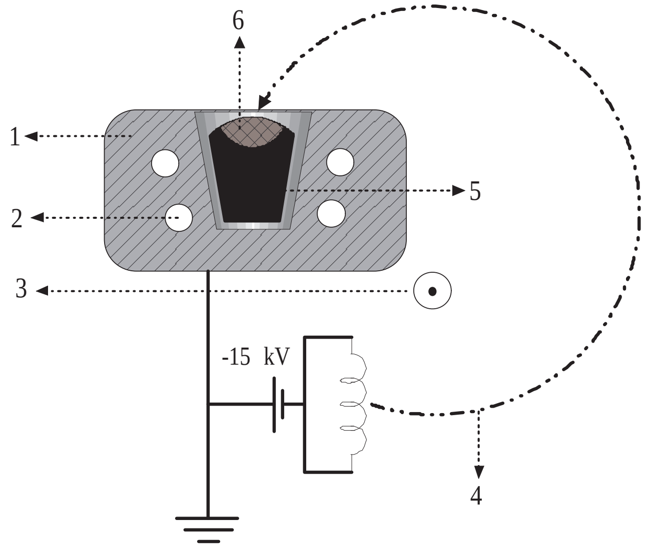

Figure 3.2: Illustration of an electron beam evaporation source. 1. Hearth, 2. water cooling, 3. magnetic field, 4. accelerated and focused electron beam, 5. solid source of evaporation and 6. the evaporating source.

in the original source material [76, 78]. The uniformity of thin films deposited onto the substrate material can be attained by positioning the substrate holder because EB-PVD is a line-of-sight process in which evaporated atoms move from source to substrate on a straight path. Deposited thin films by EB-PVD have usually a uniform structure and a good surface finish.

In this thesis work, the AIS thin films were deposited on ultrasonically cleaned soda lime glass substrates in EB-PVD system, which is equipped with a typical electron beam source composed of a 3-kW electron gun, a water-cooled cavity (often called as hearth) for placing graphite crucible containing source material and an electromagnet for the deflection of the electron beam. Moreover, the EB-PVD system has a stainless steel vacuum chamber that is 50 cm in diameter and 75 cm in height, a fixed substrate holder with a heating unit which is required for improving film adhesion and structure and minimizing strain and stress in thin films, a turbomolecular pump, vacuum gauges, thickness monitoring unit, shutter and a thermocouple fixed at substrate holder. The vacuum chamber is sealed the stainless steel base plate with a rubber o-ring. The lowest attainable pressure within the vacuum chamber corresponding to the highest attainable vacuum level is recorded as around 10^{-7} Torr. The detailed picture of the electron beam evaporation system is shown in Fig. 3.3.

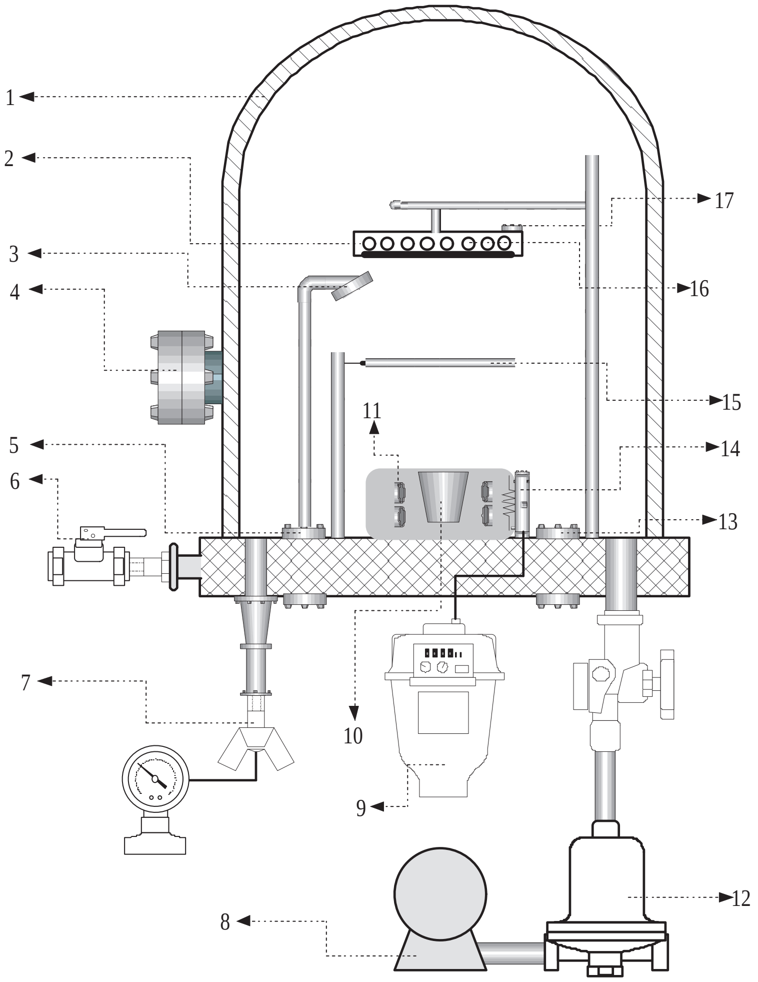

Figure 3.3: Detailed illustration of the electron beam evaporation system utilized for the deposition of AIS thin films. 1. Stainless steel bell jar, 2. sample (substrate) holder, 3. thickness monitor crystal, 4. window, 5. feedtrough, 6. air valve, 7. pirani and penning gauge, 8. rotary pump, 9. e-beam deflection control unit, 10. hearth, 11. water cooling, 12. turbomolecular pump, 13. feedtrough, 14. e-gun, 15. shutter, 16. substrate heater and 17. thermocouple.

The deposition of AIS thin films was performed by e-beam evaporation of $Ag_3In_5Se_9$ single crystal powder, which were grown by Bridgman-Stockbarger technique, in the EB-PVD system as in Fig. 3.3 with a base pressure of about 1.7×10^{-4} Pa. The crystal powder as an evaporation source was placed into a graphite crucible positioned in water-cooled hearth of electron beam source and the soda lime glass substrates were inserted into the substrate holder located at about 15 cm above the source. The substrate holder was heated and the temperature of the glass substrates was kept constant at around 110 °C. During deposition process, the growth rate ($\sim 36\,\mathrm{nm/minute}$) and thickness were controlled by Inficon XTM/2 thickness monitor. Following to the finalization of the deposition process, whole system was allowed to cool down to room temperature without breaking the vacuum condition for the sake of preventing oxidation of thin films and critical parts of EB-PVD system.

3.3 Post-Annealing Process

Post-annealing process is a widely used technique to alter the physical and/or chemical properties of deposited thin films. In such a process, deposited thin films are placed in an isolated furnace in which a desirable gas environment is maintained, and heated gradually up to a desirable temperature as the schematic illustration of such an annealing system is shown in Fig. 3.4. The desired temperature value is maintained for a certain time period and then the system is allowed to cool down to the room temperature slowly.

After annealing the deposited thin films, relaxation in residual film stress and a structural refinement are some of the expected outcomes. During annealing, in general, diffusion of constituent atoms, chemical reactions and cluster formation on film surface could be caused by thermal energy transfer and composition of ambient gas [76].

In this work, after the deposition of AIS thin films, annealing process in an inert gas (nitrogen) ambient was realized at different fixed temperature values changing from 200 to 400°C for a limited time interval of 60 minutes. During the process, a continuous flow of nitrogen (N_2) gas was maintained to the system to free the annealing environment from adventitious contamination caused by atmospheric elements.

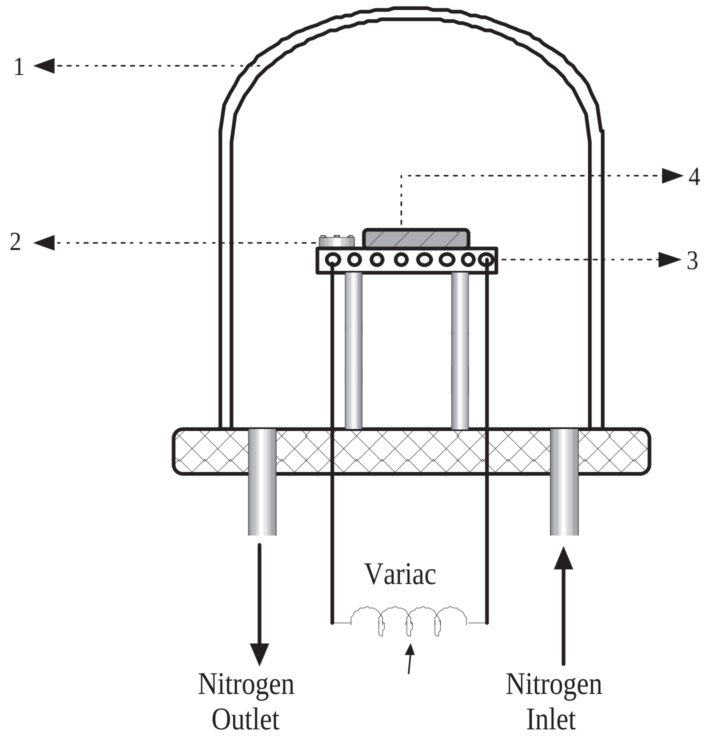

Figure 3.4: The sketch of the setup for post annealing process of AIS thin films. 1. Pyrex glass jar, 2. thermocouple, 3. hot plate and 4. thin film sample.

3.4 Structural Characterization of Thin Films

3.4.1 Thickness Measurements

Thickness of deposited thin films has a critical effect on the characteristics of the films and on the acquisition and interpretation of experimental data gained from many characterization techniques. Therefore, an exact determination of thin film thickness is an important and indispensible task for many optical and electrical mesaurements and data analysis. There exists a variety of thickness measurement techniques that are commonly employed in the field of material characterization. Thickness measurement techniques can be classified as contact and non-contact measuring techniques. In the contact measuring technique, step height of deposited thin films, which is defined between substrate and thin film surface, is measured by the movement of a stylus (generally made of diamond) over substrate and thin film surface as shown in Fig. 3.5. The force applied (1-50 mg) by the stylus on surfaces can be manipulated to obtain optimum thickness measurements which depend critically on hardness of thin film deposition. Non-contact thickness measuring includes optical interferometry, ellipsometry, atomic force microscopy (AFM), scanning tunneling microscopy (STM) and X-ray related measurements in which thin films remain untouched.

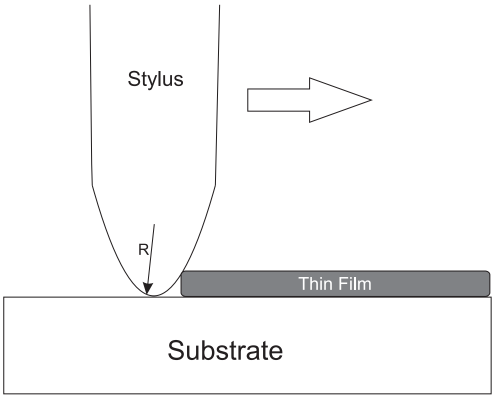

Figure 3.5: Thin film thickness measurement by means of a diamond stylus of DEKTAK 6M profilometer. R is the radius of curvature of the stylus head, which is 12.5 μm in our measurements, and arrow shows the direction of motion of the stylus during measurement.

3.4.2 X-ray Photoelectron Spectroscopy (XPS)

The main application area of X-ray photoelectron spectroscopy (XPS), also known as electron spectroscopy for chemical analysis (ESCA), is the identification of chemical species and chemical bonding states at the surface of deposited thin film, which encloses all elements except hydrogen and helium for most of the spectrometers. The incidence of X-rays upon thin film surface produces photoelectrons emitted from the core levels of constituent atoms at the surface and near-surface region of thin films, which allows an advantageous chemical and compositional analysis of near-surface region of deposited thin films because of almost non-destructive nature of the method. Since XPS utilizes the direct analysis of core level electrons and has a low sample-damage level, it is widely used as one of the most reliable quantitative surface and near-surface region analysis technique [79]. An XPS instrument consists of the X-ray source and spectrometer, which involves an electron analyzer and an electron detector, in a high vacuum environment.

For AIS thin films, the chemical compositions and existing bonding types at the surface and near-surface region were determined by XPS technique performed by a UNISPECS ESCA system with monochromatic X-ray equipped with a Mg Kα radiation source of 1253.6 eV-energy value in METU Central Laboratory. A concentric hemispherical electron analyzer, operating in the constant pass-energy (CAE) mode, was employed to collect the emitted electrons from the surface of the thin films kept under about 1.3 x 10^{-7} Pa high-vacuum level during the process.

3.4.3 X-ray Diffraction (XRD)

X-ray diffraction (XRD) method is one of the most essential tools for the structural characterization of materials. Each crystalline solid material has its unique characteristic X-ray pattern which can be used as a distinguishing property peculiar to the material. As long as the material composition is known, XRD is an effective technique to determine its structure, specifically the crystalline structure, interatomic distance and angle. In general, every scientific or industrial research project dealing with solid materials unavoidably starts with investigating the structural properties by obtaining an X-ray diffraction pattern from X-ray diffractometers. Then, the diffraction pattern is examined to build a comprehensive knowledge about the structure, phase composition and purity of the material. The coping with the diffraction data involves searching for the known diffraction patterns recorded in the International Centre for Diffraction Data (ICDD) database in order to match the measured data.

The X-rays have wavelengths ranging from around 0.1 to 100 Å, which are located between the corresponding wavelength regions of γ-rays and ultraviolet rays in the electromagnetic spectrum. The most commonly used wavelengths in XRD method range between around 0.5 and 2.5 Å because of having the same order of magnitude as the shortest interatomic distances in solid materials. A general-purpose or specific X-ray diffractometer includes an X-ray source, goniometer and a radiation detector.

The XRD measurements for AIS thin films were carried out by using a Rigaku Miniflex XRD system equipped with Cu Kα radiation of average wavelength of 1.54059 Å. All XRD measurements were performed by using the same input parameters, for example, 2θ values were taken between 5 and 90^{o} and scan speed were maintained at 2^{o}/minute. The XRD patterns were analyzed with a computer software and the ICDD database which includes the diffraction patterns of well known structures of chemical compounds which are the combination of Ag, In and Se atoms, together or individually. The peak search-and-match process was carried out based on the observed peak positions at specific angle (2θ) values and relative intensities of the peaks.

3.4.4 Energy Dispersive X-ray Spectroscopy (EDS)

Energy dispersive X-ray spectroscopy (EDS) is a widely used analytical technique implemented for the determination of quantitative microscale elemental composition of the material under investigation. The more common name for the technique is energy dispersive spectroscopy (EDS). EDS analysis equipment is usually attached to a scanning electron microscope (SEM) or is designed as a stand-alone and specialized instrument called as an electron-probe microanalyzer. In practice, the EDS technique has the adequate capacity to detect elemental species to about 0.1 at.% (which corresponds to 1000ppm) range and has a precision of about 0.5-10 percent with equipments of today's technology [80].

In this technique, the material, whose elemental composition is desired to be revealed, is bombarded with a high-energy electron beam and production of X-rays due to collision of electron with atoms of the material is maintained from the subsurface region. Then, the generated X-rays are detected through evaluation of the energy or pulse height. Every element generates X-rays whose wavelengths are peculiar to the element under electron beam bombardment. A powerful capability of this technique is to provide a quantitative elemental composition of materials.

EDS analysis of all deposited AIS thin films were performed by a JSM-6400 scanning electron microscope equipped with EDS facility in Department of Metallurgical Engineering at METU, which was operated at 20 kV, to determine the constituent elements and the quantitative elemental composition of the films.

3.4.5 Atomic Force Microscopy (AFM)

The atomic force microscopy (AFM) is a technique to gain information on the topographic properties of the material surfaces [79,80]. One of the main advantages of AFM is to capability to obtain topographic imaging of not only conducting but also non-conducting materials.

A typical AFM instrument is composed of a cantilever with a sharp tip positioned on the end. Topographic imaging by means of AFM, which serves as a microscopy technique ranging from nanoscale to atomic-scale, is obtained by measuring the interactions of tip and material surface due to forces, types of which can be van der Waals, electrostatic and magnetic, through a sensor. Most commonly encountered force magnitudes are detected in the range 10^{-13} and 10^{-6} N.

The AFM imaging of the topography of AIS thin film surfaces was realized by using a Omicron Nanotechnology AFM system in Department of Physics at Gazi University.

3.5 Optical Characterization of Thin Films

The determination of optical band gaps and optical constants of thin films has crucial importance for solar cell applications. Optical transmission or absorption measurements are used routinely as a simple but effective tool for the determination of optical absorption coefficients, optical band gaps and optical constants, such as refractive index of semiconductor materials both in industry and science.

In an ordinary optical transmission measurement, a collimated beam of light is incident on the semiconductor sample and the intensity of transmitted light is measured as a function of wavelength. In general, in such a measurement is performed by means of a spectrophotometer. A spectrophotometer is basically composed of a light source, a sample holder, a monochromator and a light detector. In a spectrophotometer, the collimated light rays from a source of radiation is passed through a monochromator, which is used to select a narrow band of wavelengths, $\Delta\lambda$, from a light source and then the light of selected wavelengths is directed onto the sample. Afterwards, transmitted light intensities are detected for different wavelengths of light.

In our optical transmission measurements, a Shimadzu UV-1201 spectrophotometer is used. It is a single beam spectrophotometer operating in the wavelength range of 200-1100 nm covering ultraviolet (UV) and visible (VIS) regions of spectrum. The radiation sources are a deuterium and a tungsten halogen lamp in order to obtain UV and VIS light, respectively. The grating of Shimadzu UV-1201 allow to obtain a resolution of 0.1 nm. The optical transmission data for AIS thin films were recorded between the wavelength values of 300 and 1100 nm with 1 nm wavelength resolution at a scan speed of about 200 nm/minute.

3.6 Electrical and Photoelectrical Characterization of Thin Films

The electrical and photoelectrical characterization procedure includes the measurements of dark resistivity, illumination intensity dependent photoconductivity at different bias voltages and wavelength dependent photoconductivity at different bias voltage with standard dc-measurement technique implemented on the deposited AIS thin films in van der Pauw geometry.

In order to obtain temperature dependencies of all measurements, the deposited thin film samples were mounted carefully onto a cold head part of a Janis Liquid Nitrogen VPF series cryostat (as seen in Fig. 3.6) and all measurements were performed under a vacuum condition at which about 1.33 x 10^{-1} Pa pressure value was attained inside the cryostat system for the sake of avoiding heat exchange with environment. Temperature dependent measurements were carried out between temperature values of 100 and 450 K with 10 K increments. The vacuum environment within cryostat system was maintained by an Ulvac Rotary pump and addition of liquid nitrogen to the trap part through fill port provided cooling of the cold head down to around 77 K temperature value. The temperature of the thin film samples were measured by a GaAlAs diode sensor attached to the cold head. Furthermore, a LakeShore 331 temperature controller was used to manipulate the temperature of the samples inside the cryostat.

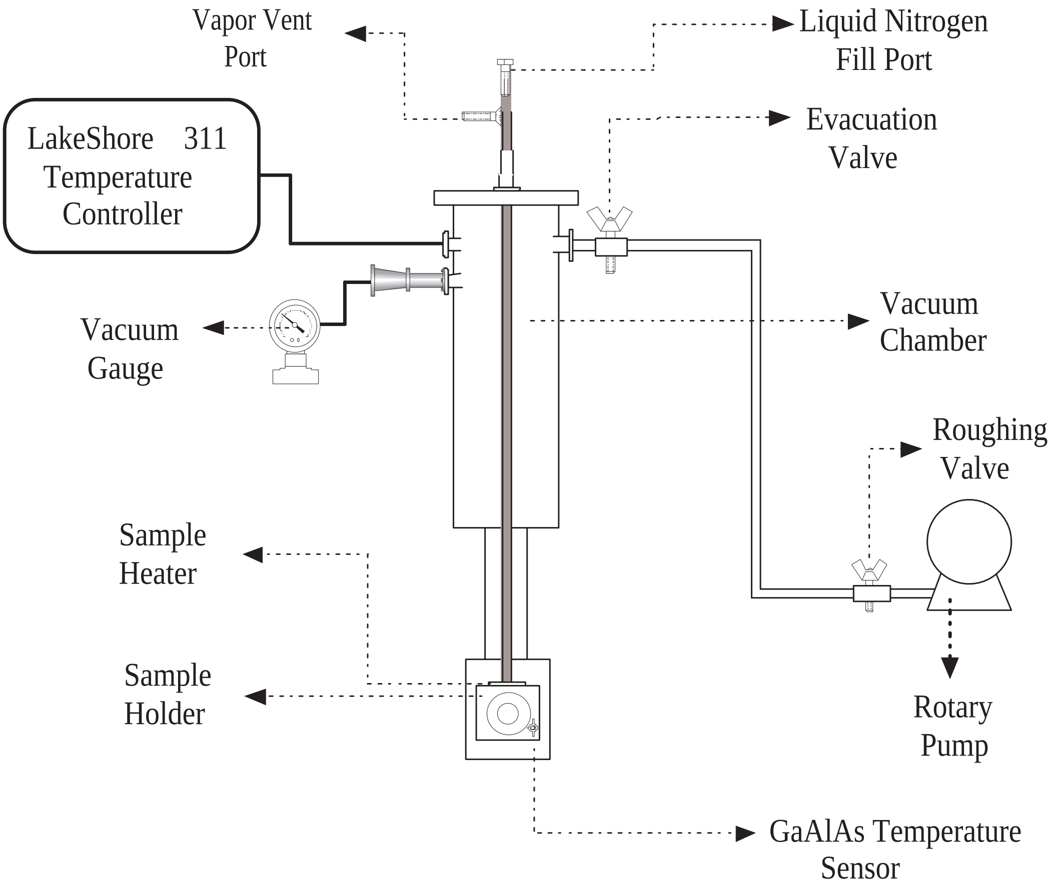

Figure 3.6: The illustration of the Janis liquid nitrogen, sample-in-vacuum type cryostat.

In making resistivity measurements, there are some sources of interference that may cause false readings of the experimental resistivity results. Therefore, a series of precautions related to these interference sources should be taken as follows;

- The measurements should be in a dark chamber and any unintentional sources of light should be blocked to enlighten the sample. Especially for highly resistive materials, the observed resistivity can drastically be influenced by a photoconductive effect.

- The observed resistivity can also severely be affected by minority-carrier injection to the material through metallic contacts during the measurement. This interference effect is detected by checking whether the current-voltage characteristics within the measurement range has a linear behavior or not. If there is no such effect, the current-voltage characteristics has a linear trend, in other words, there is no change observed in resistivity of the material. This means that, this condition imposes to obtain ohmic contacts to the material under investigation.

- The current values should be small enough to avoid the semiconductor sample from resistive heating during measurement since the resistivity of semiconductors is significantly sensitive to temperature.

- The appropriate electrical shielding should be maintained to avoid artificial currents induced from possibly existing generators near the sample.

- In resistivity measurements for high-resistivity samples, possible current leakage paths in some other parts of the circuit require particular attention. Therefore, wires, switches, cables, connectors etc. should be carefully checked in order to prevent shunting some of the applied current around the sample. In addition, the length of connection cables and wires should be as short as possible in order to avoid high lead capacitance values which might possibly increase the required time of measurement.

3.6.1 Resistivity Measurements

Resistivity (ρ) of a material is defined as the ratio of the potential gradient along the applied current flowing in the material to the current density and has the SI unit of Ohm $\cdot$ meter ($\Omega \cdot$ m), however, in resistivity measurements it is convenient to use the unit of Ohm $\cdot$ centimeter ($\Omega \cdot$ cm).

In van der Pauw resistivity measurement technique, precise knowledge of thin film thickness is a requirement. Therefore, the AIS thin film thicknesses were successfully determined by three different techniques as mentioned in Section 3.4.1. Then, all combinations of metallic contact pairs were checked for ohmicity requirement by linear current-voltage characteristics in both polarities. Afterwards, thin film samples were mounted on the cold head of cryostat system.

In order to measure the temperature, current and voltage values, a LakeShore-331 temperature controller, a Keithley 619 electrometer and a Keithley 2001 electrometer were utilized, respectively. Furthermore, a constant current value was supplied between the combinations of contact pairs by means of a Keithley 220 programmable current source. All measurement instruments were automated by a computer using a specially written software prepared in LabVIEW graphical programming language. In a typical automated resistivity measurement, the measurement of sample temperature is followed by application of constant current whose magnitude is an input parameter of desired value for the software. Afterwards, the voltages $V_{12,34}$, $V_{21,34}$, $V_{23,41}$, $V_{32,41}$, $V_{34,12}$, $V_{43,12}$, $V_{14,23}$ and $V_{41,23}$ are measured and recorded. In the designated notation, $V_{12,34}$ refers to the measured potential difference V_3-V_4 between the contact pair of 3 and 4, when constant applied current enters the contact 1 and leaves the sample through contact 2. Finally, the sample temperature is measured again for checking for a possible temperature change. If there exists a difference between two temperature values, program repeats the voltage measurements after a pre-determined time period so that the sample temperature stabilization is maintained. The illustration of the used experimental setup for resistivity measurements is given in Fig. 3.7 and the corresponding switch combinations of the switch box are tabulated in Table 3.1.

The calculation of resistivity of the AIS thin films was based on the theorem stated by van der Pauw [81] as

$$exp(-\frac{\pi t R_{12,34}}{\rho}) + exp(-\frac{\pi t R_{23,41}}{\rho}) = 1 \tag{3.1}$$

where $R_{12,34}$ is defined as

$$R_{12,34} = \frac{V_3 - V_4}{I_{12}} \tag{3.2}$$

in which current flows from contact 1 to contact 2.

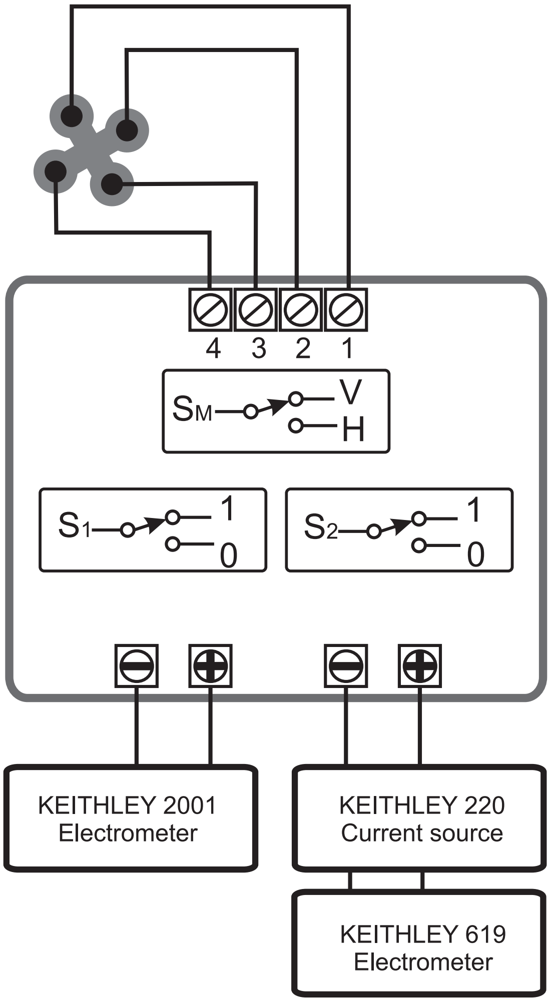

Figure 3.7: Schematic diagram of the experimental setup for resistivity measurements of AIS thin films by means of van der Pauw method.

Table 3.1: Combination of the measured potential differences with respect to the switch positions and applied currents between contact pairs in the resistivity measurements performed by means of the experimental setup shown in Fig. 3.7.

Switch Positions			Applied Current	Measured Potential Difference	
S$_M$	S$_1$	S$_2$	(Keithley 220)	(Keithley 619)	(Keithley 2001)
V	0	0	I_{12}	V_{12}	V_{34}
V	0	0	I_{21}	V_{12}	V_{34}
V	0	1	I_{32}	V_{32}	V_{14}
V	0	1	I_{23}	V_{32}	V_{14}
V	1	0	I_{14}	V_{14}	V_{32}
V	1	0	I_{41}	V_{14}	V_{32}
V	1	1	I_{34}	V_{34}	V_{12}
V	1	1	I_{43}	V_{34}	V_{12}

Furthermore, this theorem allows the calculation of sample resistivity from the obtained data by means of taking the average of two sets of equations deduced from Eqn. 3.1 as follows

$$\rho_A = \frac{\pi}{2ln(2)} \frac{t}{I} f_A [V_{21,34} - V_{12,34} + V_{32,41} - V_{23,41}] \tag{3.3}$$

and

$$\rho_B = \frac{\pi}{2ln(2)} \frac{t}{I} f_B [V_{43,12} - V_{34,12} + V_{14,23} - V_{41,23}] \tag{3.4}$$

where t is the thickness of the film in centimeters (cm), I is the magnitude of constant applied current in amperes (A), f_A and f_B are the geometrical correction factors [82]. The unit of the voltage differences is in volts (V) and the values of correction factors for symmetrically placed contacts are taken as $f_A \sim 1$ and $f_B \sim 1$. The equality of ρ_A and ρ_B within ± 10% assures the homogeneity and uniformity of the sample under investigation, otherwise a more uniform thin film should be deposited to measure resistivity correctly. As a final step, the average value

$$\rho_{av} = \frac{\rho_A + \rho_B}{2} \tag{3.5}$$

gives the average resistivity of the thin film sample in $\Omega \cdot$ cm.

3.6.2 Photoconductivity Measurements

The photoconductivity measurement on thin film semiconductors is one of most versatile optical characterization tools in order to obtain desired information about the nature of recombination processes for the semiconductors and the location of defect energy levels within forbidden energy band gap. The measurement basically involves the observation of reduction in bulk resistivity of semiconductor materials upon incidence of light, whose wavelength is short enough to be absorbed, in proportion to light intensity. In other words, the main focus of the photoconductivity measurements is the change in bulk semiconductor resistance arising from the optical excitation of excess carriers in the materials.

In this work, for AIS thin films the photoconductivity measurements as a function of illumination intensity, temperature were carried out within the Janis liquid nitrogen cryostat at five distinct light intensities of 17, 34, 55, 81 and 113 mW/cm^2 between the temperature range of 100 and 450 K. The AIS thin films were illuminated by a 12-watt halogen lamp whose spectrum comprises a relatively long wavelength range to ensure the optical excitation in samples. The different illumination intensities were obtained by changing the magnitude of applied current through the lamp between 50 and 90 mA by 10 mA-increment by means of a Keithley 220 programmable current source. Furthermore, these intensity values were measured by an ILFord 1700 radiometer at the specified applied current magnitudes.

The photoconductivity measurements on AIS thin films included the dark current measurements at the constant electric field of 105 V/cm, which was supplied by the application of a bias voltage between contact 1 and contact 3 and symmetrically between contact 2 and contact 4 by means of a Keithley 2400 sourcemeter, and the subsequent photocurrent measurements at each different light intensities. All measurements were automated by means of a specifically written computer program in LabVIEW graphical programming language, by which a standard illumination time was guaranteed as well as the reduced experimental errors.

3.6.3 Spectral Photoresponse Measurements

The spectral photoresponse measurements are nothing but the photoconductivity measurements performed at fixed wavelength of light illumination, or the photoconductivity measurements as a function of the wavelength of the incident light.

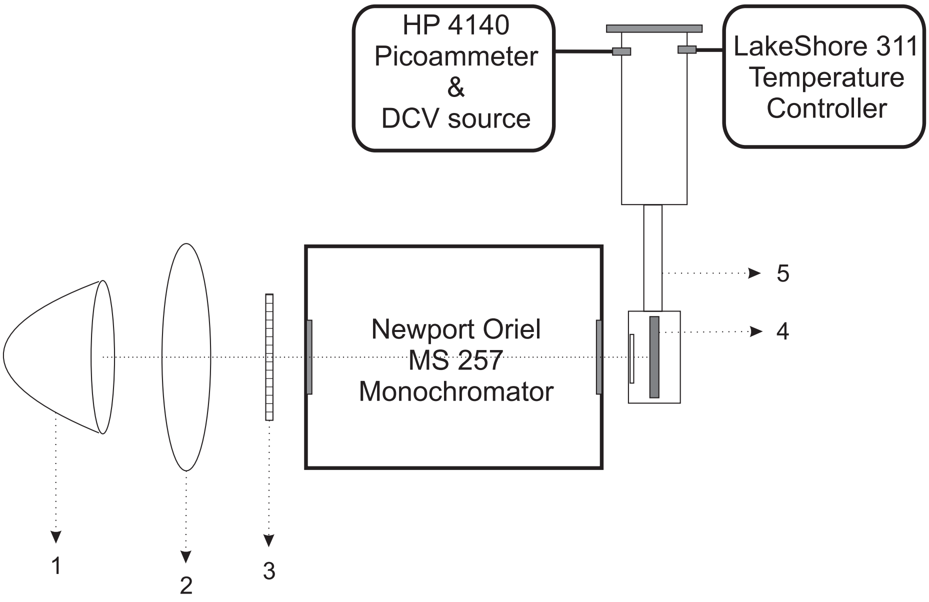

Figure 3.8: The schematic diagram of the experimental setup for the spectral photoresponse measurements of AIS thin films. All measurement devices and monochromator are controlled by a computer. 1. Concave mirror inside which a halogen lamp exists, 2. collimating lense, 3. shutter, 4. thin film sample and 5. Janis cryostat.

The photoresponse measurements of the AIS thin films were carried out within the Janis cryostat between the temperatures of 100 and 450 K under different applied bias voltages. The radiated light from a 150 W-halogen lamp was collimated through a lens. The collimated beam of light was directed into a Newport Oriel MS257 monochromator equipped with a 1200 lines/mm diffraction grating. The resulting monochromatic light having a wavelength between the range of 400 and 1000 nm was projected on the thin film samples through the quartz optical window of the cryostat.

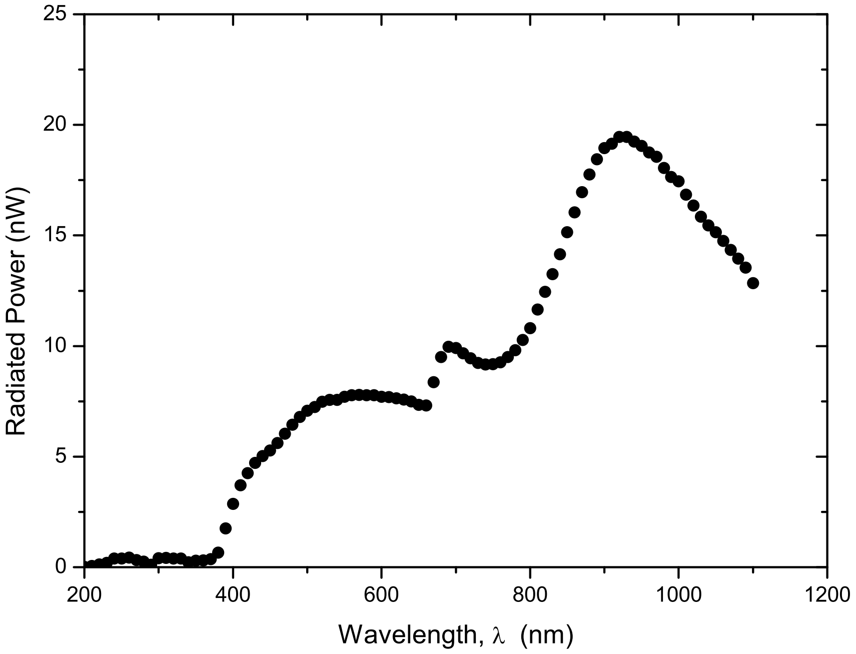

Figure 3.9: The power spectrum of the light reaching the thin film samples after passing through the optical setup of spectral photoresponse measurements.

The schematic diagram for the measurement setup is given in Fig. 3.8. The application of bias voltage and the measurement of photocurrent were performed by a HP 4140 picoammeter/DC voltage source. The illumination time was adjusted by means of a computer controlled shutter. Additionally, all the measurements and controlling the devices were maintained by means of a computer software written in LabVIEW language. Finally, the obtained photoresponse spectra was then corrected for the spectral distribution of the light source used for the illumination. The power spectrum of the light radiated by the halogen lamp was obtained by means of a Newport powermeter as given in Fig. 3.9.

CHAPTER 4

RESULTS AND DISCUSSIONS

4.1 Introduction

This chapter introduces and explores the physical properties of Ag-In-Se (AIS) ternary semiconductor thin films deposited by e-beam evaporation and presents the experimental data obtained as a result of structural, optical and electrical characterization through various experimental techniques, such as X-ray diffraction, optical transmission, and temperature dependent conductivity measurements. Furthermore, the scope of the chapter encloses the evolution of these physical properties of AIS thin films, which is described in detail, after the films are annealed under an inert gas atmosphere at different temperatures.

4.2 Structural Characterization of Ag-In-Se Thin Films

4.2.1 XRD and EDS Measurements

The results of the EDS measurements showed that the thin films deposited by the e-beam evaporation of the $Ag_3In_5Se_9$ single crystal are composed of silver, indium and selenium atoms in both as-grown and annealed forms of the samples. Trace of any impurity atoms was not detected as seen in Fig. 4.1. The atomic percentages obtained from the quantitative analysis of EDS spectra are tabulated in Table 4.1. As far as the stoichiometry of the $Ag_3In_5Se_9$ single crystal is concerned, there is a significant silver loss in the Ag-In-Se (AIS) composite thin film structure which happened during the deposition cycle. As the annealing temperature increases, the systematic decrease in the atomic percentage of selenium indicates the possible segregation of selenium atoms and/or re-evaporation from the thin film surface due to the high vapor pressure of selenium. Also, a decrease in the atomic percentage of silver content in the structure was observed.

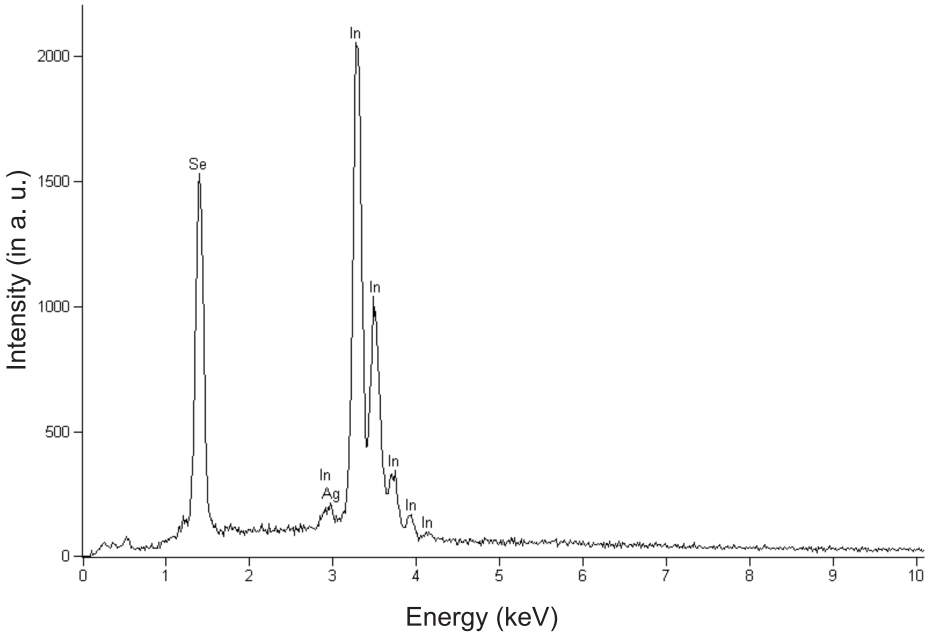

Figure 4.1: The EDS pattern of the as-grown Ag-In-Se thin films.

X-ray diffraction (XRD) measurements were performed on the AIS thin films deposited by e-beam evaporation in order to identify the properties of bulk structure of the films. In this manner, the knowledge of crystalline structure and a complete list of XRD peak positions and corresponding intensities for the single crystal source material of $Ag_3In_5Se_9$ crystal are required as references to study on the obtained diffractograms for the thin films. Although there are some theoretical and experimental works on structural properties of $Ag_3In_5Se_9$ ternary chalcopyrite single crystals [11,41], they are still devoid of complete set of crys-

Table 4.1: The results of quantitative EDS analysis for the $Ag_3In_5Se_9$ single crystal source and the AIS thin films

	Atomic Percentage (%)		
T_A (°C)	Ag	In	Se
$Ag_3In_5Se_9$ Source	18 ± 1	29 ± 1	53 ± 1
As-Grown	2 ± 1	37 ± 1	61 ± 1
200	2 ± 1	40 ± 1	58 ± 1
300	1 ± 1	42 ± 1	57 ± 1
400	1 ± 1	43 ± 1	56 ± 1

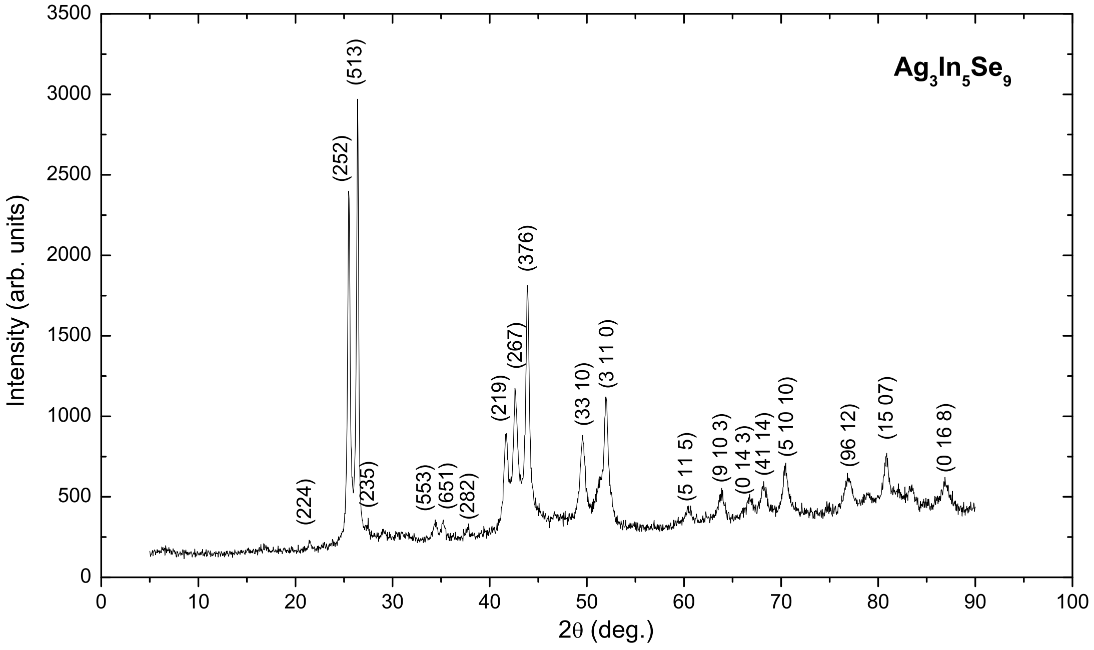

Figure 4.2: The XRD diffractogram of the $Ag_3In_5Se_9$ single crystal used as the evaporation source material.

tal data. Due to this fact, the XRD measurement was made on $Ag_3In_5Se_9$ single crystal in powdered form as a first attempt to reveal the structural properties of the thin films (see Fig. 4.2). Indexing procedure of the peak positions corresponding to reflections from atomic planes was maintained by means of "Treor90" computer software designed for XRD measurements. Additionally, "Checkcell"

Table 4.2: The structural parameters calculated by means of computer software Treor90 for the $Ag_3In_5Se_9$ single crystals used as a powder source to deposit the thin films

Peak No.	h	k	l	2θ (deg.) (observed)	2θ (deg.) (calculated)	Lattice spacing d (Å) (observed)	Lattice spacing d (Å) (calculated)
1	2	2	4	21.47	21.71	4.12	4.09
2	2	5	2	25.51	25.51	3.49	3.49
3	5	1	3	26.39	26.29	3.38	3.39
4	2	3	5	27.50	27.41	3.24	3.25
5	5	5	3	34.40	34.35	2.61	2.61
6	6	5	1	35.21	35.24	2.55	2.55
7	2	8	2	37.83	38.07	2.38	2.36
8	2	1	9	41.68	41.77	2.17	2.16
9	2	6	7	42.62	42.52	2.12	2.12
10	3	7	6	43.89	43.76	2.06	2.07
11	3	3	10	49.55	49.36	1.84	1.85
12	3	11	0	51.95	51.99	1.76	1.76
13	5	11	5	60.42	60.35	1.53	1.53
14	9	10	3	63.97	63.99	1.45	1.45
15	0	14	3	66.75	66.78	1.40	1.40
16	4	1	14	68.21	68.25	1.37	1.37
17	5	10	10	70.43	70.42	1.34	1.34
18	9	6	12	76.87	76.78	1.24	1.24
19	15	0	7	78.96	79.03	1.21	1.21
20	5	16	2	80.87	80.92	1.19	1.19
21	0	16	2	82.09	82.12	1.17	1.17
22	2	10	14	83.42	83.49	1.16	1.16
23	0	16	8	86.85	86.88	1.12	1.12

software supplied the information of site symmetry and space group to which $Ag_3In_5Se_9$ belongs. As a result of these calculations it was found that $Ag_3In_5Se_9$ crystal belongs to the space group of P4mm with site symmetry of C_{4v}^1 which agrees with the results in the work of Parlak et. al [41] and has tetragonal lattice structure together with lattice constants of a : 6.980, b : 6.980 and c : 20.055 Å. The indexed peak positions and calculated lattice parameters are listed in Table 4.2 and can be seen from Fig. 4.2. This plausible indexing result can only be obtained by the exclusion of a few weak-intensity diffraction lines appeared in the diffractogram of powder source.

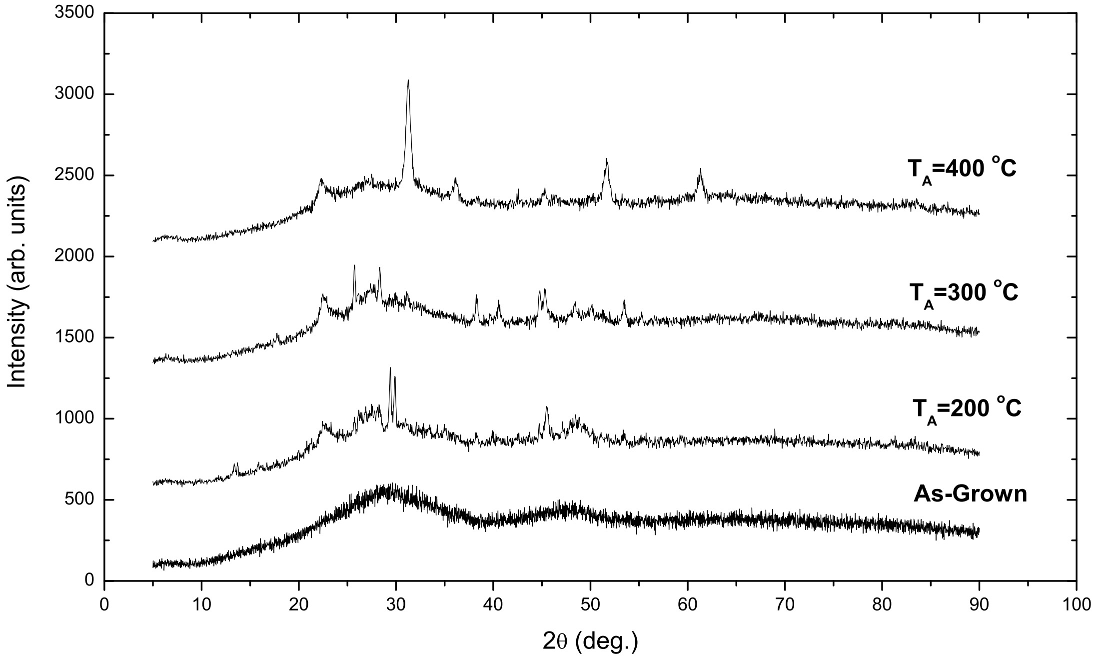

Figure 4.3: The XRD patterns of the as-grown and annealed AIS thin films at different temperatures.

The XRD measurements indicate that the AIS thin films deposited at the substrate temperature of 110 °C have amorphous structure in the as-grown form. In other words, the XRD diffractograms of the as-grown films do not include sharp peaks that are characteristic property of crystalline materials, but rather broad intensity hills indicating that the structure is in between amorphous and polycrystalline phase. Moreover, after the application of subsequent post-annealing process on thin films at 200, 300 and 400°C under nitrogen atmosphere for 30 minutes, the deposited thin films possess polycrystalline structure as shown in Fig. 4.3 and 4.4. In other words, AIS thin films are transformed from amorphous nature into polycrystalline one by means of annealing at 200 °C for 30 minutes. When the 2θ and intensity values of the peaks of XRD pattern corresponding to annealed thin films at 200 °C are compared with appropriate XRD data sets from ASTM database and data set prepared in Table 4.2, it is understood that

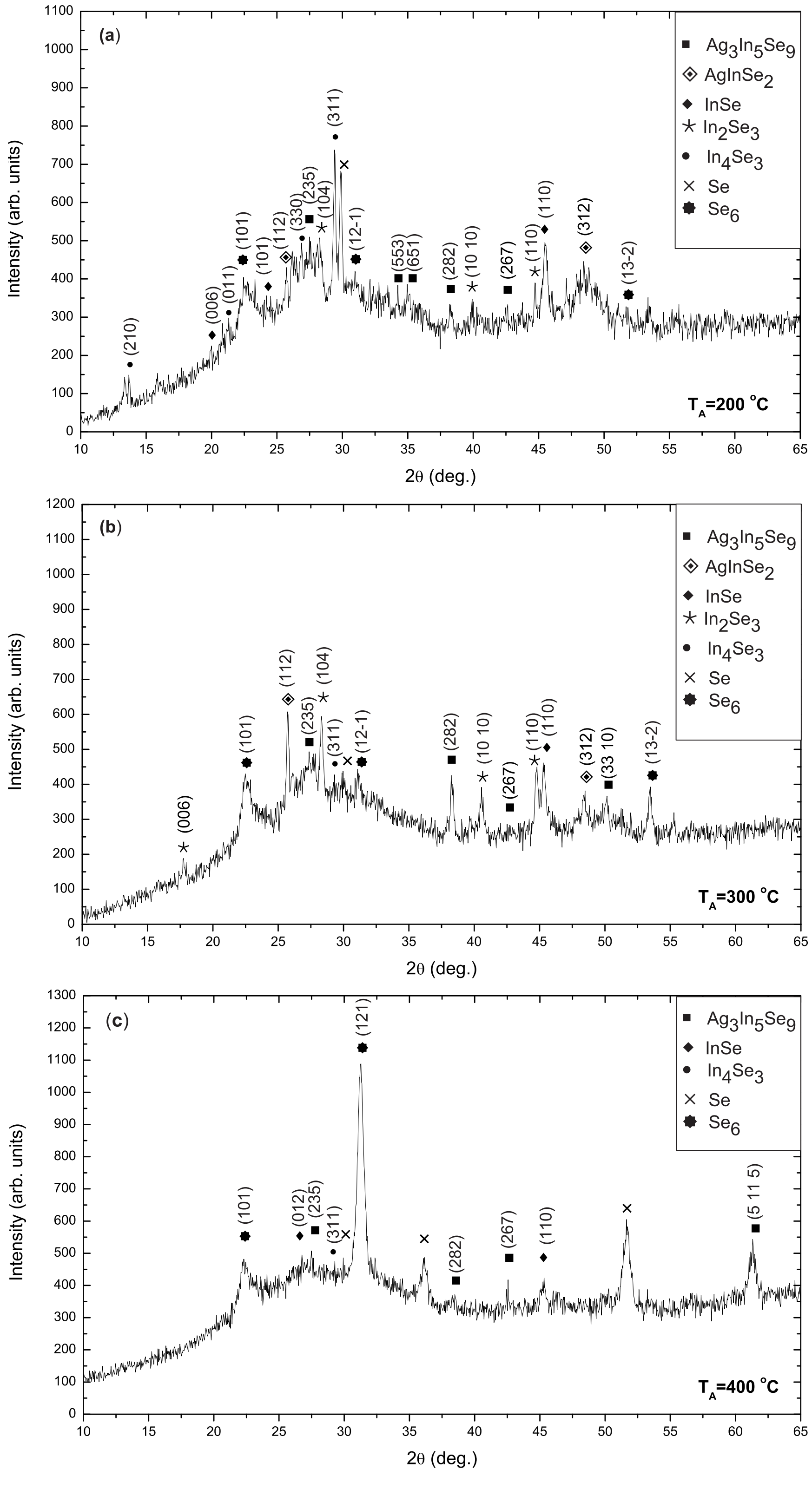

Figure 4.4: The XRD patterns of the multi-phase AIS thin film structure after annealing at a) 200, b) 300 and c) 400°C.

the thin films consist of a mixture of crystalline phases (ternary, binary and single) of the constituent atoms of powder source; Ag, In and Se. According to complete XRD data sets, AIS thin films exhibit multi-phase structure with the contribution of $Ag_3In_5Se_9$ ternary chalcopyrite compound with tetragonal crystal structure (lattice constants are a : 6.980, b : 6.980 and c : 20.055 Å), $AgInSe_2$ ternary chalcopyrite phase with tetragonal crystal structure (lattice constants are a : 6.090, b : 6.090 and c : 11.670 Å), In_4Se_3 binary compound with orthorhombic crystal structure (lattice constants are a : 15.296, b : 12.308 and c : 4.081 Å), In_2Se_3 binary compound with hexagonal crystal structure (lattice constants are a : 4.050, b : 4.050 and c : 28.770 Å), InSe binary compound with hexagonal crystal structure (lattice constants are a : 4.000, b : 4.000 and c : 25.320 Å), Se_6 compound with hexagonal crystal structure (lattice constants are a : 11.400, b : 11.400 and c : 4.470 Å) and Se [83]. After the identification of the present crystalline phases the peaks are indexed according to these XRD data sets. Fig. 4.4 shows the present phases and indexed peaks for XRD patterns of thin films annealed at 200, 300 and 400°C. The structure of the thin films annealed at 200 °C is dominated by In_4Se_3, InSe and Se compounds as far as the intensity of the characteristic peaks are concerned. Further annealing at 300°C changes this structural existence significantly and are composed mainly of $Ag_3In_5Se_9$, $AgInSe_2$, In_2Se_3 and InSe. A very similar phase transition scheme in thin films was also observed after heat treatment at specific temperature values in the works of Biswas et. al [84] and Fitzgerald et. al [85]. In view of the decrease in peak intensity of In_4Se_3 and the increase in the intensity of these compounds it can be interpreted that the In_4Se_3 crystallites dissociate within thin film structure while the crystallinity of $Ag_3In_5Se_9$, $AgInSe_2$, In_2Se_3 and InSe compounds improves. Furthermore, annealing the multi-phase AIS thin films yields the development of Se_6 and Se crystalline phases while suppressing the previous dominant compounds to diminish. The dominant Se_6 and Se existence in the structure of 400 °C-annealed samples is the most important indication of the segregation of Se atoms within the film structure [86]. Because, the segregation of Se atoms toward the thin film surface enables the chance for Se atoms to aggregate forming the Se-rich regions within the thin film structure. Furthermore, the segregation of Se atoms results in the relative motion of Ag atoms away from the film surface yielding the formation of new phases.

4.2.2 XPS Measurements

The surface and near-surface atomic composition and the present chemical environments covering binding and oxidation states of multi-phase AIS thin films were investigated by means of XPS measurements performed on as-grown and annealed films at different temperatures. The acquired XPS survey spectrum for the as-grown thin films can be seen in Fig. 4.5. The XPS survey spectra were obtained using the constant pass-energy (CAE) mode with a pass energy of 48 eV and the surfaces of the films were sputtered by ions to remove adventitious carbon (C) and oxygen (O) atoms deposited onto the surface accidentally from the environment. Due to charging effects, the C 1s photoelectron peak at 285.0 eV was used as a reference for the charge-correction of binding energies of core levels and Auger peaks. By means of experimentally determined binding energy values, the elements present at and near the surface of the as-grown films were identified as Ag, In, Se and adventitious C and O. However, after sputtering the surface, C 1s signal was significantly reduced to background level while O content was not eliminated completely. Moreover, the relatively horizontal shape of the background signal, which is produced by photoelectrons encountering kinetic energy loss as a result of the inelastic scattering, indicated a sufficiently clean surface structure [87]. On the contrary, XPS survey spectra obtained after the annealing the films at different temperatures showed slightly positive slope for background signal due to C and O contaminations on the surfaces of the films as seen from Fig. 4.6.

As shown in Fig. 4.6, post annealing process on the as-grown AIS thin films has a serious effect on the intensities of Se3d, Se3p and O1s photoelectron peaks in the XPS data. As the annealing temperature is increased, the Se3d and Se3p peak intensities becomes smaller and especially after annealing the films at 300°C,

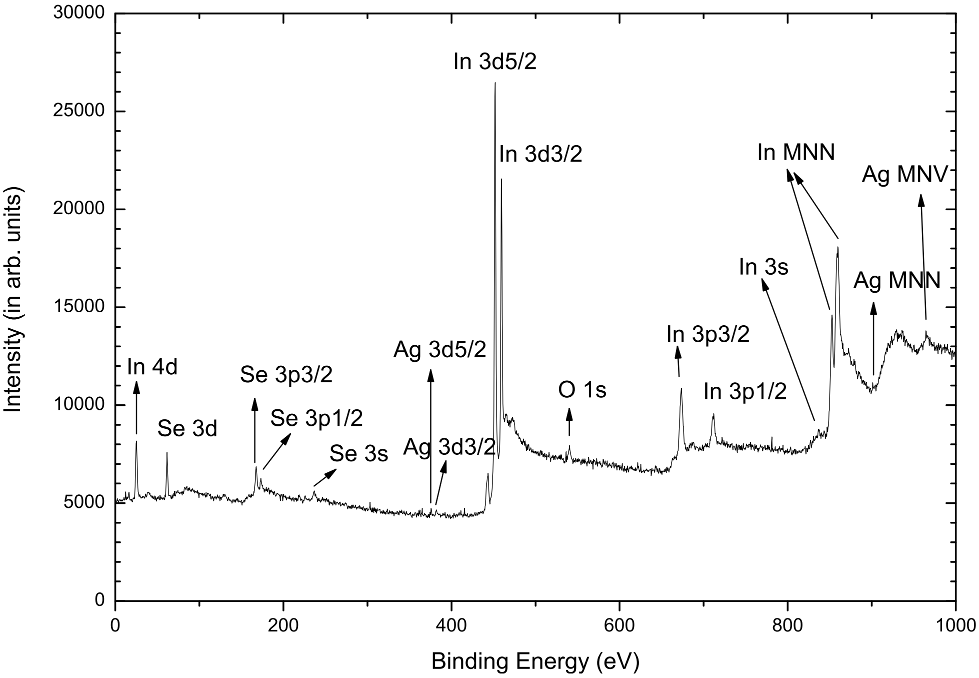

Figure 4.5: XPS spectrum of e-beam evaporated as-grown AIS thin film.

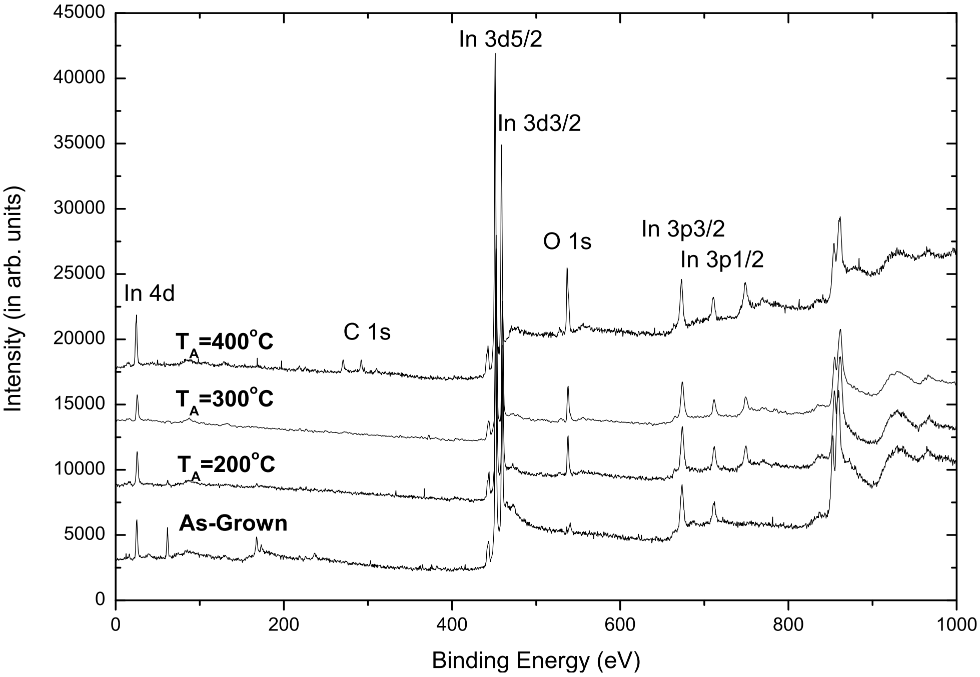

Figure 4.6: The XPS spectra of the as-grown and annealed AIS thin films at different temperatures.

the Se photoelectron peaks vanish. This interesting situation is an evidence for Se segregation and/or reevaporation from the thin film structure, which will be discussed later. Furthermore, increasing annealing temperature increases the intensity of O1s peak consistently. This indicates that although the annealing process is performed under nitrogen atmosphere, increasing ambient temperature causes the oxidization of thin film surface adventitiously.

The important part of the information obtained from the XPS spectrum is contained in the valence band region with low binding energy values. Therefore, the compositional analyses were based on the measured In 4d and Se 3d core level spectra. Also, Ag 3d and In 3d core levels were investigated because of being the main XPS signal for the elements of interest.

The detailed peak shape analysis of the core level spectra for the purpose of the decomposition of photoelectron peaks of the elements includes the removal of the background, which appears due to inelastically scattered photoelectrons, by applying Tougaard background model [88]. The measured photoelectron peaks were numerically fitted by accepting the type of fitting functions as a convolution-type of Gaussian and Lorentzian functions.

Fig. 4.7 shows the evolution of In 4d photoelectron peak after annealing the thin films at 200, 300 and 400°C. The emissions of photoelectrons from In $4d_{5/2}$ and In $4d_{3/2}$ levels can not be resolved separately due to weak spin-orbital momentum interaction [89]. As seen from Fig. 4.7(a), the In 4d peak was decomposed into the three contributions corresponding to In-In metallic indium bonds, In-Se bonds and In-Ag bonds. The intensity ratio of $4d_{5/2}$ to $4d_{3/2}$ peaks have fixed value of 3:2 since the relative intensity of these components of doublets formed by the spin-orbit coupling is dependent on their relative populations or degeneracies $(2j+1)$ [87]. The fitting parameters are summarized in Table 4.3. The binding energy values obtained by means of the detailed peak fitting procedure are in very good agreement with those reported in previous studies, which are presented in Table 4.3. Since the area under the doublets is a measure of number of bonds, it can be inferred that the number of In-In metallic bonds exceeds the numbers of In-Se and In-Ag bonds for the as-grown thin films. The observation of the chemical shifts of the binding energies of the doublets corresponding to In-Ag and In-Se bonds with respect to the energy position of In-In metallic bonds is an expected phenomena. Actually, the formation of bonds for metals with elements having a higher electronegativity increases the value of positive XPS chemical shifts with respect to metallic binding energy values as observed in Table 4.3 [87]. Because, when a metal combines with electronegative element to form a compound, the inner-shell electron binding increases due to loss of valence electrons. In this manner, chemical shift due to In-Se bonding is greater than In-Ag one, since Se is more electronegative than Ag.

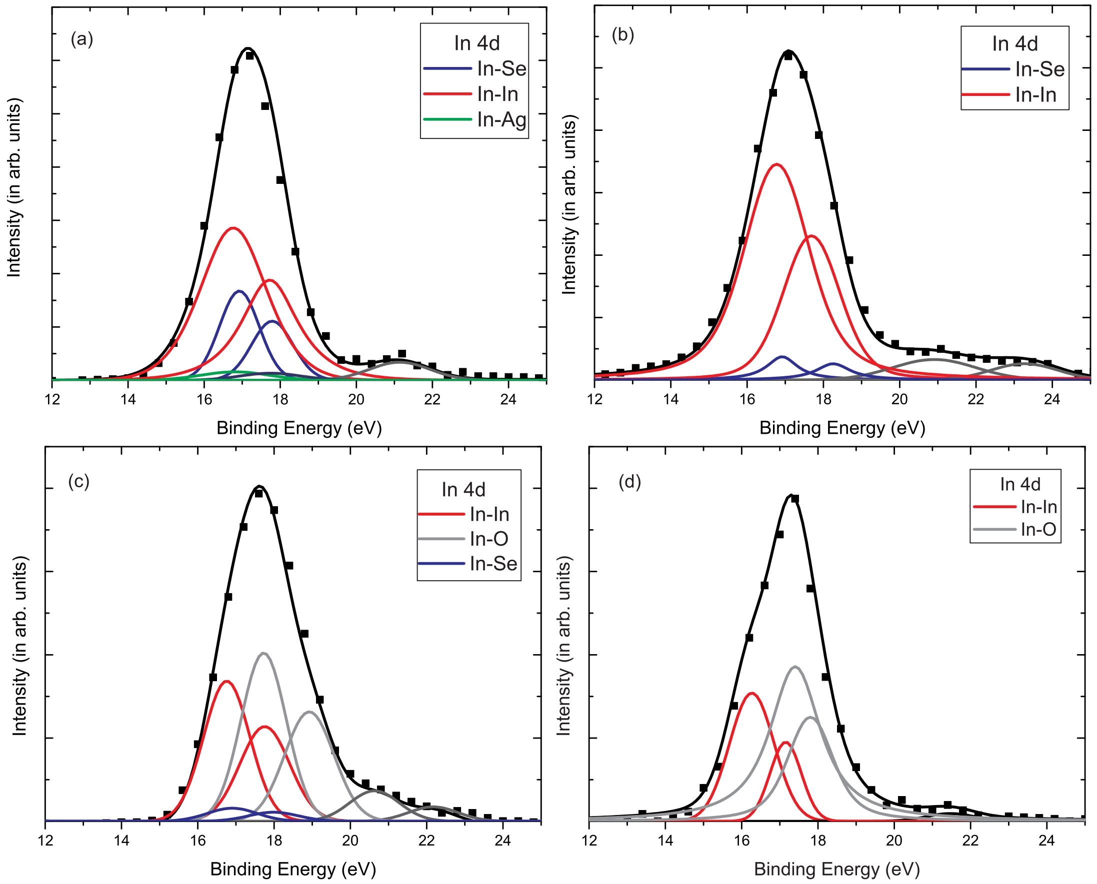

Figure 4.7: In 4d core level XPS spectra for a) as-grown AIS thin films and annealed at b) 200°C, c) 300°C and d) 400°C. The squares are the experimental data, the black solid line represents the resulting best fit.

According to the bonding scheme in Fig. 4.7, it is possible to observe a multi-

Table 4.3: Decomposition parameters of In 4d photoelectron peak with respect to $4d_{5/2}$ line

Annealing Temp. (°C)	Bonding	B.E.(eV) (Observed)	B.E. (eV) [Ref.]	Spin-Orbit (eV) (Observed)
As-Grown	In-In	16.7	16.74 [90]	1.0
	In-Ag	16.8	-	1.0
	In-Se	16.9	16.9 [91]	0.9
200	In-In	16.8	16.74 [90]	1.1
	In-Ag	-	-	-
	In-Se	16.9	16.9 [91]	1.3
300	In-In	16.8	16.74 [90]	1.0
	In-Ag	-	-	-
	In-Se	16.9	16.9 [91]	1.1
	In-O	17.7	17.8 [92]	1.2
400	In-In	16.3	16.74 [90]	1.0
	In-Ag	-	-	-
	In-Se	-	-	-
	In-O	17.4	17.8 [92]	0.5

Table 4.4: Decomposition parameters of In 3d photoelectron peak with respect to $3d_{5/2}$ line

Annealing Temp. (°C)	Bonding	B.E.(eV) (Observed)	B.E. (eV) [Ref.]	Spin-Orbit (eV) (Observed)
As-Grown	In-In	444.0	444.0 [93]	7.4
200	In-In	443.9	444.0 [93]	7.6
300	In-In	445.4	444.0 [93]	7.6
400	In-In	443.8	444.0 [93]	7.6

phase thin film structure containing such as $Ag_3In_5Se_9$, $AgInSe_2$, In_2Se_3 etc, because the indium atoms are bounded to both silver and selenium atoms [94]. In fact, the same multi-phase structure of the AIS thin films was also observed in XRD analysis.

The annealing the thin films at 200°C causes a significant decrease in the number of In-Se bonds as in Fig 4.7(b). On the other hand, In-Ag bonding is diminished by the effect of the annealing. The peaks situated around 21 eV as seen in Fig 4.7(b) are most probably X-ray satellites produced by the photoelectrons encountering kinetic energy loss due to inelastic scattering by valence electrons. The post-thermal annealing of the thin films triggers the segregation mechanism of selenium, owing to high vapor pressure value, selenium atoms placed at surface can easily leave the thin film structure [86, 95, 96]. Accordingly, the signal due to Se 3d core level disappears as the annealing temperature increases as seen in Fig. 4.10. In other words, increase in the post-annealing temperature leads to chalcogen(Se)-deficient surface [95]. Further increase in the temperature of annealing increases the number of In-O bonds. This is possibly due to the filling of O atoms in empty atomic sites left by Se atoms bounded earlier to In atoms. Therefore, a positive chemical shift is observed as in Fig. 4.7(c) and (d) with respect to the binding energy of metallic In core level, since O is an electronegative element [97].

Fig. 4.8 shows the XPS signal of In 3d core level, which is the most intense photoelectron peak of In. It is observed that the binding energy position of In 3d doublet is generally shifting towards the lower energy values as the annealing temperature increases because of increasing concentration of In-O bindings due to In_2O_3-oxidized phase [98]. The parameters calculated from the decomposition procedure of the photoelectron peaks are tabulated in Table 4.4. Moreover, the 3d levels are well separated due to spin-orbit coupling into $3d_{3/2}$ and $3d_{5/2}$ components with an average energy separation of about 7.4 eV.

As mentioned above, post-annealing procedure affects significantly the bonding states and the chemical composition of the thin film surface. Fig. 4.9 shows the well separated photoemission signal from Ag 3d core levels that is the most intensive photoelectron peak of Ag and the decomposition parameters are given in Table 4.5. According to peak fitting analysis, there are three main contributions corresponding to Ag-Ag metallic bonds, Ag-Se bonds and Ag-O bonds. Due to the very low concentration of Ag-In as shown in Fig. 4.7(a), the possible contribution due to Ag-In bonding could not be seen within the tolerance of calculational errors. It is apparent that in the as-grown thin films, most of the

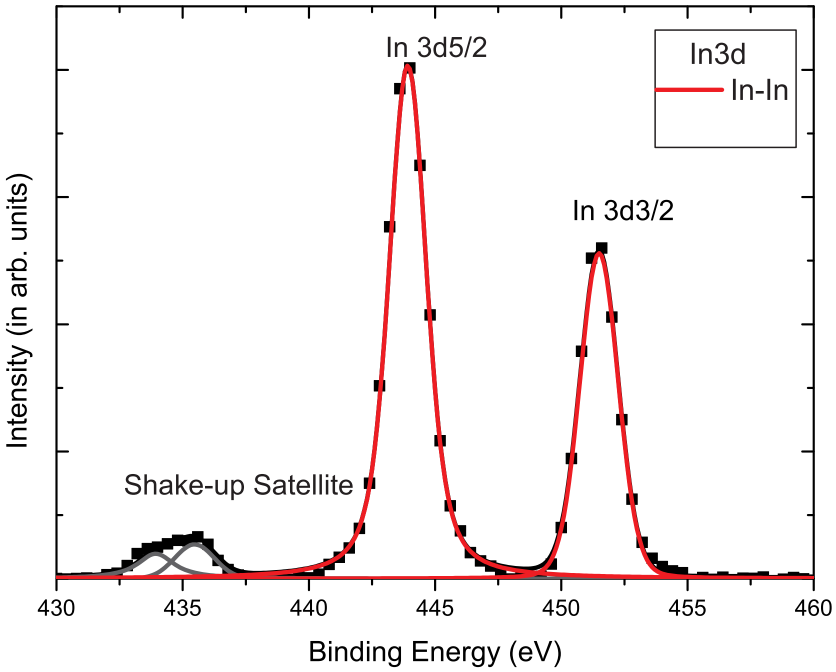

Figure 4.8: In 3d core level XPS spectra for a) as-grown AIS thin films and annealed at b) 200°C, c) 300°C and d) 400°C. The squares are the experimental data, the black solid line represents the resulting best fit.

O atoms are catched by Ag atoms to form Ag-O bonding.

The Ag-Se bonding causes a slight contraction of electronic distribution about the Ag 3d core level producing a well-defined positive chemical shift as expected. Just after annealing the thin films at 200°C produces Ag-deficient film surface as the Ag 3d signal disappears in the XPS survey spectrum. It might be the result of the relative motion of the Ag atoms away from the thin film surface due to the segregation of Se atoms, which have high diffusivity and vapor pressure, towards the surface. It is also experimentally proved that this motion of silver atoms into chalcogenide glass structures is improved by increasing the annealing temperature [102–104]. Therefore, the increase in the annealing temperature induces the Se segregation into the film surfaces while enhances the diffusivity of Ag atoms into the thin film structure together with possible bond formation

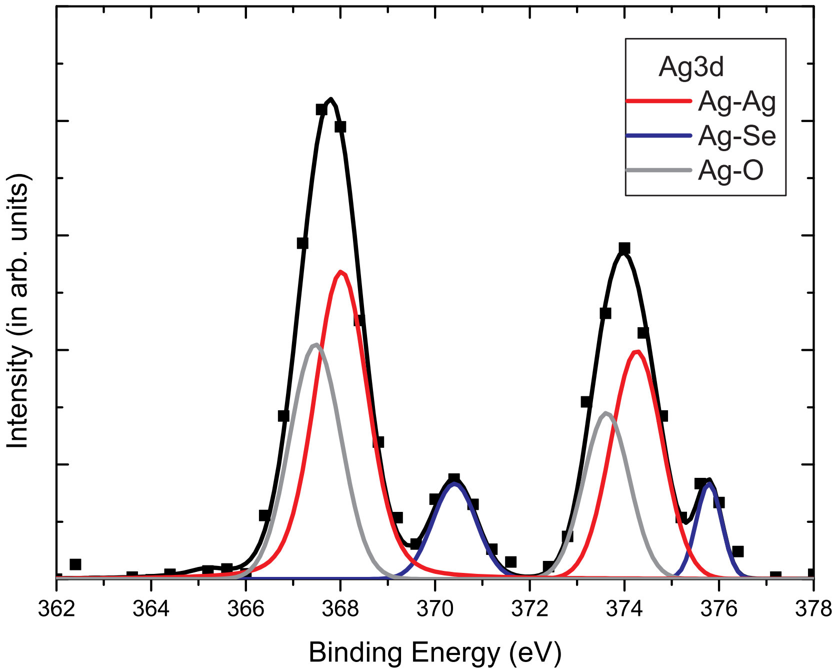

Figure 4.9: Ag 3d core level XPS spectrum for as-grown AIS thin films. The squares are the experimental data, the black solid line represents the resulting best fit.

with In atoms and segregated Se atoms within the thin films. This could also be a reason for multi-phase structure as observed in the XRD study.

As seen in Fig. 4.10, most of the Se atoms are bound to In atoms and there exists very small concentration of Se-Se bonding near the film surfaces in the as-grown form. A negative chemical shift in binding energy due to Se-In and Se-Ag bonding relative to the binding energy of Se-Se bonding is observed, because indium and silver are less electronegative than selenium. In the annealed films at 200°C the relative concentration of Se-Se bonds increases. This situation is not unreasonable because the segregated Se atoms might pile up to form Se clusters as shown in the XRD measurements, thus Se-Se and In-Se bonds after annealing at 200°C. Further increase in annealing temperature produces the loss of Se core level signal indicating the Se-deficient thin film surfaces as discussed above.

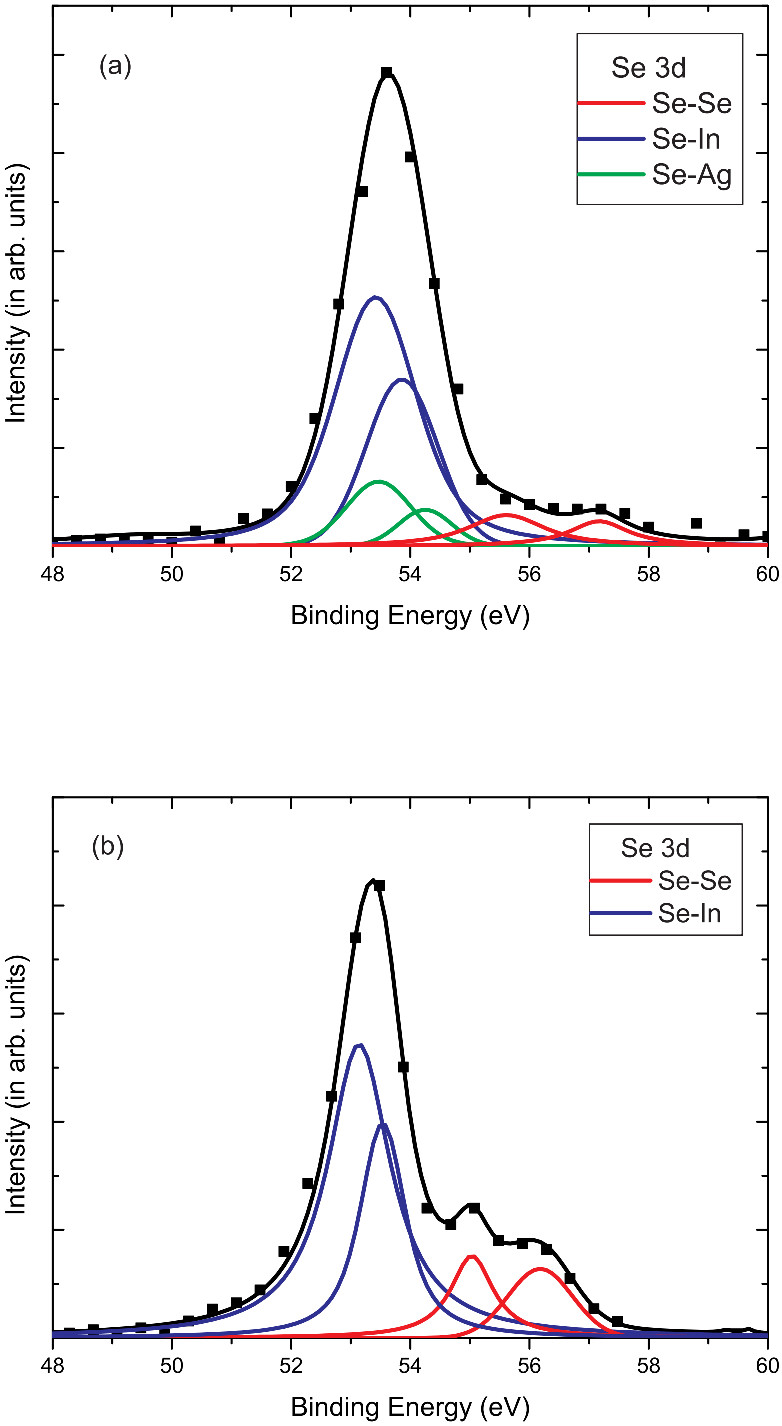

Figure 4.10: Se 3d core level XPS spectra for a) as-grown and annealed AIS thin films at b) 200°C. The squares are the experimental data, the black solid line represents the resulting best fit.

Table 4.5: Decomposition parameters of Ag 3d photoelectron peak with respect to $3d_{5/2}$ line

Annealing Temp. (°C)	Bonding	B.E.(eV) (Observed)	B.E. (eV) [Ref.]	Spin-Orbit (eV) (Observed)
As-Grown	Ag-Ag	368.0	368.1 [99]	6.2
	Ag-Se	370.3	369.0 [100]	5.5
	Ag-O	367.4	367.4 [101]	6.3

Table 4.6: Decomposition parameters of Se 3d photoelectron peak with respect to $3d_{5/2}$ line

Annealing Temp. (°C)	Bonding	B.E.(eV) (Observed)	B.E. (eV) [Ref.]	Spin-Orbit (eV) (Observed)
As-Grown	Se-Se	55.6	55.5 [105]	1.6
	Se-Ag	53.5	53.8 [100]	0.8
	Se-In	53.4	53.5 [91]	0.5
200	Se-Se	55.1	55.5 [105]	1.2
	Se-Ag	-	-	-
	Se-In	53.2	53.5 [91]	0.5

Table 4.6 lists the obtained binding energy parameters after the decomposition of Se 3d core level photoelectron peak.

4.2.3 AFM Measurements

The corresponding evolution of the surface structure of multi-phase AIS thin films upon post-thermal annealing at different annealing temperatures was monitored by means of AFM analysis. The obtained AFM images of the thin film surfaces at different annealing temperatures are shown in Fig. 4.11. The surface of the as-grown thin film is almost smooth with the root-mean-square (RMS) peak to peak value of 1.8 nm. However, after annealing the thin film the surface morphology starts to change and the RMS peak to peak distance value becomes 8.2 nm. This smoothness of the surface deteriorates due to the migration of Se atoms towards the film surface. Also, when the annealing temperature is increased further, the roughness of the film surface increases drastically along with the apparent grain formation. The RMS peak to peak values of the film surfaces becomes 15.9 and 22.9 nm for the samples annealed at 300°C and 400°C, respectively.

The annealing process results in the formation of different phases in the AIS thin films and further increase in the annealing temperature cause these phases to change as proved by XRD measurements. Fig. 4.11 shows explicitly the formation of the crystallites and the increase in the crystallite size as the annealing temperature increases. Therefore, the segregation of the Se atoms towards the surface and the growth of crystallites of different phases shown in the XRD section destroys the smoothness of the thin film surfaces and the increased surface area enhances the chance of O and C contamination of In-rich but Se-deficient thin film surface structure as observed from XPS analysis. Furthermore, there might be other reasons for increasing RMS values with annealing, such as, segregation of selenium might result in the multiphase formation including such In_2Se_3, In_4Se_3, InSe phases as observed from XRD analysis and increasing their crystallite size with annealing.

4.2.4 Thickness Measurements

The thin film thickness of AIS thin films were measured independently from three different measuring techniques.

1. *in-situ* thickness measurement during deposition of AIS thin films is made by means of an Inficon XTM/2 thickness monitor which analyzes the changes in natural oscillation frequency of quartz crystal, which is placed near substrate holder, due to thin film coating developing onto the crystal. The growth rate of thin films was maintained at $\sim 36\,\mathrm{nm/minute}$ and final deposited thin film thickness was measured as 702 ± 1 nm by means of Inficon XTM/2 thickness monitor.

2. Electromechanical thin film thickness measurement is performed by a DEKTAK 6M thickness profilometer after the deposition of AIS thin films. The

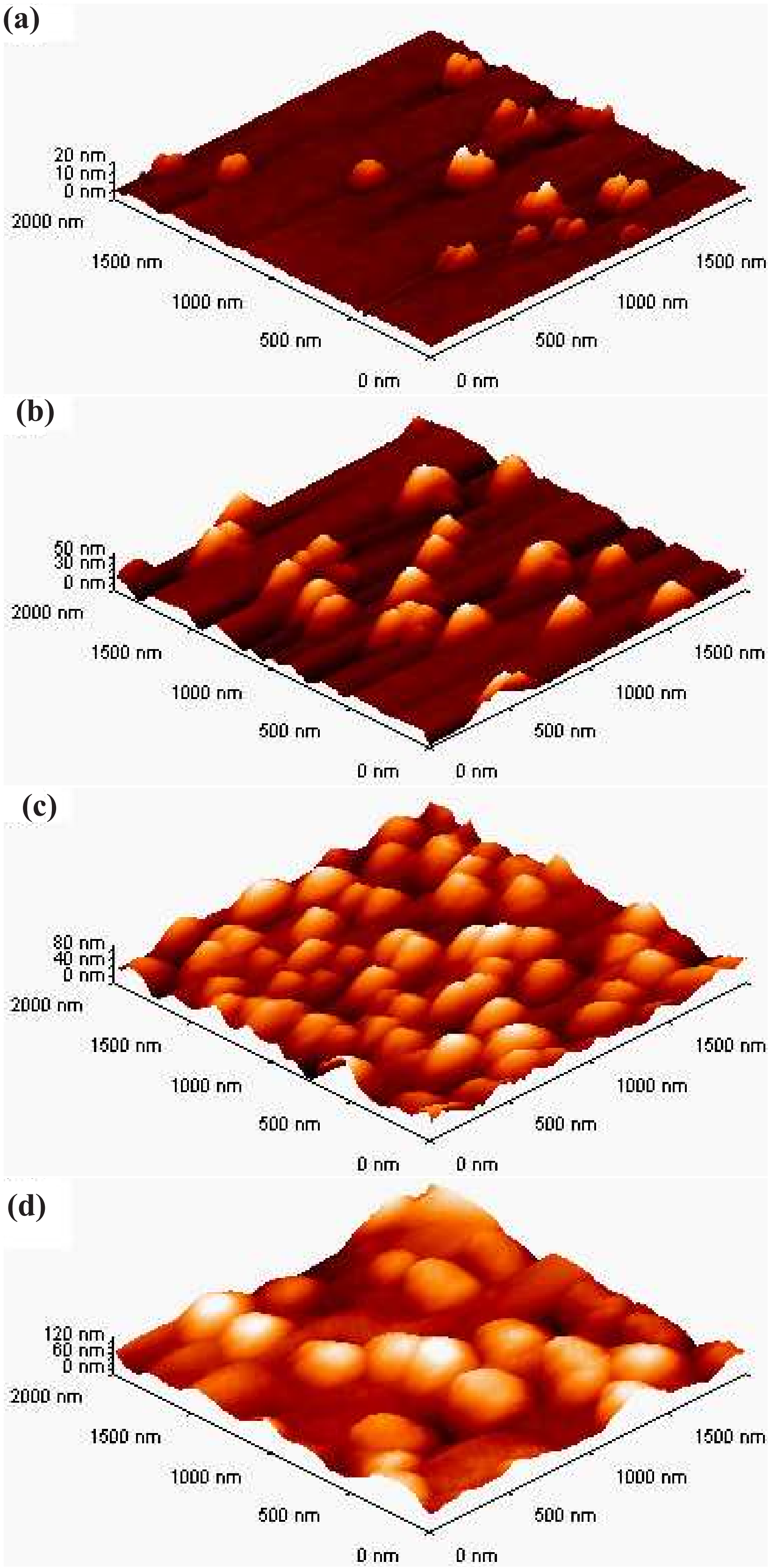

Figure 4.11: The AFM images of a) the as-grown and annealed AIS thin films at b) 200, c) 300 and d) 400°C.

thin film thickness of 710 ± 2 nm was recorded by the measurement in which a diamond stylus of 12.5 μm radius was pushed onto thin film surface with a force of 5 mg.

3. Thin film thickness measurement of AIS thin films was performed by means of optical transmittance measurements as it will be discussed in Section 4.3.1. Obtained transmission spectrum has interference fringes in the transparent region of the deposited AIS thin films. Thin film thickness was determined as 690 ± 10 nm from the analysis of the region.

Thin film thickness measuring procedure was applied to all deposited thin films having different places on the substrate holder and the thickness uniformity was verified.

4.3 Optical Characterization of Ag-In-Se Thin Films

The complete knowledge of the optical constants, i.e. refractive index, dielectric constant and absorption coefficient, over a wide wavelength (λ) range and optical bandgap values of thin films, is crucial for optimizing their optical and electrical properties especially for solar cell applications. Therefore, determination of the optical constants of e-beam evaporated absorbing AIS thin films, both as-deposited and annealed samples at different ambient temperatures, was performed by transmission measurement, since the optical transmission measurement at a specific wavelength spectrum is a simple and effective experimental method for this purpose [106–109].

Fig. 4.12 shows the optical transmission spectra of AIS thin films, both as-deposited and annealed at different temperatures under nitrogen environment, in the wavelength range of 300-1100 nm. As-grown and annealed thin films perform good transmittances together with the interference patterns in the transparent region of the spectrum. Thin films become increasingly absorbing as the incident photon energy gets greater than 1.6 eV and the magnitude of the interference fringes diminishes. Additionally, the transmittance values decrease in magnitude as the annealing temperature increases. This result is an expected result because of the Se segregation process triggered by increased annealing temperature as mentioned in Section 4.2 on the XPS, XRD and AFM results of AIS thin films [110]. Segregation of Se atoms brings about a Se-deficient but In-rich thin film surface and this pseudo-metallic thin film surface becomes more reflective.

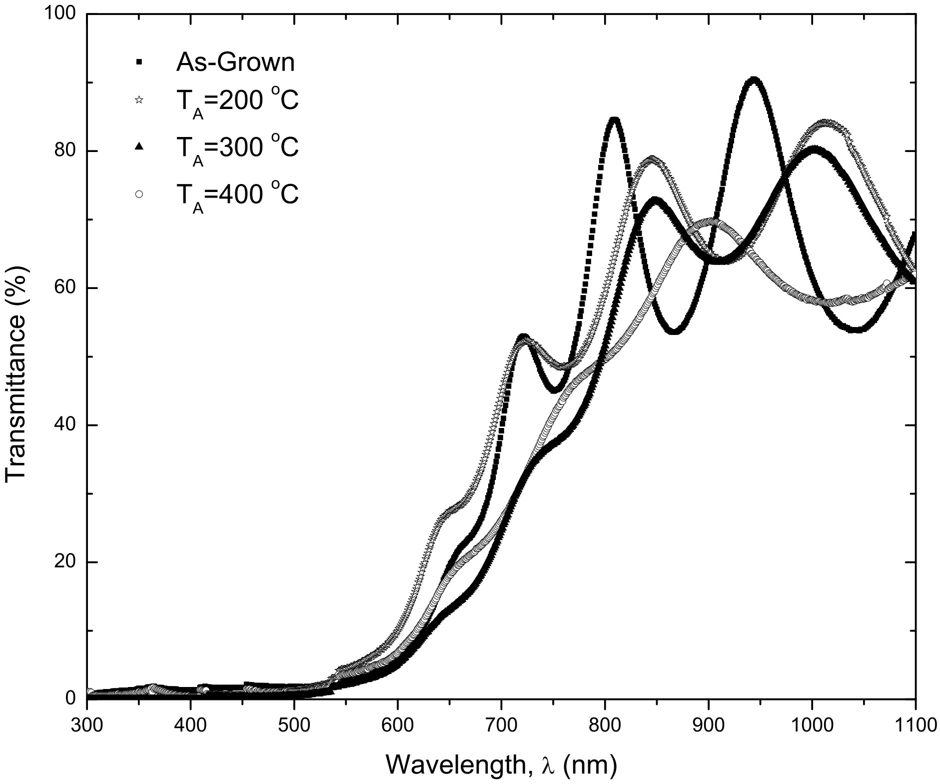

Figure 4.12: Optical transmission spectra for as-deposited and annealed AIS thin films.

The oscillatory behavior of the obtained spectrum (Fig. 4.12) due to the interference fringes produced by the reflected light waves from two surfaces of thin films indicates a well thickness uniformity for as-grown and for the films annealed at 200 and 300°C. On the other hand, for the thin films annealed at 400°C the interference fringes are disturbed significantly. That can be explained by the modification in the film structure and the surface dynamics due to Se segregation [110] as discussed in Section 4.2.

4.3.1 Optical Constants of Ag-In-Se Thin Films

The complex refractive index $\tilde{N}$ is defined as

$$\tilde{N} = n + ik \tag{4.1}$$

where n is the refractive index and k is the extinction coefficient for the thin films as a function of incident light frequency [111]. The refractive indices, n, of the films annealed at different temperatures were determined by both using the envelope method (EM) developed by Manifacier et al. [112] and Swanepoel [113, 114] and continuous wavelet transform (CWT) method [115, 116], which was first introduced by Grossman et al. [117]. EM permits the refractive index calculations of the films that exhibit at least two interference fringes in their weak absorption and transparent spectral region by constructing envelope curves of transmittance spectra. The envelopes are the two curves designated as T_M and T_m, which connect the peaks and valleys of the interference pattern in the transparent region of the transmission spectrum (normalized to unity) of the thin films, respectively, as presented in Fig. 4.13 for as-grown AIS thin films. Both envelopes merge together at the beginning of the strong absorption region where the interference fringes can no longer be observed. According to EM, the refractive index, n, is given by the following equation

$$n = \left(N + \sqrt{N^2 - n_o^2 n_s^2}\right)^{1/2} \tag{4.2}$$

where

$$N = \frac{n_o^2 + n_s^2}{2} + 2n_o n_s \frac{T_M - T_m}{T_M T_m} \tag{4.3}$$

here n_o is the index of refraction of the surrounding environment (air) which was taken as 1 and n_s is the refractive index of the ordinary glass substrate determined as 1.51 over the wavelength range of 300-1100 nm from its transmission spectrum using this relation [118]

$$n_s = \frac{1}{T_s} + \left(\frac{1}{T_s^2} - 1\right)^{1/2} \tag{4.4}$$

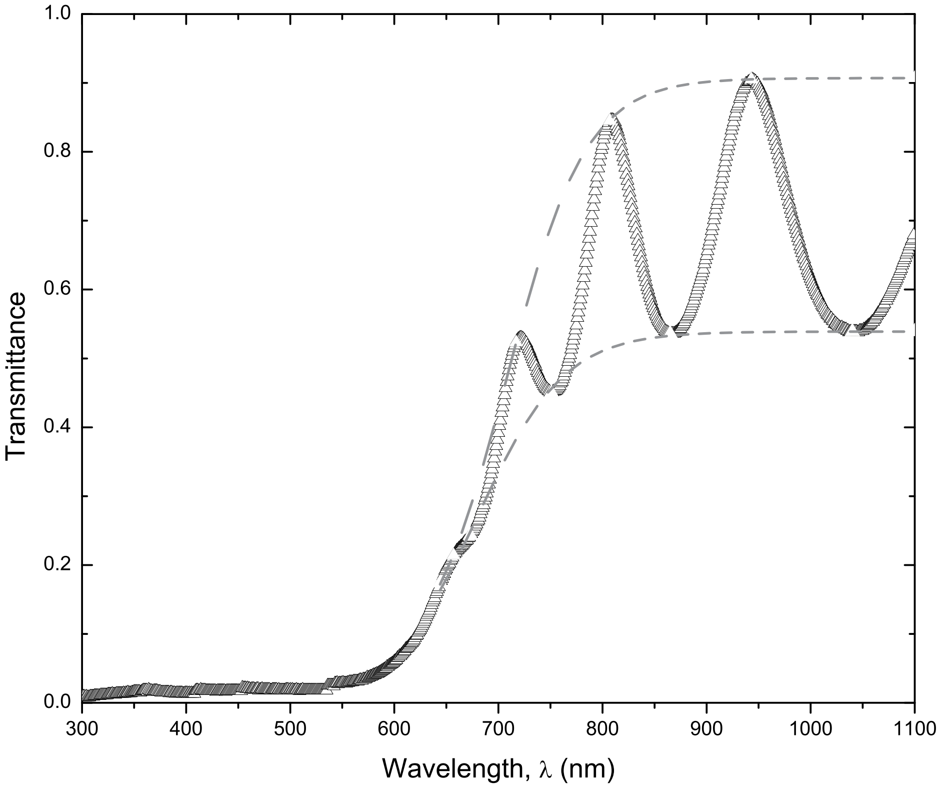

Figure 4.13: A typical optical transmission spectrum for as-grown AIS thin films with the constructed envelope curves.

where T_s is transmittance value of the transmission spectrum for the glass substrate alone. The obtained refractive index values for the thin films from the Eqn. 4.2 were plotted as a function of wavelength in the weak absorption and transparent region between 750 and 1100 nm in the Fig. 4.14(a). Obviously, the index of refraction n varies from 4.00 to 4.40 over the wavelength region of 750-1100 nm for the as-grown thin films. In order to check the correctness and the applicability of this value for the as-grown AIS thin films, the equation used for the determination of thickness of the films was utilized to find the electromechanically measured thickness value of (0.71 ± 0.01) μm by Dektak 6M profilometer. The thickness, d, of the thin films is given by [113]

$$d = \frac{\lambda_1 \lambda_2}{2\left(\lambda_1 n_2 - \lambda_2 n_1\right)} \tag{4.5}$$

where n_1 and n_2 are the refractive indices of two adjacent transmittance maxima or minima of the interference fringes located at λ_1 and λ_2, respectively. Choosing λ_1 and λ_2 as 807 and 943 nm corresponding to the two adjacent maxima in the transparent region where n is almost constant with the value of 4.22, the Eqn. 4.5 yields the thickness d of (0.69 ± 0.01) μm which is well consistent with the above measured result. Along with this consideration, the calculated refractive indices of the thin films can be adopted as correct. On the other hand, after annealing AIS thin films at 200°C, the refractive index of the films drops to the 3.60-3.80 interval over the same wavelength range. This change in refractive index can be ascribed to the amorphous-to-polycrystalline phase transformation occurs in the AIS thin film structure after annealing at 200°C. When the annealing temperature was increased to 300°C, n values increase again to the values in between 4.20 and 4.80. This change in n values is related to the change in the dominant structural phase within the AIS thin films after annealing the multiphase polycrystalline AIS thin films at 300°C just following to the annealing at 200°C [110] as discussed in Section 4.2. However, n values of the films annealed at 400°C could not be evaluated due to the insufficient number of interference fringes observed in optical transmission spectrum [119].

In the CWT method, the wavelet transform of the transmittance signal $\mathrm{T}(\mathrm{k}_0)$, $k_0 = 2\pi/\lambda$ being the wave number, is expressed as [115]

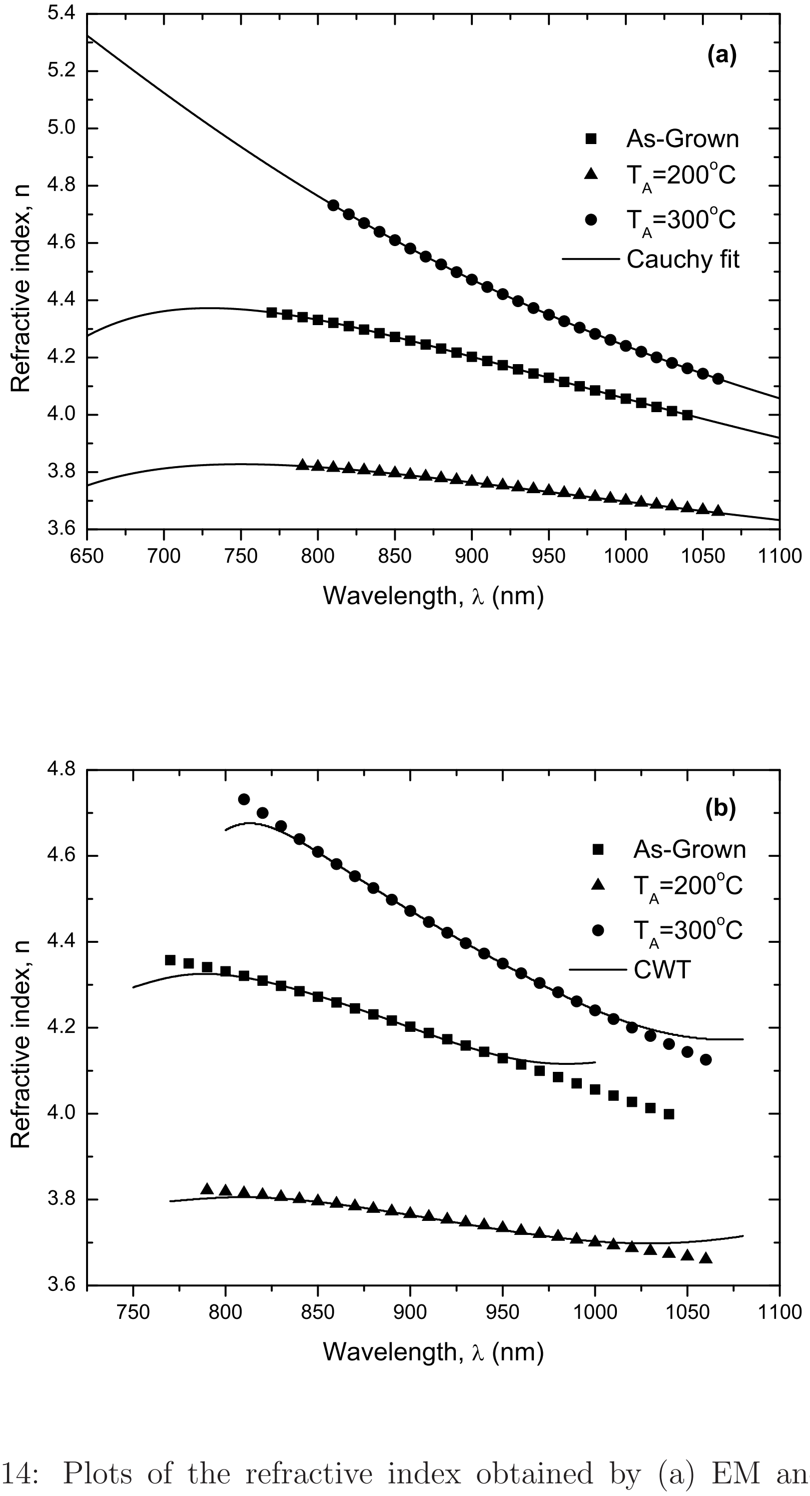

Figure 4.14: Plots of the refractive index obtained by (a) EM and fitted by Cauchy dispersion equation (solid line) and (b) CWT method (solid line) vs. incident photon energy for as-grown and annealed AIS thin films.

$$W(a,b) = \frac{1}{\sqrt{a}} \int_{-\infty}^{\infty} h^* \left(\frac{k_0 - b}{a} \right) T(k_0) dk_0 \tag{4.6}$$

Each wavelet is obtained by scaling a mother wavelet $h(k_0)$ by $a > 0$ and translating it by b. In this study, the Morlet wavelet was used to deal with transmittance signal because it is known to provide a better localization than any other wavelet. The Morlet wavelet, which is a plane wave modulated by a Gaussian, is defined as

$$h(k_0) = \pi^{1/4} exp(ick_0) exp(-k_0^2/2) \tag{4.7}$$

where $c = \pi(2/ln2)^{1/2}$. For a fixed b, the modulus $|W(a,b)|$ has a ridge at

$$a_{max}(b) = \frac{c + \sqrt{c^2 + 2}}{4dn} \tag{4.8}$$

which leads to the calculation of corresponding refractive index provided that the film thickness is known. The obtained refractive index dispersion of the films from CWT analysis was plotted in Fig. 4.14b.

4.3.2 Dispersion Relations of Refractive Indices for Ag-In-Se Thin Films

The values of n calculated by EM and CWT methods can be fitted by

$$n(\lambda) = A_n + \frac{B_n}{\lambda^2} + \frac{C_n}{\lambda^4} + ... \tag{4.9}$$

which is called as Cauchy dispersion relation [120]. The least square fit of the n values by Cauchy equation can be used for the extrapolation of the values to whole wavelengths. The values of the calculated fitting parameters A_n, B_n and C_n for each annealing temperature are listed in Table 4.7.

The imaginary part of the complex refractive index $\tilde{N}$, which is the extinction coefficient k, can be deduced from the absorption coefficient, (α), given as [121]

$$\alpha = \frac{4\pi}{\lambda} k \tag{4.10}$$

Table 4.7: The calculated values of refractive index by both EM and CWT methods, extinction coefficient, real and imaginary parts of dielectric constant at 850 nm for the AIS thin films. Cauchy fitting parameters for the dispersion spectra of n for as-grown and annealed AIS thin films. The n, k, ϵ_{re}, ϵ_{im} values were calculated within an accuracy of 2% due to the systematic measurement error of the spectrophotometer

$T_A(^oC)$	n(EM)	n(CWT)	k	ϵ_{re}	ϵ_{im}	A_n	B_n x 10^6 (nm^2)	C_n x 10^{11} (nm^4)
As-Grown	4.27	4.27	0.06	18.25	0.52	2.928	1.537	- 4.089
200	3.79	3.79	0.02	14.41	0.18	3.147	0.7657	- 2.153
300	4.61	4.60	0.03	21.25	0.28	3.043	1.369	- 1.711

where α is defined as;

$$\alpha = -\frac{1}{d} ln \left(\frac{1}{T} \right) \tag{4.11}$$

here T is the normalized transmittance and d thickness of the thin films. The calculated values of k decrease monotonically from 0.12 to 0.02 as the wavelength increases in between 650 and 1100 nm.

The real and the imaginary parts of the refractive index n and k determined from the transmission measurements are strongly related to the complex dielectric function [121];

$$\varepsilon^{*}(\lambda) = \varepsilon_{re}(\lambda) + i\varepsilon_{im}(\lambda) \tag{4.12}$$

by the relation

$$\tilde{N}(\lambda) = n(\lambda) + ik(\lambda) = [\varepsilon^{*}(\lambda)]^{1/2}. \tag{4.13}$$

Then, the real and imaginary parts of the complex dielectric function can be written through the mathematical expressions

$$\varepsilon_{re}(\lambda) = n^{2}(\lambda) - k^{2}(\lambda) \tag{4.14}$$

$$\varepsilon_{im}(\lambda) = 2n(\lambda)k(\lambda) \tag{4.15}$$

The resulting ε_{re} spectrum of multi-phase AIS thin films, both as-grown and annealed at different temperatures, is shown in Fig. 4.15. Since $k << n$ for the AIS thin films, the variations of ε_{re} and ε_{im} values over the wavelength region of 750-1100 nm are similar to those of n and k, respectively. The reasonably high values of ε_{re} can be the consequence of a multi-phase polycrystalline structure of AIS thin films [110] as discussed in Section 4.2. The calculated ε_{im} values were found to vary between 0.1 and 0.6 over the studied wavelength range.

The dispersion of the refractive index n can also be analyzed through single oscillator model (SOM) proposed by Wemple and DiDomenico [122] in order to

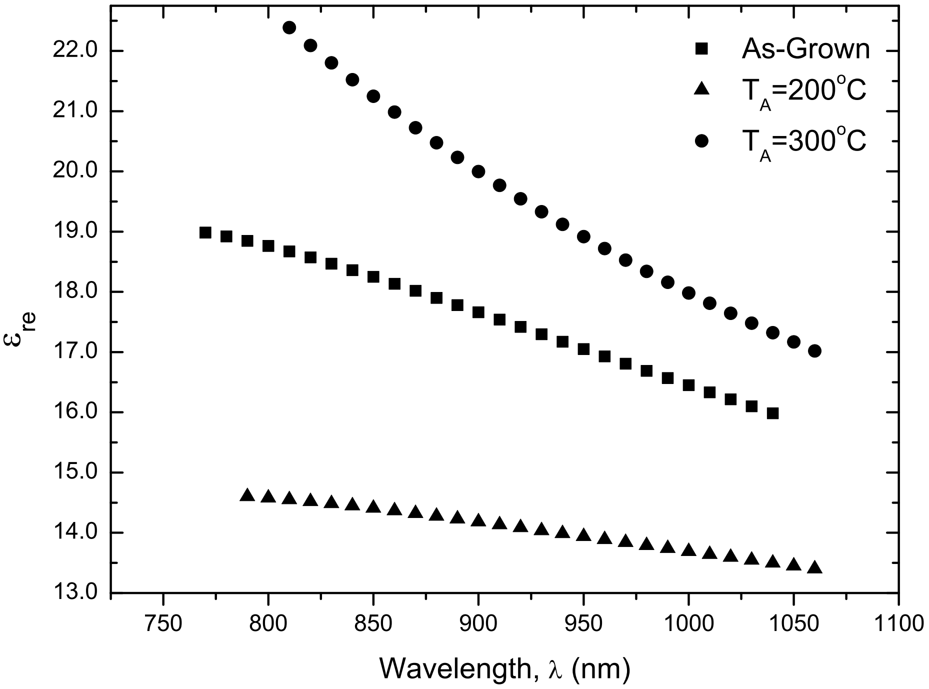

Figure 4.15: Dispersion spectra of the real part of the complex dielectric function for the as-grown and annealed AIS thin films at different annealing temperatures.

study electronic band structure dependent dispersion and oscillator energy, E_d and E_p using the following mathematical equation

$$n^2(h\nu) = 1 + \frac{E_p E_d}{E_p^2 - (h\nu)^2}. \tag{4.16}$$

The SOM assumes that the imaginary part of the dielectric constant ε_{im} is a delta function at energy E_p. By taking the very small k values calculated for AIS thin films into consideration, it can be written as $\varepsilon_{re}(\lambda) = n^2(\lambda)$ and this model can be accepted as applicable to the dispersion of n values of the films. Single oscillator parameters E_d and E_p were determined from the linear plots of $(n^2 - 1)^{-1}$ vs. $(h\nu)^2$ as shown in Fig. 4.16 and the values are listed in Table 4.8. By extrapolating the linear variations to $h\nu = 0$, the static refractive index $n(0)$ and static dielectric constant $\varepsilon(0)$ can be obtained (Table 4.8). It is seen from Fig. 4.16, as expected, SOM gives very reasonable fits for the incident photon energies well below the 1.5 eV which is about the lowest optical bandgap as discussed below.

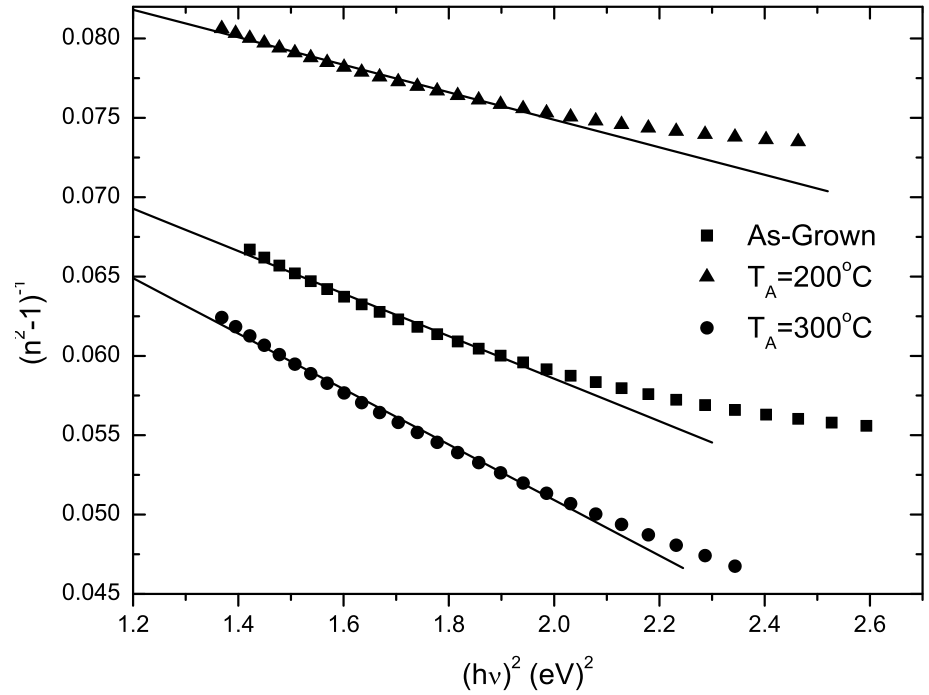

Figure 4.16: Plots of $(n^2 - 1)^{-1}$ vs. $(h\nu)^2$ for as-grown and annealed AIS thin films at 200 and 300°C.

However, at higher energy values, a deviation from the linear behavior is observed (Fig. 4.16) due to the excitonic absorption or energy correspondance to the band edge [121]. Since the value of E_d is the indication of the strength of the transition, the strongest optical transition ability is obtained from the AIS thin films annealed at 200°C (Table 4.8). In other words, the optical properties of AIS thin films strongly depend on the structural formations within the films.

Table 4.8: Physical parameters obtained by single oscillator model for as-grown and annealed AIS thin films at different temperatures

$T_A(^oC)$	$n(0)$	$\varepsilon(0)$	$E_d(eV)$	$E_p(eV)$
As-Grown	3.57	12.75	29.58	2.52
200	3.44	11.83	35.36	3.26
300	3.55	12.60	25.81	2.21

4.3.3 Fundamental Optical Absorption in Ag-In-Se Thin Films

In the variation of the optical absorption coefficients calculated by using Eqn. 4.17 and as seen from Fig. 4.17a, there are basically three different regions for the absorption coefficients due to the distinct physical nature of the optical absorption at these regions [121]; i) high absorption region, where the magnitude of optical absorption coefficient $\alpha > 10^4$ cm^{-1}. In this energy region, high absorption coefficients are recorded and the optical absorption takes place between the extended valence and conduction band states. Then, the absorption coefficient can be described by the relation

$$\alpha h\nu = C_\alpha (h\nu - E_g)^\gamma. \tag{4.17}$$

The exponent γ takes the values of 1/2 (allowed direct transition), 2 (allowed indirect transition), 3/2 (forbidden direct transition) and 3 (forbidden indirect transition). C_α is a constant related to the tailing states at the band edge and E_g is the optical band gap which is one of the most important physical parameters of the thin film semiconductors. ii) the spectral absorption region at lower energy defined as $10^2 < \alpha < 10^4$ cm^{-1}. The region is called as Urbach's region (or Urbach tail) and corresponds to the absorption involving the band tail states. In the Urbach's region, α is defined as;

$$\alpha = \alpha_o exp[(h\nu - E_g)/E_e]. \tag{4.18}$$

E_e is the energy width of tail states and can be adopted as a degree of disorder in the thin film structure. In Fig. 4.17(a), the region between the dotted lines corresponds to the Urbach region. iii) Low energy absorption region in which $\alpha < 10^2$ cm^{-1} and the optical transitions carry out among localized states.

As shown in Fig. 4.17(b), the slopes of the linear fittings to the variations of Ln (α) vs. ($h\nu$) are used to evaluate the E_e values as listed in Table 4.9. The calculated energy width values are in good agreement with those obtained from temperature dependent conductivity analysis of AIS thin films [123] discussed in Section 4.4. The energy width of the band tail states related with the structural defects and impurities decreases in magnitude as the AIS thin films are annealed at 200°C [124]. It is a consistent result as compared to those obtained in the structural analysis. According to the XRD analysis performed on AIS thin films, as-grown thin films are amorphous in nature and annealing them at 200°C transforms AIS thin films into polycrystalline phase [110]. This means that some of the structural defects arising from uncomplete bonding and growth process are removed and a decrease in the density of localized states in the bandgap takes place along with the observed decrease in the band tail width. However, further annealing the AIS thin films at 300 and 400°C increases the width of the band tail states near the valence-band edge as seen in Table 4.9. It is not a contradiction because as it was observed from XRD and XPS analysis for the AIS thin films that annealing the AIS thin films at and above 300°C triggers the segregation mechanism of Se atoms, in which Se atoms leave their original sites producing Se vacancies, in turn causes the some of the grains to dissolve while other new grains and grain boundaries to form, therefore increases the density of localized energy states near the valence-band edge [86, 110].

Fig. 4.17(a) shows the arrhenius plot of the absorption coefficient on the incident photon energy. There are three distinct local maxima for absorption coefficients in the high absorption region where optical absorption process occurs between the extended valence and conduction band. In other words, there are three different intrinsic band-to-band transitions for AIS thin films. This phenomena can be explained by the splitting of the valence band into three bands due to hybridization of d-like valence band states and p-like conduction

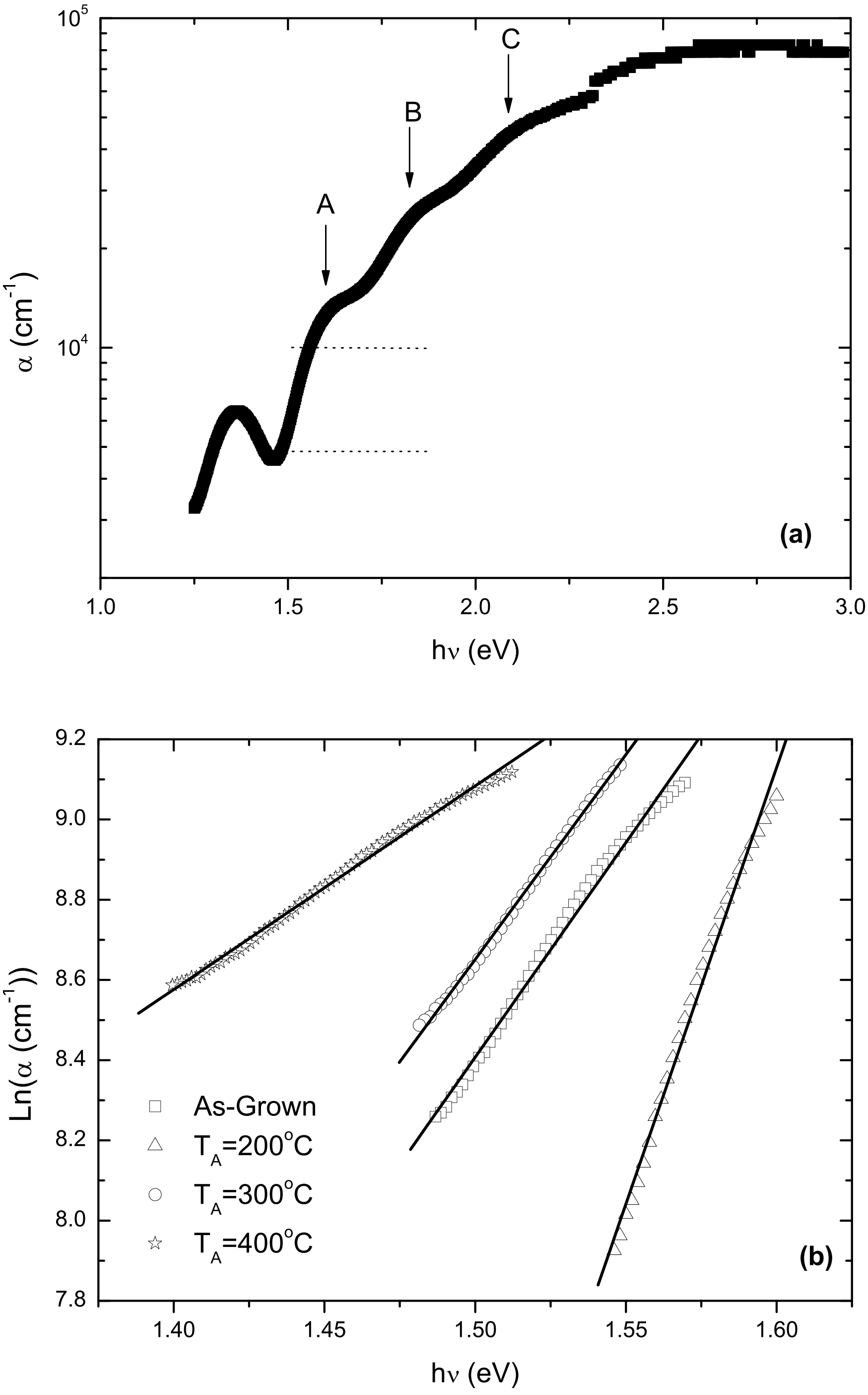

Figure 4.17: (a) The semi-logarithmic plot of the absorption coefficient on the incident photon energy for the a typical AIS thin film. The dotted lines represents the borders for Urbach region. The designated points A, B and C show absorption shoulders (local maxima) in the high absorption region. (b) The variation of $Ln(\alpha)$ vs. $(h\nu)$ for the as-grown and annealed AIS thin films.

band states [6,125]. The uppermost and lowermost valence bands are separated from mid-valence band by the amount of Δ_{CF} (Crystal Field Splitting) and Δ_{SO} (Spin-Orbit Splitting), respectively [6–8]. The same results were also observed from the spectral dependence of photocurrent measurements in Section 4.5.2.

As shown in Fig. 4.18, the $(\alpha h\nu)^2$ vs. $(h\nu)$ plots with $\gamma = 1/2$ have very good linearity in the extended energy region. Therefore, the fundamental optical transitions in multi-phase AIS thin films are determined to be direct transitions in nature. From the linear fittings applied to the variations in Fig. 4.18, the optical energy band gaps of three optical transitions determined from Fig. 4.17(a) were calculated according to the Eqn. 4.17 and listed in Table 4.9. The optical band gaps correspond to the energy differences from the top of uppermost valence band to the bottom of the conduction band (E_{g1}). The E_{g1} energies for as-grown and annealed AIS thin films at 200°C are 1.72 and 1.71 eV, and 1.57 and 1.68 eV, which were obtained from optical transmission and spectral photoresponse analysis, respectively [123] as discussed in Section 4.5.2. The difference between the band gap energies are comparable with the calculated energy widths of the tail states near the valence band edge (Table 4.9). Therefore, the observed deviations in the band gap values are reasonable in terms of two different optical measurements. As the annealing temperature increases, the optical energy band gap value for the AIS thin films decreases due to the increase in the energy widths of the band tail states as shown in Table 4.9 [67,126]. The XRD and XPS results also support that the crystallinity and grain sizes of the thin films were not improved significantly. If there were an improvement in crystallinity of the films, which resulted in increases in grain sizes, it allows the density of localized energy states to decrease and the optical energy band gaps to increase [124].

The other two calculated energy band gaps, E_{g2} and E_{g3} as seen from Fig. 4.18, correspond to direct valence-to-conduction band transitions (B and C in Fig. 4.17), which are caused by the crystal-field slitting of the valence band induced by the tetragonal chalcopyrite structure and the spin-orbit splitting of the valence band, respectively [6,21]. Therefore, the A, B and C transitions seen in Fig. 4.17 are identified as the allowed direct transitions to a single conduction

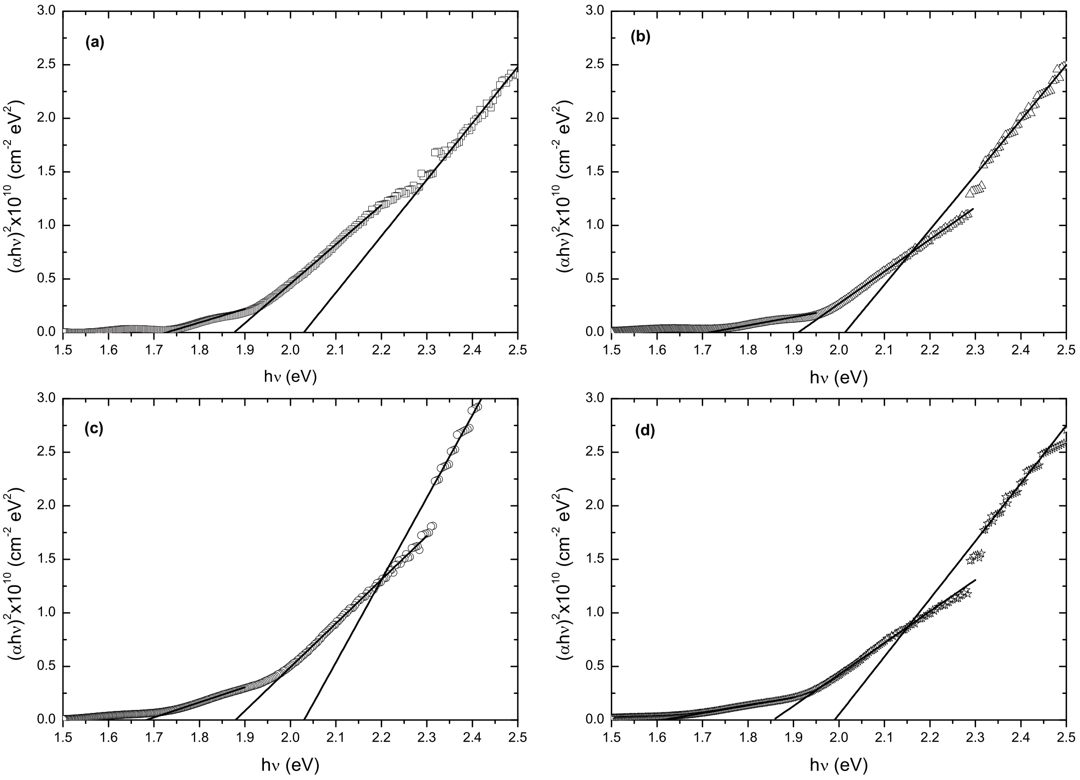

Figure 4.18: The variation of $(\alpha h\nu)^2$ as a function of incident photon energy for (a) as-grown, (b) 200°C-annealed, (c) 300°C-annealed and (d) 400°C-annealed AIS thin films.

band from three closely separated valence bands. The quasicubic model, which explains correctly the splitting of p-like levels in the valence band combining the effects of a tetragonal crystalline field and spin-orbit interaction, defines the energy levels of the splitted valence bands peculiar to the A and C optical transitions relative to the energy level in the valence band of a chalcopyrite semiconductor structure corresponding to the B transition as [6, 7, 125];

$$E_{1,2} = -\frac{1}{2}(\Delta_{SO} + \Delta_{CF}) \pm \frac{1}{2}[(\Delta_{SO} + \Delta_{CF})^2 - \frac{8}{3}\Delta_{SO}\Delta_{CF}]^{1/2} \qquad (4.19)$$

where Δ_{SO} is the spin-orbit splitting and Δ_{CF} is the crystal-field splitting of the valence bands for AIS thin films. The $E_{1,2}$ energies are defined as the energy differences of $E_1 = E_{g2} - E_{g1}$ and $E_2 = E_{g2} - E_{g3}$. The calculated parameters of the quasicubic model, Δ_{SO} and Δ_{CF} are in good agreement with the results

Table 4.9: Band tail energy width values and the quasicubic model parameters related with the valence band splitting for the as-grown and annealed AIS thin films. The E_{g1}, E_{g2} and E_{g3} values were calculated within an accuracy of 0.03 eV due to inaccuracy in thickness of the films and systematic measurement error

$T_A(^oC)$	$E_e(eV)$	$E_{g1}(eV)$	$E_{g2}(eV)$	$E_{g3}(eV)$	$-\Delta_{CF}(eV)$	$\Delta_{SO}(eV)$
As-Grown	0.083	1.72	1.87	2.03	0.18	0.19
200	0.046	1.71	1.91	2.01	0.23	0.13
300	0.098	1.68	1.88	2.03	0.24	0.18
400	0.197	1.61	1.86	1.99	0.29	0.17

obtained from the spectral photocurrent analysis [123] in Section 4.5.2 and listed in Table 4.9 for as-grown and annealed AIS thin films.

4.4 Electrical Characterization of Ag-In-Se Thin Films

In this section, the results of the electrical conductivity measurements, which were carried out as a function of ambient temperature, of e-beam evaporated Ag-In-Se thin films in both as-grown and annealed forms at different temperatures will be presented and the nature of the electrical transport in those films will be discussed within the corresponding theoretical frameworks.

The electrical transport properties of the e-beam evaporated AIS thin films were investigated by means of temperature dependent conductivity measurements in the temperature range changing from 100 to 450 K as well as by taking the effect of post annealing into account and the measurements were carried out simultaneously on the same sample by the four probe technique of van der Pauw to eliminate finite contact effects. The hot-probe technique showed that all of the films have n-type electrical conductivity. As a result of temperature dependent conductivity measurements, the room temperature conductivity values obtained for the AIS thin films depending on the annealing temperature lie in the range between 1.9×10^{-6} and 5.2 $(\Omega\ \mathrm{cm})^{-1}$ as listed in Table 4.10. Apparently, the electrical conductivity of the thin films increases systematically with the increasing annealing temperature.

4.4.1 Temperature Dependent Dark Conductivity Measurements

In order to obtain the general behavior of conductivity against the changes in ambient temperature in the films, the temperature dependent conductivity measurements were carried out. As seen from Fig. 4.19, the variation of the conductivity values as a function of temperature shows an increasing exponential behavior with increasing absolute temperature for the as-grown and 200°C-annealed AIS thin films.

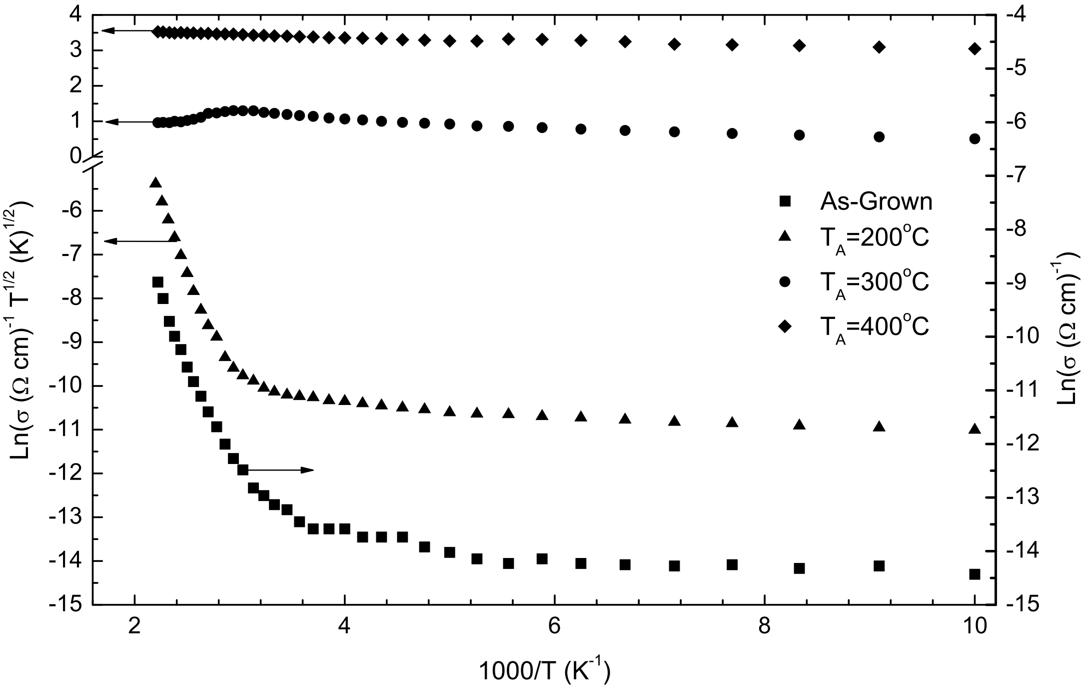

Figure 4.19: The variation of conductivity as a function of the inverse absolute temperature for the AIS thin films at different annealing temperatures.

After annealing the samples at 300°C, the semiconductor properties of the films are transformed into a degenerate form along with the increase in conductivity values because of segregation and/or re-evaporation of Se atoms in the structure due to the high vapor pressure and annealing at 400°C confirms the presence of this form in the film structure, whereas a significant increase in conductivity values is observed at each constant temperature as compared with the values as a function of annealing temperature. The most plausible reason for that type of electrical behavior is the realization of the segregation of Se atoms, as a result of which a Se-deficient and In-rich thin film surfaces were produced as discussed in XPS and XRD analysis [86, 110]. The structure of the thin films that were annealed at 200°C is dominated by In_4Se_3, InSe and Se compounds as far as the intensities of characteristic XRD peaks are concerned. Furthermore, annealing at 300°C changes this structural existence significantly and the film structure is composed mainly of $Ag_3In_5Se_9$, $AgInSe_2$, In_2Se_3 and InSe crystalline phases [110]. As far as the conductive properties of the films are concerned, it can be inferred that the optimum temperature of post thermal annealing process for AIS thin films is 200°C in order to maintain the semiconductor characteristics.

Table 4.10: The room temperature conductivity values and the calculated activation energies E_a of the AIS thin films

Annealing Temperature	Conductivity σ $(\Omega\ \text{cm})^{-1}$	Activation Energy E_a (meV)		
T_A (°C)	(at 300 K)	310-450 K	210-300 K	100-200 K
As-Grown^a	1.9×10^{-6}	388	65	9
200^b	2.3×10^{-6}	423	43	7
300^b	9.8×10^{-1}	-	17	6
400^b	5.2	7	7	5

The activation energy values were calculated by using ^{a} Eqn.4.20 and ^{b} Eqn.4.30 .

4.4.1.1 Electrical Transport Properties of As-grown AIS Thin Films

The variation of electrical conductivity values of as-grown thin films with respect to temperature exhibits an increasing exponential behavior as the absolute temperature increases specifically after the critical temperature of 300 K as it is seen from Fig. 4.19. On the contrary, below this critical ambient temperature, the experimentally measured conductivity values are almost insensitive to change in temperature for the as-grown thin films. Furthermore, the as-grown thin films have very close conductivity values having almost the same temperature dependence with 200°C-annealed sample, however, they are amorphous in nature as observed from XRD analysis. Then, the conductivity vs. temperature variation of the as-grown amorphous films are analyzed according to conductivity expression due to the excitation of the carriers into the extended states beyond the mobility shoulders [67,127];

$$\sigma = \sigma_o exp\left(-\frac{E_a}{kT}\right). \tag{4.20}$$

where σ_o is the preexponential factor, E_a is the activation energy, k is the Boltzmann constant, and T is the absolute temperature. As seen from Fig. 4.19 and Table 4.10, the Ln(σ)-1000/T variation is linear above 300 K with a calculated activation energy of 388 meV. Below this temperature level the Ln(σ)-1000/T variation differs from this trend as proved by the calculated temperature-dependent activation energy values that decrease with decreasing temperature. This experimental observation rules out the validity of the same kind of transport mechanism in the amorphous thin films. In other words, the calculation of different activation energy values for different temperature regions by means of the Eqn. 4.20 implies the existence of distinct conduction mechanisms dominating the charge transport in the as-grown thin films. Therefore, the temperature dependence of the electrical conductivity of as-grown thin films can be investigated at three different temperature zones with respect to the dominant conduction mechanism as follows;

- ***high temperature region***; as it is seen from Fig. 4.20(a) the plot of Ln(σ) vs. 1000/T for as-grown thin films gives a linear variation in the temperature region starting from 300 up to 450 K which indicates that the current conduction in the amorphous as-grown thin films is dominated by the electrons in the extended states above E_C with the thermal activation

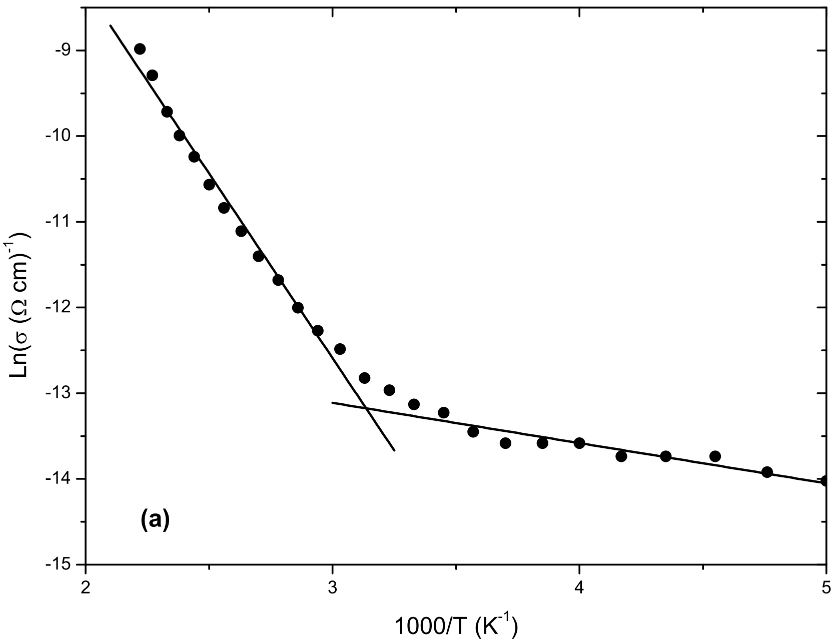

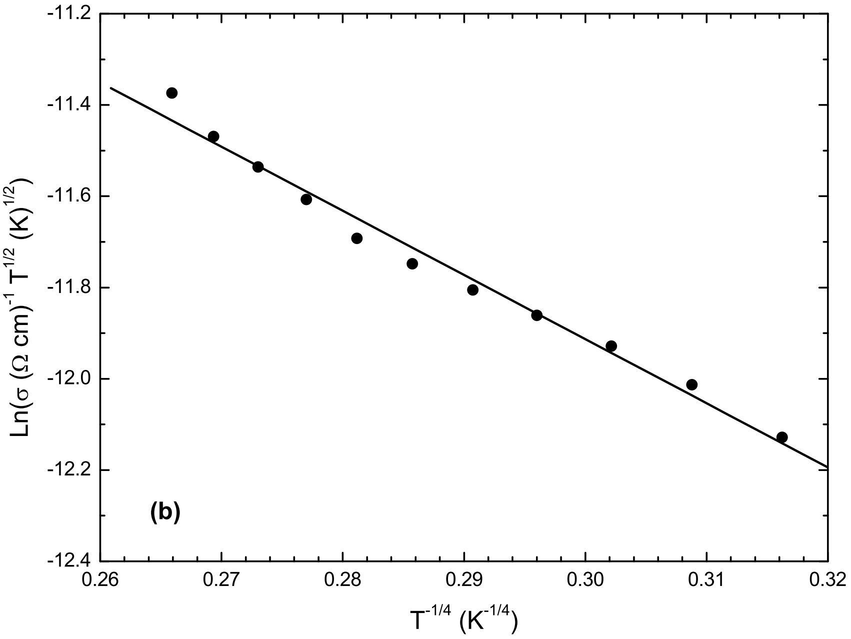

Figure 4.20: Linearly fitted parts of (a) the plot of Ln(σ) vs. 1000/T variation and (b) the plot of Ln($\sigma T^{1/2}$) vs. T$^{-1/4}$ variation for the as-grown AIS thin films.

energy equal to $(E_C - E_F)$. Therefore, at the high temperature region the temperature dependence of conductivity for as-grown AIS thin films is expressed as in Eqn. 4.20 and related parameters that is calculated through experimental data is given in Table 4.11.

- ***moderate temperature region***; the boundaries of this temperature range is determined to be in between 200 and 300 K by analyzing the second distinct linear variation in the Ln(σ)- 1000/T plot as seen in Fig. 4.20(a). At these moderate temperatures the electrons in the extended conduction band can not have enough thermal energy to contribute the electrical conduction as in the case of high temperature conductivity. However, the current conduction is mainly characterized by the the electrons occupying the band tail states with energies less than E_C by means of phonon-assisted hopping among neighbor electronic sites. In this case, the variation of conductivity as a function of temperature at the moderate temperature region is given by

  $$\sigma = \sigma_T exp\left(-\frac{E_a}{kT}\right) \tag{4.21}$$

  where σ_T is the preexponential factor, which is smaller than σ_o in Eqn. 4.20, and E_a is defined this time as the difference between the average energy of the band tail states E_T and the Fermi level. The related parameters in Eqn. 4.21 are calculated and tabulated in Table 4.10 and 4.11.

- ***low temperature region***; at very low temperatures changing from 100 to 200 K, the conductivity values remain almost constant with changing temperature as seen from Fig. 4.19. The finite conductivity values imply that the charge transport in the films is somehow maintained by means of a different mechanism than the others at these low temperatures. This conduction mechanism was theoretically formalized by Mott and Davis [67] and thus it is named as the Mott's variable range hopping (VRH) conduction, which is discussed in detail in section 2.5.1.3. The arguments of Mott's theoretical framework depend on the concept that at such low temperatures, the charge carriers can be transported most efficiently among the localized states randomly distributed in energy around the Fermi level because of the strong possibility that the empty and occupied states with close energies can be found near the Fermi level. Therefore, Mott's variable range hopping mechanism predicts the behavior of electrical conductivity at low temperatures by obeying the equation

$$\sigma\sqrt{T} = \sigma_H exp\left(-\frac{T_o}{T}\right)^{1/4} \tag{4.22}$$

where σ_H is the corresponding pre-exponential factor defined as

$$\sigma_H = \left(\frac{A^2 N(E_F)}{\gamma}\right)^{1/2} \tag{4.23}$$

where A is expressed as

$$A = \frac{3e^2\nu_{ph}}{(8\pi k)^{1/2}} \tag{4.24}$$

and γ is the localization radius for the wavefunctions of the localized states around the Fermi level and given by

$$\gamma = \frac{\sigma_H (kT_o)^{1/2}}{4A} \tag{4.25}$$

and T_o is the characteristic temperature which is given by

$$T_o = \frac{16\gamma^3}{kN(E_F)} \tag{4.26}$$

and the density of localized states around E_F, $N(E_F)$, is expressed by

$$N(E_F) = \frac{\sigma_H^3 (kT_o)^{1/2}}{4A^3} \tag{4.27}$$

and the typical hopping distance, R, is defined as

$$R = \left(\frac{9}{8\pi\gamma kTN(E_F)} \right)^{1/4} \tag{4.28}$$

and finally the average hopping energy, W, is mathematically expressed by

$$W = \frac{3}{4\pi R^3 N(E_F)} \tag{4.29}$$

which are all called as the Mott's parameters and the ratio (T_o/T) gives the approximate measure of the degree of disorder in the thin film structure. In all above equations, k refers to the Boltzmann constant and ν_{ph} is the phonon frequency whose value is taken to be around $10^{12}\ s^{-1}$. Fig. 4.20(b) shows the linear variation in the low temperature region for the Ln$(\sigma T^{1/2})$ vs. T$^{-1/4}$ plot that indicates the domination of the Mott's variable range hopping mechanism over the others in current conduction for as-grown AIS thin films. The Mott's parameters are calculated through the fitting parameters of the linear fit in Fig. 4.20(b) and the above-given related equations and the calculated parameters are tabulated in Table 4.12. Additionally, the validity of the Mott's theoretical work for the case of as-grown AIS thin films was checked by the requirements that $\gamma R > 1$, which is related to the degree of localization, $W > kT$, $T_o > 10^3$ and $T_o/T > 43$. Therefore, the calculated parameters are decided to be physically meaningful for our case.

Table 4.11: The calculated values of the pre-exponential factors in the conductivity relations at different temperature regions given in Eqn. 4.20, Eqn. 4.21, Eqn. 4.30, Eqn. 4.31, and Eqn. 4.22, respectively, by using the obtained experimental data for as-grown and annealed AIS thin films at 200°C.

T_A (°C)	σ_o $(\Omega\,\text{cm})^{-1}$	σ_T $(\Omega\,\text{cm})^{-1}$	σ_{th} $(\Omega\,\text{cm})^{-1}\text{K}^{1/2}$	σ_{tun} $(\Omega\,\text{cm})^{-1}$
As-Grown	1.40	8.26×10^{-6}	–	–
200	–	–	3.65×10^{3}	1.41×10^{-6}

Table 4.12: The Mott's parameters calculated by means of Mott's variable range hopping theory for the as-grown and 200°C-annealed AIS thin films in the temperature range of 100-200 K with an average T of 150 K.

T_A (°C)	σ_H $(\Omega\,\text{cm})^{-1}\text{K}^{1/2}$	T_o (K)	γ (cm^{-1})	$N(E_F)$ $(\text{cm}^{-3}\,\text{eV}^{-1})$	R (cm) (for 150 K)	W (meV) (for 150 K)
As-Grown	4.55×10^{-4}	6.97×10^{5}	1.88×10^{5}	1.77×10^{15}	1.70×10^{-5}	27
200	2.17×10^{-4}	1.26×10^{5}	8.01×10^{4}	7.51×10^{14}	2.61×10^{-5}	18

4.4.1.2 Electrical Transport Properties of AIS Thin Films Annealed at 200°C

As discussed previously [110] in the section of XRD results, the annealed AIS thin films at 200°C have polycrystalline structure. In this manner, the polycrystalline thin films are composed of crystallites (grains) surrounded by grain boundaries (sometimes called as internal surfaces) within which there exists a short range order of atoms for crystalline structure. Accordingly, there exists a reasonably high concentration of active trapping sites causing charge carriers to be captured at the grain boundaries which are the most dominant and the least controllable structural formations inside the polycrystalline thin films [59]. The current conduction mechanism for the polycrystalline thin films are significantly influenced by this built-in grain boundary potentials. Therefore, the dominant current conduction mechanisms in 200°C-annealed films are expected to be different from the amorphous thin film case at different temperature regions, although the variation of conductivity as a function temperature is similar in both types of thin films. Again decided by analyzing Fig. 4.19, the conductivity-temperature data for the polycrystalline AIS thin films, which were annealed at 200°C, are to be investigated in three different temperature regimes in accordance with three distinct temperature dependencies of the measured conductivity values as follows;

- ***high temperature region***; the conductivity-temperature data for the polycrystalline AIS thin films annealed at 200°C was analyzed according to the thermionic emission over the grain boundary potential model proposed by Seto [58] where the expression for conductivity is given by

  $$\sigma\sqrt{T} = \sigma_{th} exp\left(-\frac{E_a}{kT}\right) \tag{4.30}$$

  here σ_{th} is the pre-exponential factor, E_a is the conductivity activation energy, k is the Boltzmann constant and T is the absolute temperature. The conductivity activation energies for three different temperature regions

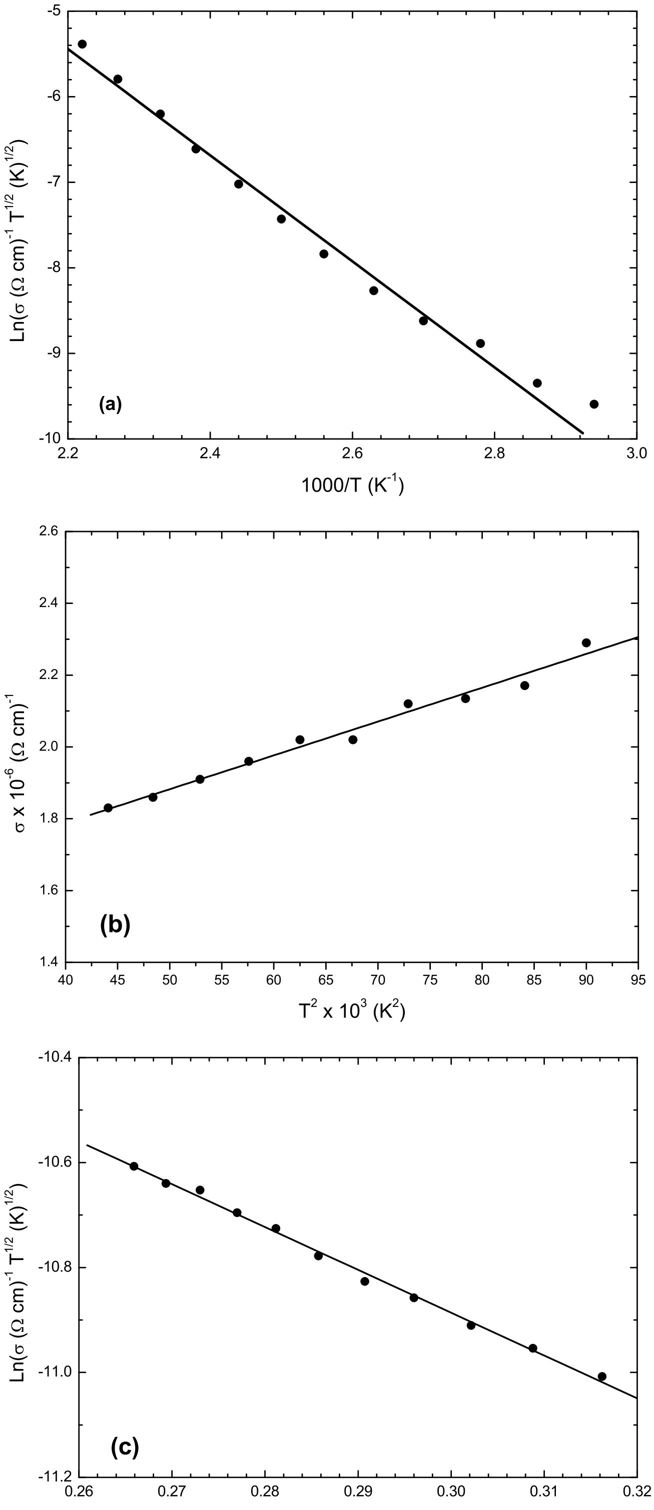

Figure 4.21: Linearly fitted parts of (a) the plot of Ln($\sigma T^{1/2}$) vs. 1000/T variation, (b) the plot of σ vs. T^2 variation, and (c) the plot of Ln($\sigma T^{1/2}$) vs. T$^{-1/4}$ variation in order to reveal the dominant conduction mechanisms at different temperature regions for AIS thin films annealed at 200°C.

are calculated by using Eqn. (4.30) from the variation of Ln($\sigma T^{1/2}$) as a function of inverse absolute temperature for the AIS thin films as in Fig. 4.19 and these values are listed in Table 4.10. As it was observed in the amorphous AIS thin films, the calculated values of different activation energies calculated in different temperature regions confirm the presence of different current conduction mechanism throughout the measurement temperature range.

The linear variation of conductivity with increasing temperature in the plot of Ln($\sigma T^{1/2}$) vs. 1000/T, which is shown in Fig. 4.21(a), proves that the Seto's trapping boundary model developed for the polycrystalline thin films is also the case for the AIS thin films annealed at 200°C. Therefore, it is shown that at high temperature region having the temperature boundary between 300 and 450 K, the physical nature of electrical conductivity in the polycrystalline AIS thin films is dominated by the thermally emitted charge carriers over the grain boundary potential barriers. The calculated parameters for the Eqn. 4.30 are tabulated in Table 4.10 and 4.11.

- ***moderate temperature region***; in this region electrons can not have enough thermal energy to surmount the grain boundary potential barrier, the charge carriers that tunnel quantum mechanically through the high but narrow potential barrier. In accordance with the work of Garcia [61], at moderately high temperatures, the thermally assisted tunneling of charge carriers could be written as,

$$\sigma = \sigma_{tun}\left[1 + \left(\frac{F^2}{6}\right)T^2\right] \tag{4.31}$$

where σ_{tun} is a constant equal to the conductivity at 0 K, and F is another constant that depends on the mean barrier height of the grain boundary potential. Accordingly, the plot of σ vs. T^2 as shown in Fig. 4.21(b) has a linear variation in the temperature range between 200 and 300 K, which is the experimental manifestation of that the dominant contribution to the conduction is from the electrons tunneling the barrier at these temperature values. The related parameters in Eqn. 4.31 are calculated and given in Table 4.11.

- ***low temperature region***; in this region, neither electrons have enough thermal energy to overcome the potential barrier in the grain boundary region, nor the probability for them to tunnel the barrier is high enough to maintain a finite conductivity for AIS thin films. On the other hand, Mott's variable range hopping mechanism could be plausibly well for the 200°C-annealed AIS thin films as well as for the amorphous as-grown AIS films. The variation of $\mathrm{Ln}(\sigma T^{1/2})$ vs. $T^{-1/4}$ plot as seen from Fig. 4.21(c) performs a linear trend between temperatures of 100 and 200 K. Therefore, the Mott's parameters are calculated as tabulated in Table 4.12 and the physical validity of the theory was satisfied by the previously mentioned requirements of $\gamma R > 1$, $W > kT$, $T_o > 10^3$ and $T_o/T > 43$.

Furthermore, in the light of above physical discussions, the significant increase in the activation energy in high temperature region (310-450 K) for the polycrystalline films shows the development of grain boundary potential barrier inside the structure of the films and the apparent improvement in the crystallinity of the grains. In the intermediate temperature region (200-300 K), the activation energies (Table 4.10) are related to the width of the band tail states near conduction band and the decrease in these values with annealing at 200 °C well fits the above statement. This change in the energy width of conduction-band tail states with increasing annealing temperature is in a good agreement with the observed change of the valence-band tail states in optical transmission analysis in Section 4.3.3.

4.5 Photoelectrical Characterization of Ag-In-Se Thin Films

4.5.1 Temperature Dependent Photoconductivity

The temperature dependent photoconductivity measurements for the AIS thin films including both as-deposited and annealed at 200°C were carried out as a function of illumination intensity over the temperature range of 100-450 K under the constant applied electric field strength of 105 V/cm. They were illuminated by a halogen lamp at five distinct incident light intensities of 17, 34, 55, 81 and 113 mW/cm^2 during the photoconductivity measurements.

The highly photoconductive behavior of the AIS thin films is confirmed from the change in the conductivity values by comparing them with the values taken under illumination (see Fig. 4.22). Due to the contribution of the photo-excited carriers to the current conduction, the illuminated conductivity (σ_ϕ) values are higher than those of the dark conductivity (σ_{Dark}) up to a specific temperature where the recombination rate of the carriers suppress the number of free carriers in the conduction band [70]. However, this increase in the conductivity values is relatively less for the 200°C-annealed AIS thin films than as-grown ones. It is obvious that the annealing process at 200°C which was applied to the AIS thin films reduces photosensitivity due to the structural modification and the decrease in the resistivity of the annealed films. The photoconductivity ($\Delta\sigma$) values were calculated by subtracting the (σ_{Dark}) values from the measured (σ_ϕ) values under the illumination ($\Delta\sigma$ = σ_ϕ - σ_{Dark}). Figure 4.23 shows the variation of $\Delta\sigma$ as a function of reciprocal absolute temperature for as-grown and 200°C-annealed AIS thin films at different illumination intensities. As it can be seen from the Fig. 4.23(a) and 4.23(b), the photoconductivity increases exponentially with increasing ambient temperature at each illumination intensity for the as-grown and 200°C-annealed AIS thin films. At low temperature region below 200 K, $\Delta\sigma$ is almost temperature insensitive and directly proportional to the illumination intensity, in other words the $\Delta\sigma$ is directly proportional to the generation rate

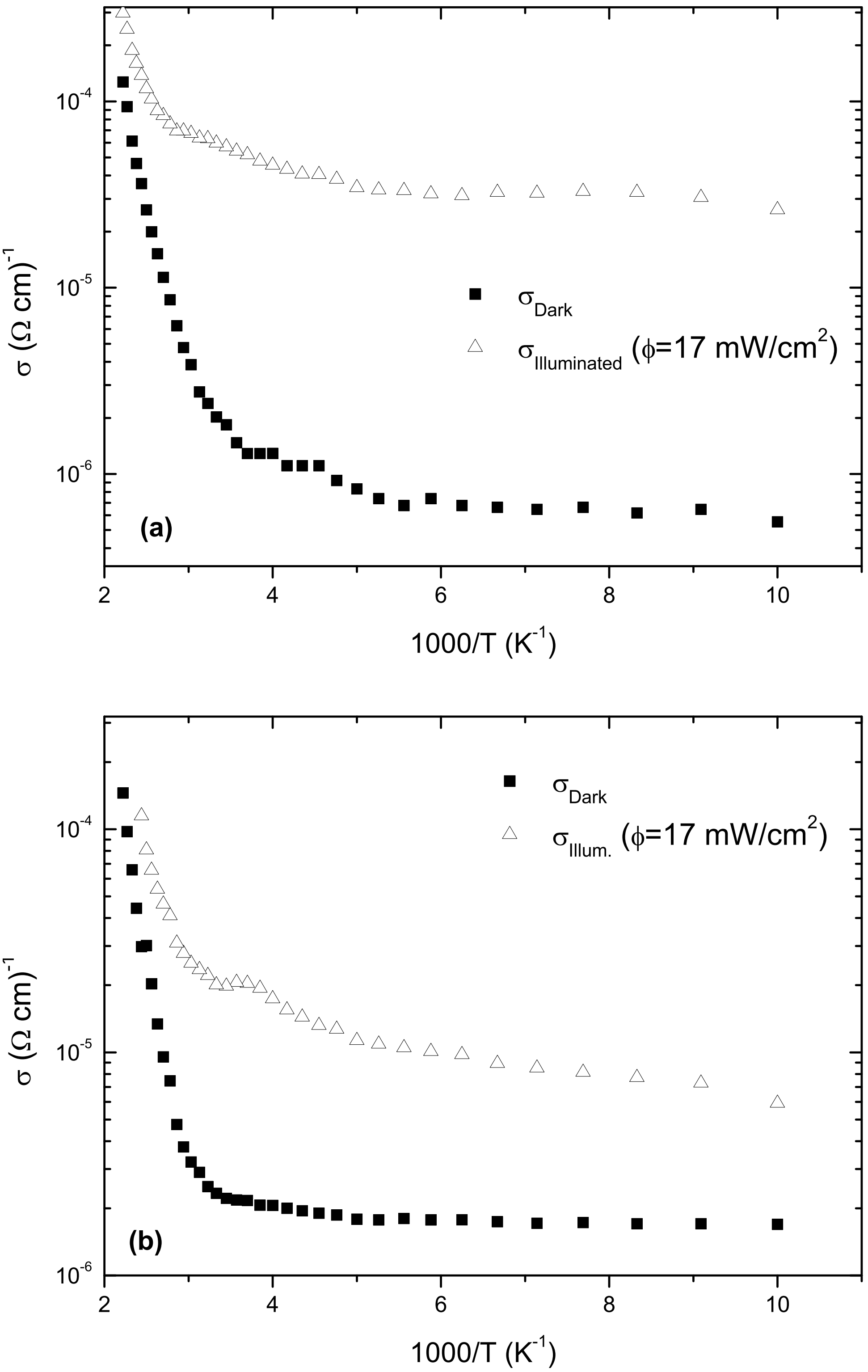

Figure 4.22: The variations of the dark conductivity (σ_{Dark}) and the conductivity under illumination (σ_{ϕ}) as a function of inverse absolute temperature for the AIS thin films in both (a) as-grown and (b) 200°C-annealed forms.

of photo-excited carriers. In the temperature region between 210 and 320 K for as-grown thin films and between 210 and 290 K for the 200°C-annealed ones, photoconductivity slowly varies with increasing temperature and increases again with increasing intensity. The low activation energy values that were calculated and tabulated in Table 4.13 as E_{β_2}, which exhibit almost insensitive behavior against the change in the light intensity, is less than that of σ_{Dark} as predicted by Simmons and Taylor [73]. In the as-grown thin films, for the high temperature region above 330 K, the $\Delta\sigma$ increases rapidly with increasing temperature and light intensity; and attains a maximum value at a critical temperature (T_c). Actually, the (T_c) is the temperature at which σ_{Dark} equals to $\Delta\sigma$ and for T > T_c the concentration of thermal carriers exceeds that of photo-excited carriers and the surface recombination is more dominant, i.e. $\Delta\sigma$ decreases with increasing temperature. This phenomena is known as the thermal quenching of photoconductivity [71]. The observation of T_c was only realized for the $\Delta\sigma$ values as $T_c = 420$ K at the illumination intensity of 17 mW/cm^2 due to the measurement limitations. Therefore, the observation of these regions proves the existence of defect levels and the photo-induced ionization of these energy levels.

The typical dependence of photoconductivity shown in Fig. 4.23(a) and (b) on temperature and illumination intensity shows the distinct temperature regions with the different recombination mechanisms. In other words, monomolecular recombination is dominant at high temperatures together with low intensities of light and the photoconductivity is thermally activated with the activation energy E_α. On the other hand, at moderate temperatures and high incident light intensities bimolecular recombination dominates the conduction. The variation of the photoconductivity as a function of reciprocal temperature with the activation energy E_β is shown in Fig. 4.23(a) and (b). Most of the chalcogenide semiconductors exhibit that type of photoconductivity variation with temperature and light intensity [67, 128] and the discrete trap levels can be obtained in terms of the quantities E_α and E_β by means of the theory presented by Simmons and Taylor for the chalcogenide semiconductors with discrete trap levels within forbidden energy region [72, 73].

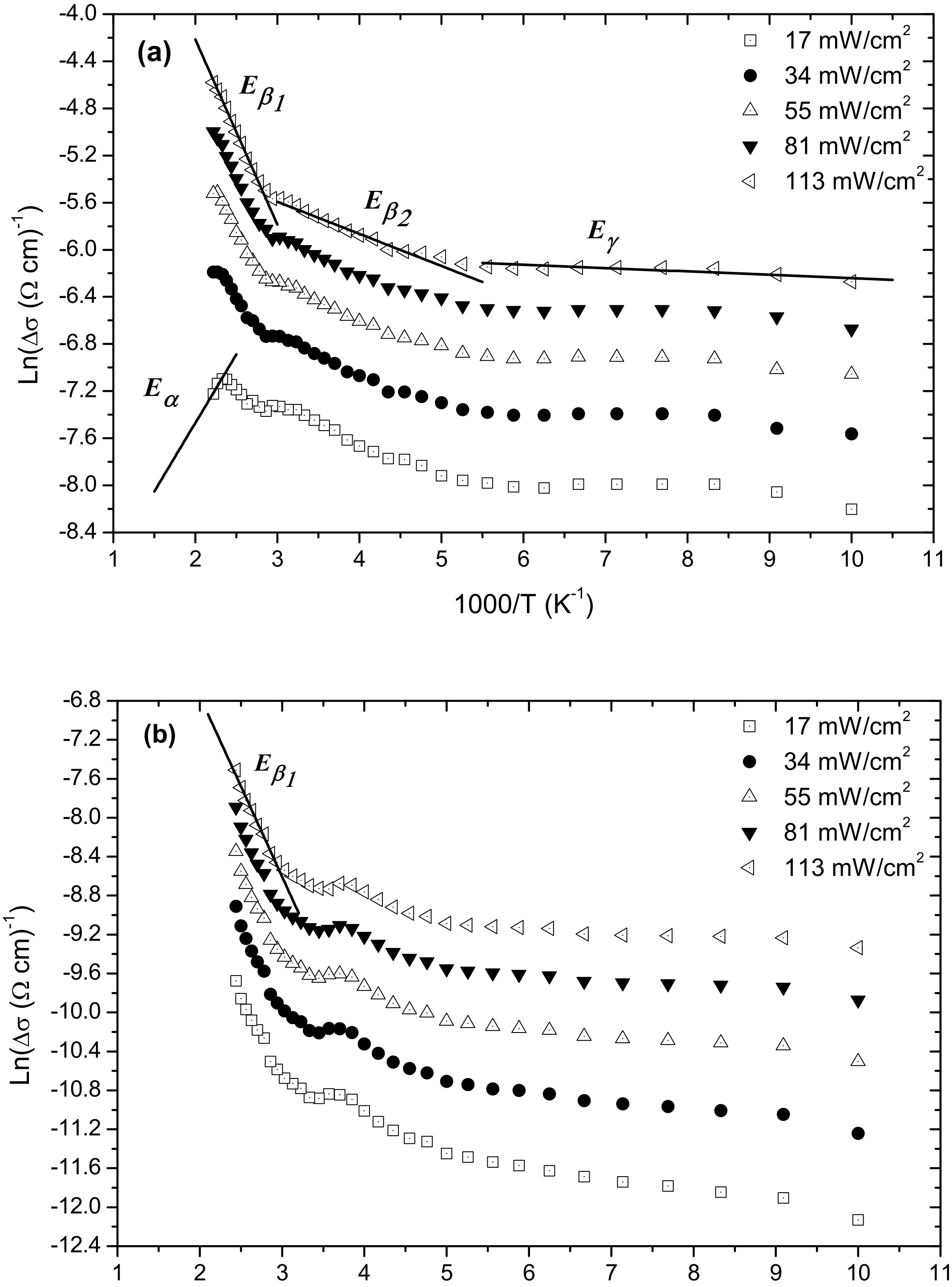

Figure 4.23: The variation of $\Delta\sigma$ for constant applied electric field of 105 V/cm as a function of inverse absolute temperature at different light intensities for (a) as-grown and (b) 200°C-annealed AIS thin films.

Table 4.13: The calculated activation energies from temperature dependent photoconductivity measurements for the as-grown and 200°C-annealed AIS thin films. For all types of thin films there are two distinct activation energies at moderate temperature region calculated under the names of E_{β_1} and E_{β_2}. The activation energies for the last two light intensities are calculated from fitting parameters of Fig. 4.30(a) and (b).

Illumination	As-Grown Films				200°C-Annealed Films			
Intensity ϕ (mW cm^{-2})	E_α (meV)	E_{β_1} (meV)	E_{β_2} (meV)	E_γ (meV)	E_α (meV)	E_{β_1} (meV)	E_{β_2} (meV)	E_γ (meV)
17	101	51	26	3	-	122	32	10
34	-	89	22	4	-	130	28	8
55	-	111	21	3	-	131	25	6
81	-	116	20	3	-	141	23	5
113	-	131	21	3	-	149	22	3
3.6×10^{-5}	103	68	-	3	-	-	-	-
3.5×10^{-5}	-	-	-	-	230 (12)	69	-	8

Table 4.14: The photosensitivity values for AIS thin films under the light flux of 113 mW cm^{-2} at 100 K and room temperature, together with the evaluated trap energy levels with respect to the conduction band.

Annealing Temperature T_A (°C)	$\Delta\sigma/\sigma_{Dark}$ (at 100 K)	$\Delta\sigma/\sigma_{Dark}$ (at 300 K)	E_{T_1} (meV)	E_{T_2} (meV)
As-Grown	313	156	262	491
200	52	71	298	653 (435)

According to the theory of Simmons and Taylor, temperature dependence of photoconductivity is analyzed at three temperature regions;

- ***high temperature region***, in which photo-excitation rate of carriers is suppressed by monomolecular recombination rate ($\Delta\sigma < \sigma_{Dark}$) and the maximum photoconductivity is reached as the temperature decreases down to the critical temperature T_C, and the photoconductivity can be expressed in the region as

  $$\Delta\sigma_{ht} = e\mu_n \left(\frac{G}{v\sigma_t N_t}\right) exp\left(-\frac{E_a - (E_c - E_{t2})}{kT}\right) \tag{4.32}$$

  where v is the thermal velocity of electrons, σ_t is the capture cross section corresponding to trap energy level E_{t2}, k is the Boltzmann constant. N_t is the density of trap states.

- ***moderate temperature region***, in which photoconductivity decreases as the temperature decreases with a lower activation energy than that of dark conductivity at the same temperatures, which is described by the expression

  $$\Delta\sigma_{mt} = e\mu_n \left(\frac{GN_o}{v\sigma_t N_t}\right)^{1/2} exp\left(-\frac{(E_c - E_{t1})}{2kT}\right) \tag{4.33}$$

  where N_o is a density of state value equal to both N_c and N_v which are the effective density of states in the conduction and valence band, respectively.

- ***low temperature region***, in which photoconductivity is independent of temperature but photoconductivity values are greater than those of dark conductivity as expressed by

  $$\Delta\sigma_{lt} = 2e\mu_n \left(\frac{G}{v\sigma_t N_t}\right) \tag{4.34}$$

  as described in the theory [72]. At high light intensities the value of T_C is shifted towards higher temperatures. As compared to the experimental

> data of temperature and intensity dependent photoconductivity shown in Fig. 4.23(a) and (b), the theory explains the photoconductive behavior of AIS thin films well.

The related activation energy values were calculated by using the fitting parameters of Fig. 4.23(a) and (b) and Fig. 4.30(a) and (b). The calculated values are tabulated in Table 4.13. As it is seen from the figures and table, there are two distinct activation energies for the moderate temperature region designated as E_{β_1} and E_{β_2} for all types of AIS thin films. The E_{β_2} values are almost independent of light intensity while the E_{β_1} values increases as intensity of incident light increases. Therefore, the E_{β_2} photo-activation energies can be ascribed to the recombination process governed by the localized states within bandtail near the conduction band edge. Furthermore, the E_{γ} values are almost constant as the excitation intensity increases as expected.

The excitation intensity dependence of the photoconductivity gives information on the recombination process. Hence, the recombination process may change from monomolecular to bimolecular as the excitation intensity is increased. This increase in E_{β_1} values implies that exposing the as-grown AIS thin films to the illumination increases the overall density of defect centers which causes the Fermi energy level to change, thus changes the fraction of empty defect centers [129]. At low light intensity, the observation of thermal quenching of photoconductivity over a small temperature range for as-grown AIS thin films (see Fig. 4.23(a)) and for 200°C-annealed ones (see Fig. 4.30(b)) indicates the presence of sensitizing centers together with recombination centers in the thin film structure [129]. Therefore, the activation energies at high temperature region E_{α} are calculated from the slopes of the fittings in Fig. 4.23(a) for as-grown films and in Fig. 4.30(b) for the 200°C-annealed ones since the T_C can not be observed in Fig. 4.23(b) for the light intensities used in the experiments. Additionally, the inadequate data for high temperature region in Fig. 4.30(b) prevent obtaining an activation energy. However, two possible fittings yield two different activation energy values, which are designated as E'_{α} and E''_{α} in Fig. 4.30(b), and the expected activation energy value E_α lies in between these two values as given in Table 4.13. Therefore, only an energy interval for one of the trap levels, E_{T_2}, can be determined from the data for the 200°C-annealed AIS thin films.

Moreover, the theoretical model gives the information about the energy levels of the two discrete sets of localized states in the forbidden gap by the following relations [73, 74, 130–132]

$$E_{T_1} = 2E_{\beta_1} \tag{4.35}$$

and

$$E_{T_2} = E_a + E_\alpha \tag{4.36}$$

where E_a is the dark conductivity activation energy and the trap positions E_{T_1} and E_{T_2} are defined as the energy differences between the bottom of the conduction band and the energy levels of trap positions. The calculated photoconductivity activation energies and the energy positions of the trap levels from the conduction band are tabulated in Table 4.10 and 4.14, respectively and the trap levels are illustrated for the as-grown AIS thin films in Fig. 4.28(a).

The variation of the photosensitivity ($\Delta\sigma$ / σ_{Dark}), which is a useful parameter, as a function of inverse absolute temperatures at different illumination intensities, which is shown in Fig. 4.24(a) and (b) revealed that at the low temperature region, increasing illumination intensity yields increased photoconductivity and its values are up to about 300 times larger than σ_{Dark} at the illumination intensity of 113 mW/cm^2 for as-grown thin films. On the other hand, these values can reach about 80 times the σ_{Dark} at the illumination intensity of 113 mW/cm^2 for annealed AIS thin films as given in Table 4.14. In this manner, as it can be obviously seen from the Fig. 4.24(a) and (b), as-grown AIS thin films are more photosensitive than the 200°C-annealed ones. However, as the temperature increases the ratio approaches to unity due to the remarkable increase in the concentration of thermally activated carriers relative to that of photo-excited carriers. The reason for the increasing photosensitivity at low

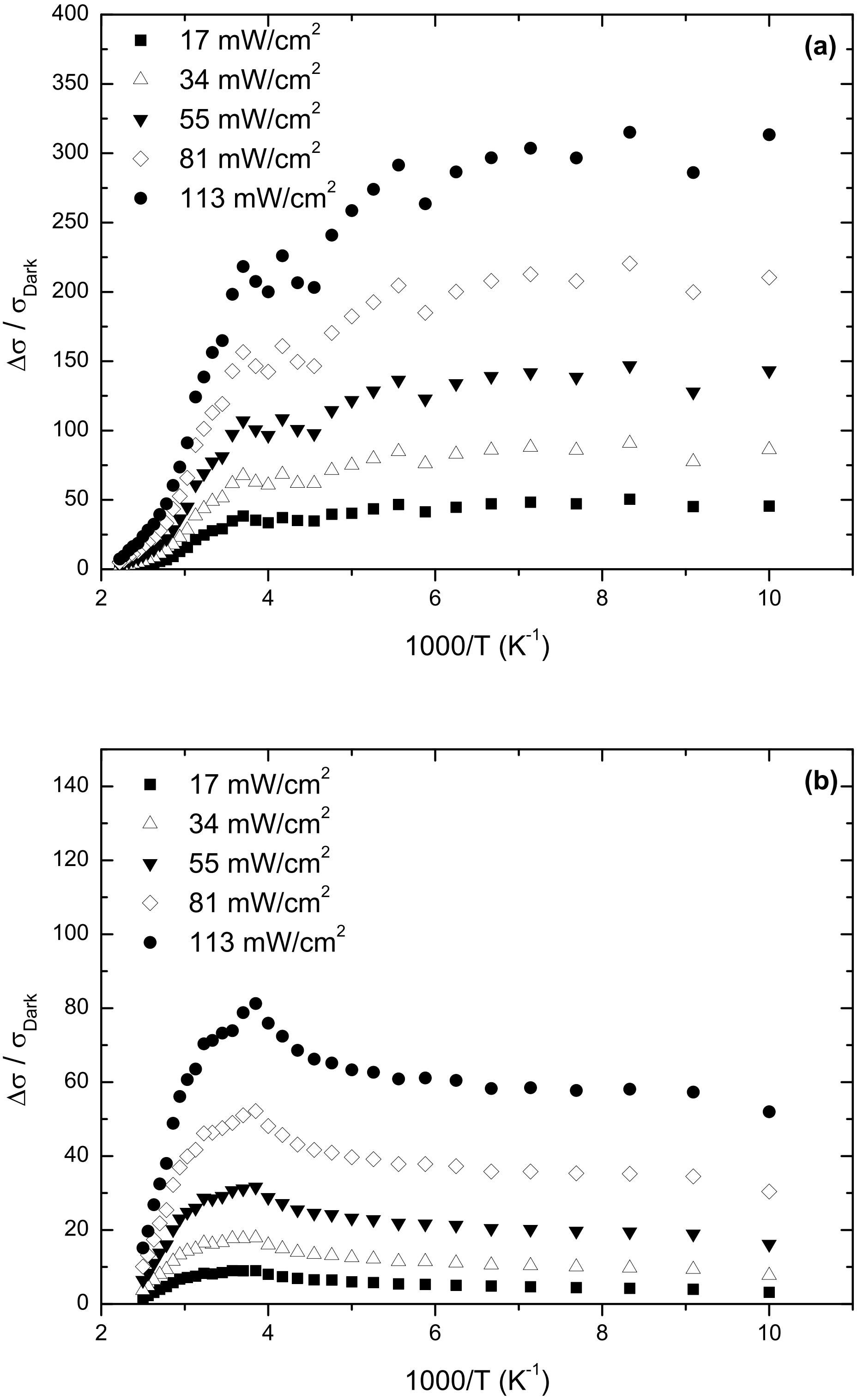

Figure 4.24: The variation of the photosensitivity as a function of inverse absolute temperature at different light intensities for (a) as-grown and (b) 200°C-annealed AIS thin films.

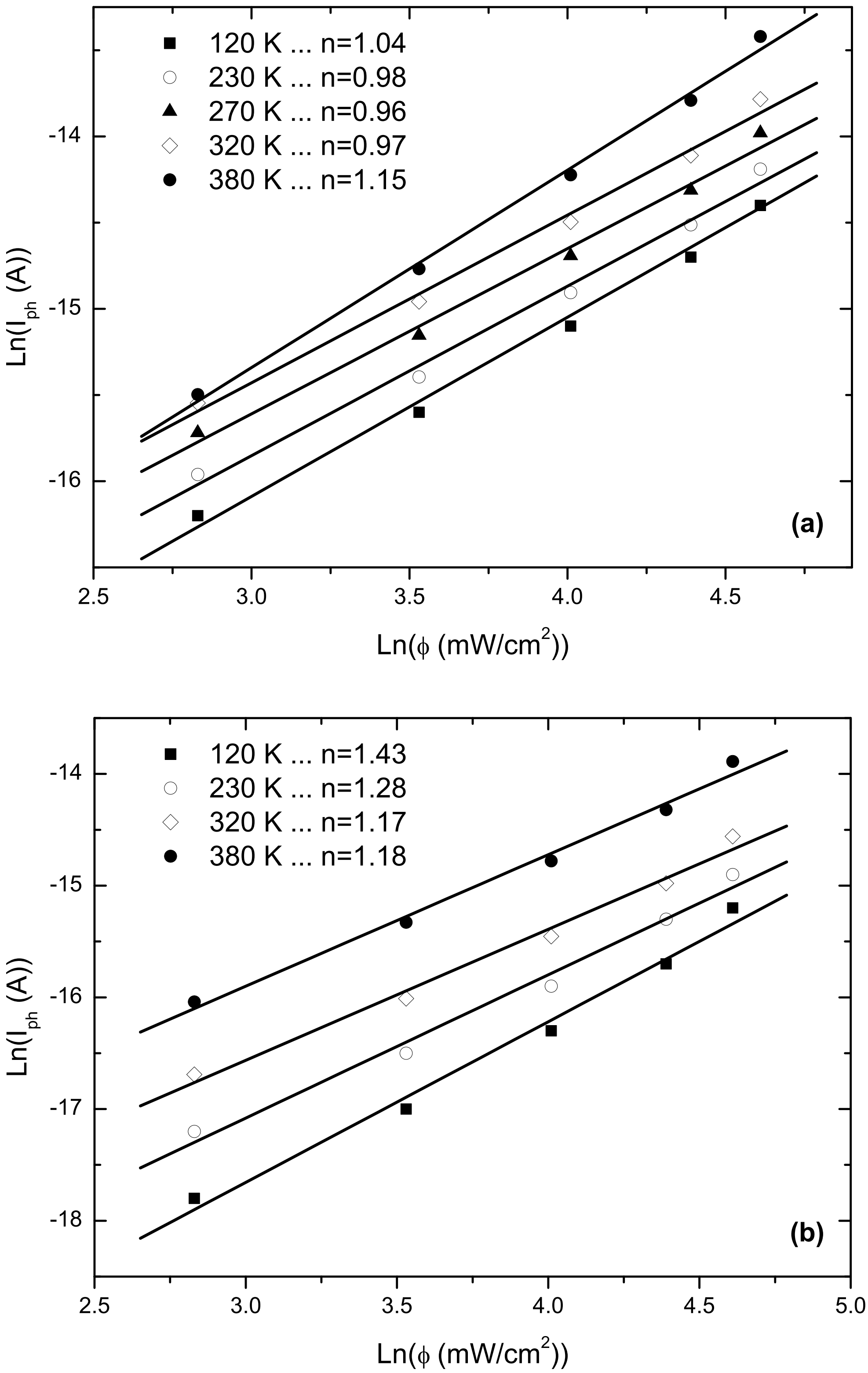

Figure 4.25: The photocurrent-illumination intensity behaviors at different temperatures for (a) as-grown and (b) 200°C-annealed AIS thin films.

temperature region is the increased probability of carriers to tunnel through the grain boundary barrier height which is reduced upon light illumination. The generated holes near the grain boundary region due to the photoexcitation might be captured by trapping centers located at the grain boundary and this causes a decrease in the energy barrier height and width [133]. Therefore, the probability of tunneling through the decreased and narrowed energy barrier for electrons becomes larger at low temperatures causing increased photosensitivity for annealed AIS thin films.

In order to determine the nature of the recombination centers, photocurrent (I_{ph})-illumination intensity (ϕ) dependencies were measured at different temperatures as another important analysis. Figure 4.25(a) and (b) indicate the plot of Ln(I_{ph}) versus Ln(ϕ) at different ambient temperatures. The relation between the photocurrent and the illumination intensity is of $I_{ph} \propto \phi^n$ type [70]. The power exponent (n) is a distinctive indicator for the determination of the nature of recombination mechanism of the non-equilibrium carriers. The calculated n values vary between 0.96 and 1.20 for various temperatures for the as-grown AIS thin films. For the 200°C-annealed AIS thin films these values vary in between 1.16 and 1.55. Increasing exponent n values with increasing temperature confirm the longer lifetimes for free carriers and stronger recombination process at the film surface. Two-center model best fits the situation when the exponent $n > 1.0$, which is formally defined as the supralinear photoconductivity. This model can explain the increase in lifetime of free carriers with increasing illumination intensity by foreseeing two-center effects [71]. Therefore, the analysis of photocurrent (I_{ph})-illumination intensity (ϕ) variation for the AIS thin films strongly supports the results obtained after the application of the theory developed by Simmons and Taylor as discussed above.

4.5.2 Temperature Dependent Spectral Photoresponse

The spectral distribution of photoconductivity is a useful and simple tool to obtain the information related to band gap energy of the AIS thin films. Figure

4.26 shows the spectral distribution of the photoconductivity values normalized to the incident number of photons for as-grown and 200°C-annealed films at 300 K with the applied electric field strength of 85 V/cm. As it is seen from figure 4.26, the normalized photocurrent spectrum has three strong peaks located at 792 nm (A), 699 nm (B) and 618 nm (C) corresponding to 1.57, 1.77 and 2.01 eV for the as-grown films, respectively. For the 200°C-annealed samples only two well-defined peaks located at 741 nm (A_A) and 656 nm (B_A) (corresponding to 1.68 and 1.89 eV) were observed. The energies of $E_A = 1.57$ eV and $E_{A_A} = 1.68$ eV correspond to the intrinsic transitions from extended valence band to conduction band for as-grown and annealed AIS thin films at 200°C, respectively. These values are in a close agreement with the results obtained from the optical transmission analysis [134] in Section 4.3.3. In addition, it can be inferred from the energy peaks corresponding to band gap energies that annealing of the AIS thin films at 200°C smears out the structural defects introduced during the growth process and causes the band gap energy to increase due to the amorphous-to-polycrystalline phase transformation as observed from XRD studies [110]. The other two peak energies represent the transitions from the splitting parts of the valence band to the conduction band. Because of the tetragonal symmetry of the crystal field and the spin-orbit interaction, the valence band splits into three energy levels [6–8]. Therefore, the maxima of the uppermost ($\Gamma_{7v}(U)$) and the lowermost ($\Gamma_{7v}(L)$) levels of the parabolic valence band are separated from the top of the mid-valence band energy (Γ_{6v}) level as seen in figure 4.28. The A, B and C symbolize the allowed direct transitions ($\Gamma_{7v}(U) - \Gamma_{6c} \Rightarrow E_A, \Gamma_{6v} - \Gamma_{6c} \Rightarrow E_B$ and $\Gamma_{7v}(L) - \Gamma_{6c} \Rightarrow E_C$, respectively) to a single conduction band from three closely separated valence bands. According to the quasicubic model, which was developed for the splitting of p-like levels in the valence band including the effects of a tetragonal crystalline field and spin-orbit interaction, the energies of the Γ_{7v} levels relative to the Γ_{6v} level in the valence band of a chalcopyrite semiconductor structure are given by [6, 7, 125]

$$E_{1,2} = -\frac{1}{2}(\Delta_{SO} + \Delta_{CF}) \pm \frac{1}{2}[(\Delta_{SO} + \Delta_{CF})^2 - \frac{8}{3}\Delta_{SO}\Delta_{CF}]^{1/2} \tag{4.37}$$

where Δ_{SO} is the spin-orbit splitting and Δ_{CF} is the crystal-field splitting of the valence bands for AIS thin films. The $E_{1,2}$ energy values correspond to the energies $E_1 = E_B - E_A$ and $E_2 = E_B - E_C$. The calculated parameters of the quasicubic model, Δ_{SO} and Δ_{CF} are in good agreement with the results obtained from the optical transmission analysis [134] in Section 4.3.3, and listed in Table 4.15. Therefore, the band gap energies of the as-grown and the 200°C-annealed AIS thin films are determined to be as 1.57 and 1.68 eV. Interestingly, for the annealed thin films, the observation of the third transition corresponding to spin-orbit splitting of the valence band could not be resolved from spectral distribution of photoresponse measurements as it was detected from optical transmission. This could be a consequence of scattering of electrons in the conduction band due to the mutual interaction among electrons [8].

Experimentally determined energy band gap values for as-grown and 200°C-annealed thin films by the spectral photoconductivity measurements have greater energy values as compared to the results of previous works on $AgInSe_2$ (1.24 eV) and $Ag_3In_5Se_9$ (1.30 eV) ternary compounds [44]. The relatively larger band gap value of the deposited thin films can be explained by the reduction in Se p-Ag d interband repulsion (p-d hybridization) due to the decrease in d nature following the formation of crowded Ag vacancies which produce ordered defect compounds of Ag-In-Se [18, 135]. Moreover, the calculated value of Δ_{CF} for the films is almost comparable with the one of $AgInSe_2$ and on the other hand Δ_{SO} value is greater than the one of $AgInSe_2$ but less than that of $Ag_3In_5Se_9$ [44] which can be considered in the light of p-d hybridization concept [135, 136].

The applied electric field strength dependencies of the photoconductivity of AIS thin films are shown in Fig. 4.27(a) and (b). Furthermore, the temperature dependence of spectral distribution of photoconductivity can be seen from Fig. 4.29 and, Fig. 4.30(a) and (b) for both as-grown and 200°C-annealed AIS thin films over the temperature range between 80 and 450 K. As observed from

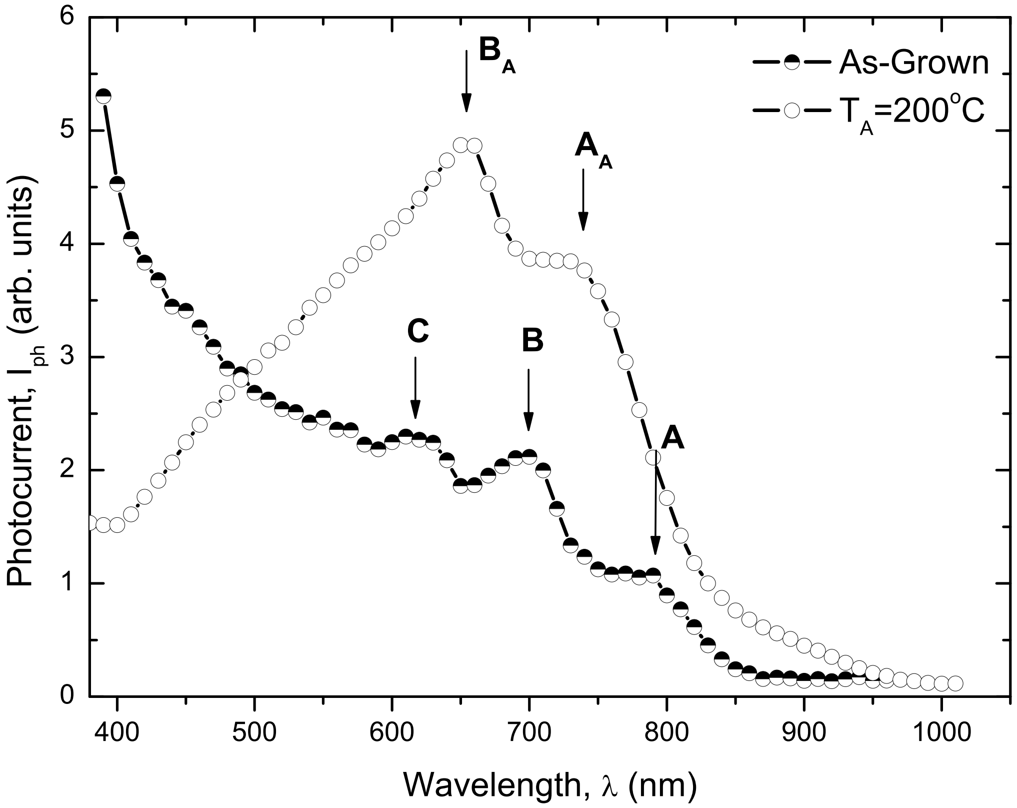

Figure 4.26: The normalized photocurrent response of the AIS thin films both as-grown and 200°C-annealed at 300 K with the applied electric field strength of 85 V/cm.

Table 4.15: The band gap energy values and the calculated parameters of the quasicubic model for as-grown AIS thin films

T (K)	E_g (eV)	E_A (eV)	E_B (eV)	E_C (eV)	-Δ_{CF} (eV)	Δ_{SO} (eV)
150	1.57	1.57	1.80	2.01	0.28	0.26
250	1.58	1.58	1.78	1.98	0.24	0.24
300	1.57	1.57	1.78	2.00	0.26	0.27
350	1.57	1.57	1.77	2.00	0.25	0.28
400	1.56	1.56	1.79	1.96	0.27	0.21

the figures, the magnitude of the photocurrent values increases as the temperature increases up to a critical temperature value T_C where the maximum value of the photocurrent is achieved in the spectral response curve then starts to de-

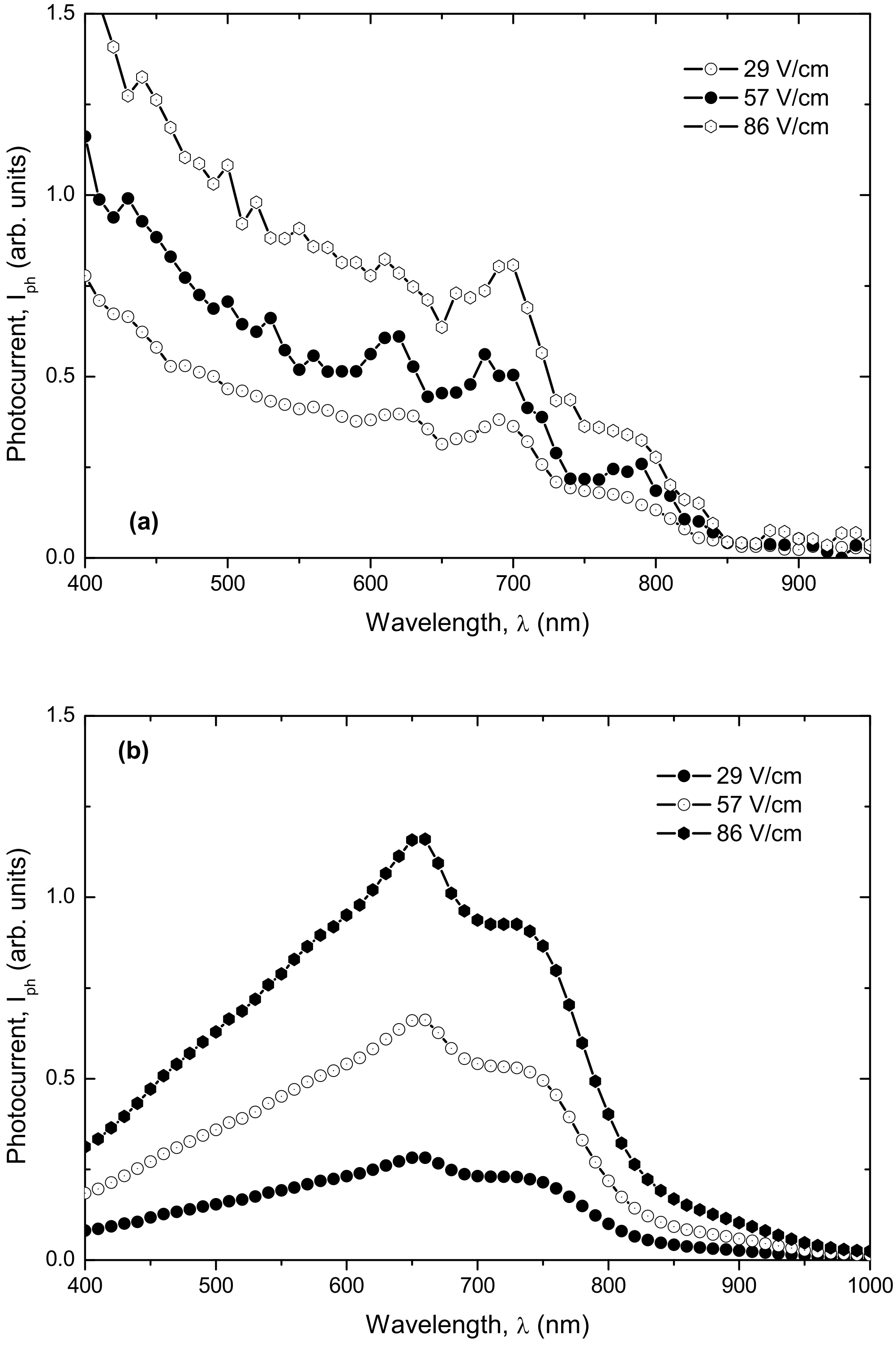

Figure 4.27: The room temperature spectral distribution of the normalized photocurrent measured under different electric field strengths for the (a) as-grown and (b) 200°C-annealed AIS thin films.

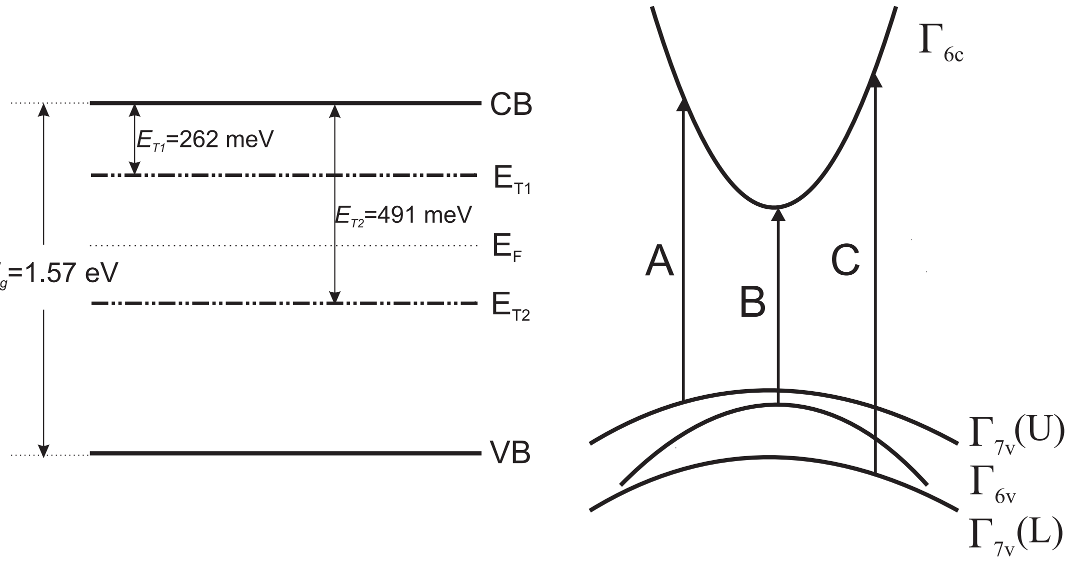

(a) (b)

Figure 4.28: (a) Energy level diagram for the two discrete traps in the forbidden energy gap of the as-grown AIS thin films and (b) energy band structure of the AIS thin films at Γ point according to allowed transitions.

crease with further increase in the ambient temperature. In other words, thermal quenching of photoconductivity phenomena is observable for both as-grown and 200°C-annealed AIS thin films. The T_C values are obtained as 350 and 380 K with the activation energies tabulated in Table 4.13 at high temperature region for as-grown and 200°C-annealed AIS thin films, respectively. The mechanism of thermal quenching of photoconductivity is defined by two energy levels related with deep recombination centers and shallow traps [71]. At fixed incident photon energy and constant illumination intensity, when the ambient temperature is increased to T_C, the minority carriers (holes in this case) are thermally reactivated to the valence band from their trapping sites producing additional free holes. Then, they recombine with free electrons in the deep recombination centers. Therefore, the lifetime of the free carriers is diminished significantly causing the photoconductivity to decrease in magnitude [70].

The band gap energy of the AIS thin films shows slight variation with the temperature and varies in between 1.57 and 1.63 eV over the temperature range

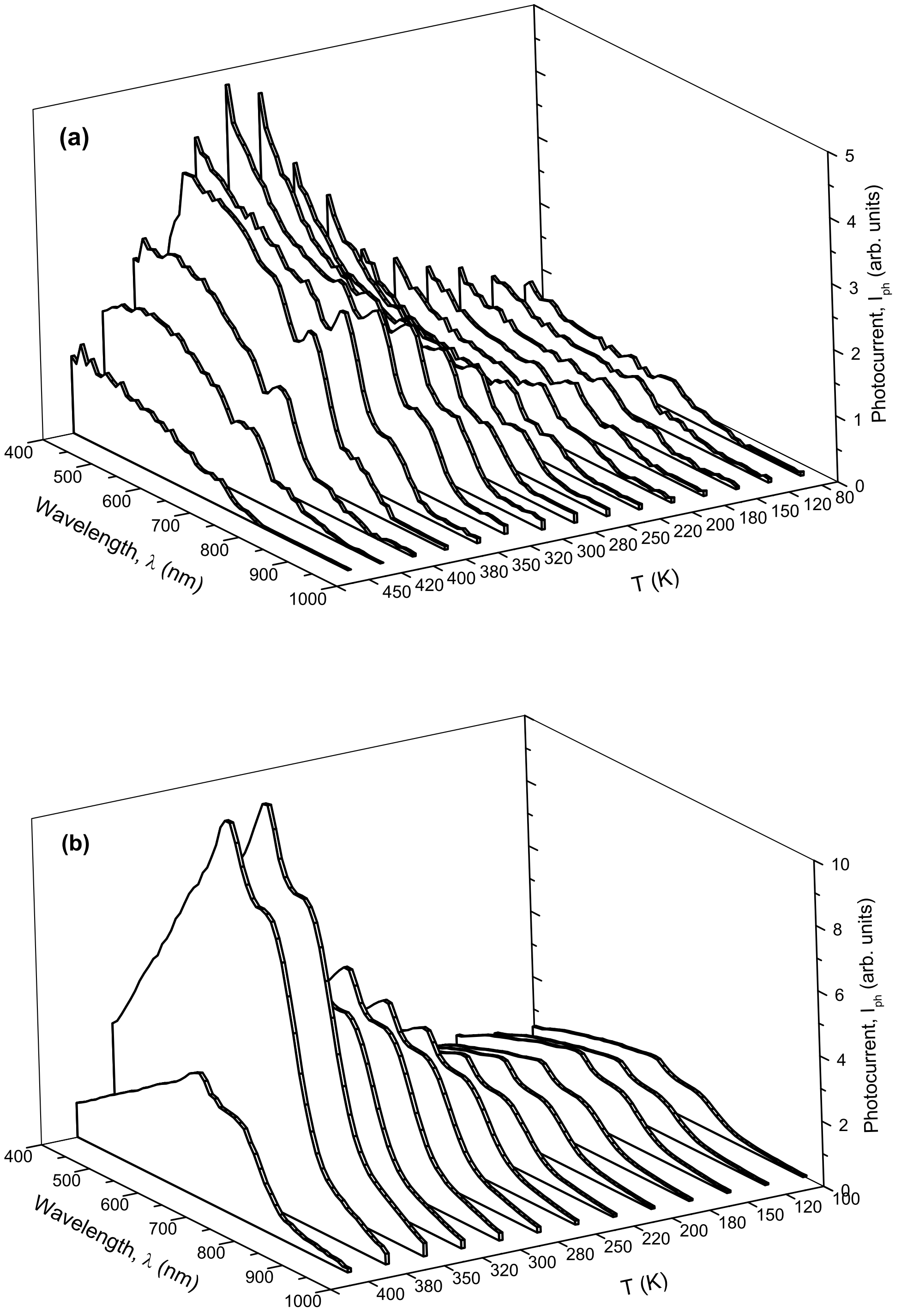

Figure 4.29: The spectral distribution of the normalized photocurrent at different temperatures ranging from 80 to 450 K for (a) as-grown and (b) 200°C-annealed AIS thin films.

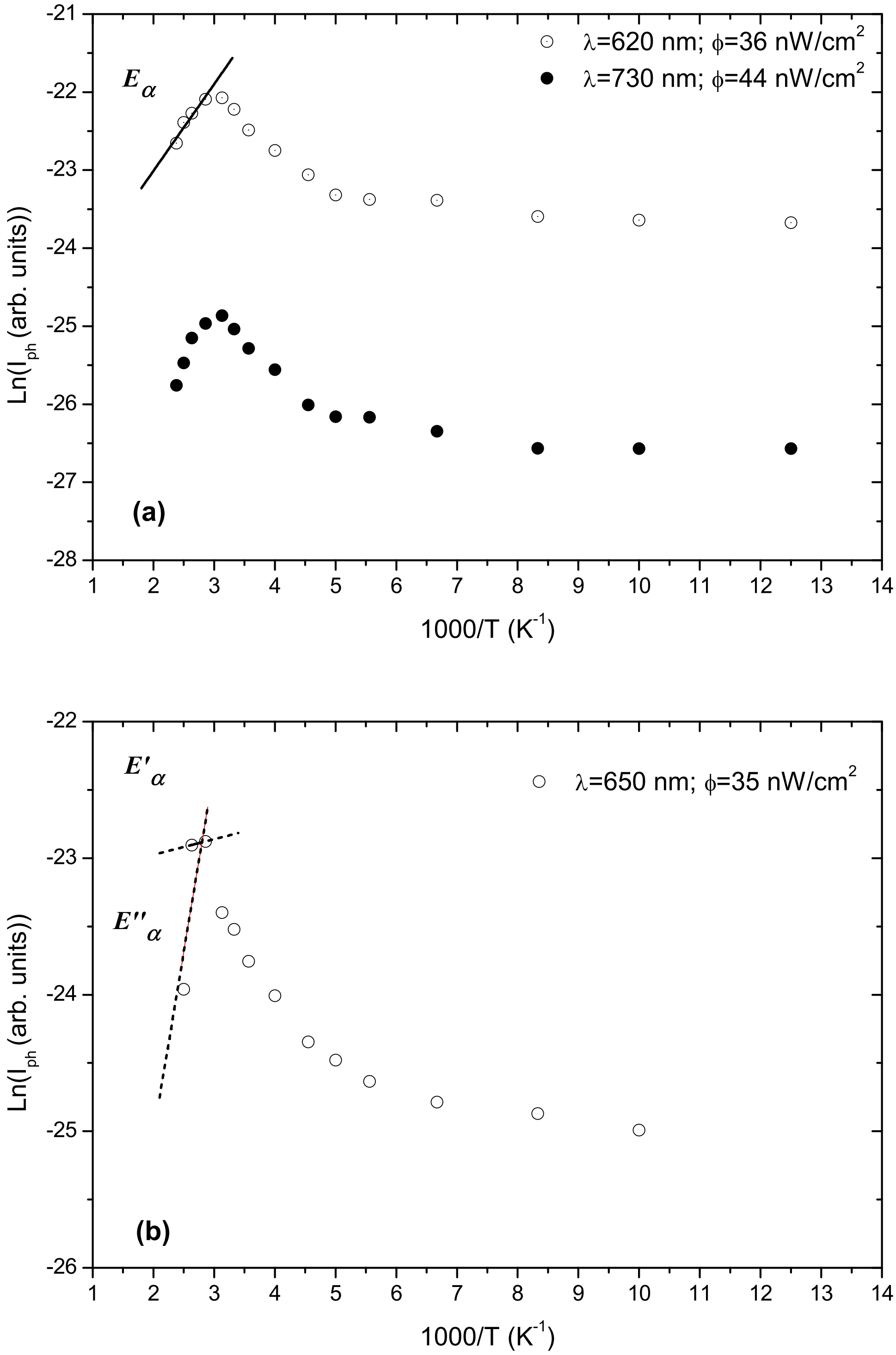

Figure 4.30: The temperature dependence of photocurrent at different excitation wavelength of incident light with given flux for the (a) as-grown and (b) 200°C-annealed AIS thin films. E_α, E'_α and E''_α are the activation energies discussed in Section 4.5.1.

of 80-450 K without any apparent correlation with temperature. For the annealed AIS thin films, the result is not so different but the values are varying in between 1.67 and 1.69 eV. This interesting result may be ascribed to the significantly wide energy width of the band tail states determined from the optical transmission analysis [134] in Section 4.3.3.

CHAPTER 5

CONCLUSIONS

The Ag-In-Se (AIS) thin films were deposited by e-beam evaporation of $Ag_3In_5Se_9$ single crystal powder under the base pressure of about 1.7×10^{-4} Pa without intentional doping and the temperature of the glass substrates was maintained constant at around 110°C during the deposition. The chemical stoichiometry of the source powder was determined as 18% Ag, 29% In and 53% Se in atomic percentages by means of EDS results and the XRD analysis revealed the tetragonal lattice structure with the main crystalline orientation along (513) direction.

As a result of the structural analysis, the as-grown AIS thin films were in amorphous phase and the polycrystalline films were obtained following to the post thermal annealing under nitrogen atmosphere at 200°C. Furthermore, the detailed analysis of the XRD results showed that the resulting polycrystalline thin film structure was composed of a mixture of different crystalline phases, such as $AgInSe_2$, In_4Se_3, InSe. The most intensive peaks in the XRD pattern of the 200°C-annealed thin films belonged to In_4Se_3, InSe and Se crystalline phases. However, the $AgInSe_2$ and $Ag_3In_5Se_9$ crystalline phases also exist according to the XRD diffractogram. As the annealing temperature was increased to 300°C, the existence of the $Ag_3In_5Se_9$, $AgInSe_2$, In_2Se_3 and InSe crystalline phases dominated the polycrystalline film structure. Further annealing the AIS thin films at 400°C resulted in the development of Se_6 and Se crystalline phases, which is an important indication of Se segregation process within the film structure since the migrated Se atoms could form localized Se aggregates in the film structure. Therefore, the annealing process implemented after the deposition of the AIS thin films caused the formation of multi-phase polycrystalline thin film structure and the increasing annealing temperature triggered the segregation of Se atoms resulting in the change in the dominant crystalline phases.

The surface atomic composition of the multi-phase AIS thin films were investigated by means of XPS analysis on as-grown and annealed samples at different temperatures. The compositional analyses were mainly focused on the In 4d, Se 3d and Ag 3d core levels, since the valuable information about the bonding states is obtainable within the valence band region in the XPS spectrum with low binding energy value. Decomposition of In 4d photoelectron peak revealed that there exist three contributions to the peak due to doublets corresponding to In-In metallic bonds, In-Se bonds and In-Ag bonds for the as-grown thin films. The existence of three different bonds formed by In atoms indicated the possibility of the formation of a multi-phase thin film structure. As a result of fitting analysis of the XPS data, it was observed that the concentration of In-In metallic bonds exceeds the other ones for the as-grown films. Annealing the AIS thin films caused a drastic decrease in the In-Se and In-Ag bond concentrations while the In-O bond concentration increases. This was also an evidence for the segregation of Se atoms as a result of post depositional annealing. The peak fitting analysis of the core levels corresponding to Se 3d and Ag 3d supported the Se segregation mechanism triggered by the increasing annealing temperature because the Se 3d photoelectron peak intensity in the XPS spectra of the AIS thin films obviously diminished as the annealing temperature was increased. Therefore, Se segregation accompanied by the relative diffusive motion of Ag atoms into the bulk film structure brought about an In-rich, but Ag- and Se-deficient thin film surface. Furthermore, the increasing roughness parameters from 1.81 to 22.89 nm with the increasing annealing temperature from 200 to 400°C were due to the Se segregation and/or re-evaporation dynamics at the thin film surfaces.

The optical transmission measurements were performed on as-grown and annealed AIS thin films at different temperatures. The refractive index dispersions for the films were calculated by means of both envelope method (EM) and continuous wavelet transform (CWT) methods and the results were found to be in good agreement with each other. In addition, the refractive index dispersions of the AIS thin films were shown to be explained by the Cauchy dispersion relation very well. Optical constants (n, k, ε) of the AIS thin films were calculated and found to be critically dependent on the post thermal annealing due to the structural changes within the AIS thin film caused by thermal energy. On the other hand, the annealing of the as-grown AIS thin films at 200°C caused the indices to drop from 4.00-4.40 to the 3.60-3.80. Moreover, the refractive indices of the annealed films at 300°C were calculated and shown to vary between 4.20 and 4.80 over the same wavelength range.

Furthermore, it was observed that the optical absorption characteristics of the AIS thin films were identified by three distinct intrinsic direct transitions from the valence band to conduction band (at 1.72, 1.82 and 2.03 eV for as-grown samples), indicating the existence of the valence band splits, which are due to spin-orbit interaction and crystal-field splitting. Therefore, the fundamental optical band gap was determined to be direct band gap with the value 1.72 eV for as-grown AIS thin films and the related parameters of the quasicubic model were calculated for the samples. The decrease in the optical band gap values with increasing annealing temperature from 1.72 to 1.61 eV despite the polycrystalline structure could be ascribed to the Se segregation causing Se vacancies at large concentrations such that the energy width of the band tail states near the valence band edge increases with increasing annealing temperature.

The effect of post-thermal annealing of the AIS thin films on the electrical and photoelectrical properties of the films was also investigated. The as-grown and the annealed AIS thin films had n-type conduction, which was determined by means of the hot-probe technique. The temperature dependent conductivity results showed that the electrical properties of the thin films strongly depended on the annealing temperature. In other words, annealing the AIS thin films at 200°C improved the conductivity, while annealing at 300°C and above temperatures resulted in the degenerate semiconductor behavior. Specifically, the room temperature conductivity value of the as-grown thin films was 1.9×10^{-6} $(\Omega \text{ cm})^{-1}$ and increased to 2.3×10^{-6}, 9.8×10^{-1}, and 5.2 $(\Omega \text{ cm})^{-1}$ as the annealing temperature increased from 200 to 400°C, respectively. The most important reason for the degenerate semiconductor behavior observed in the AIS thin films annealed at 300°C and above temperatures was the resulting In-rich but Se-deficient thin film surfaces due to the segregation and/or reevaporation of Se in the structure as the annealing temperature increased.

The nature of the recombination process and trap levels within the forbidden energy gap of both the as-grown and 200°C-annealed AIS thin films, the photoconductivity measurements were carried out as a function of temperature and illumination intensity. The temperature dependent photoconductivity measurements showed that the as-grown AIS thin films are highly photoconductive. The annealing of the thin films at 200°C reduced the photoconductive properties of the AIS thin films. At room temperature, the measured photosensitivity values were 156 and 71 for as-grown and 200°C-annealed AIS thin films, respectively.

The power exponent n in the relation $I_{ph} \propto \phi^n$ which represents the dependence of the photocurrent on the illumination intensity was calculated and found to have values lying in between 0.96 and 1.15 for the as-grown thin films, and 1.17 and 1.43 for the 200°C-annealed thin films. In other words, the power exponent values were observed to be $n > 1.00$ which is the formal definition of the supralinear photoconductivity. Moreover, the thermal quenching of the photoconductivity was observed for both types of the films which was observed as a decrease in photoconductivity above corresponding critical temperatures. As a conclusion, the simultaneous observation of the thermal quenching and the supralinear photoconductivity proved the existence of two distinct recombination centers in the forbidden energy gaps of the two kinds of AIS thin films. The energy levels of two trap levels were determined from the calculated activation energies of the temperature dependent photoconductivity data as 262 and 491 meV from the bottom of the conduction band for the as-grown AIS thin films. The first deduced trap level of the 200°C-annealed AIS thin films had the value of 298 meV. However, due to the inadequacy of the data set at the thermal quenching region of the photoconductivity variation as a function of temperature, the activation energy calculation was performed by means of two possible fittings of the data. Therefore, the second trap level was found to be in between 435 and 653 meV for the annealed thin films.

The spectral distribution of the photoconductivity exhibited three strong peaks located at 1.57, 1.77 and 2.01 eV for as-grown thin films and two peaks located at 1.68 and 1.89 eV for 200°C-annealed AIS thin films at room temperature. These first energy values were very close to the values of 1.72 and 1.71 eV obtained from the optical transmission analysis and the differences between the results arise from the wide energy distribution of the valence band tail states into the band gap due to amorphous structure. The energy values of 1.57 and 1.68 eV correspond to the band gap energies of as-grown and annealed thin films, respectively. The other energy values are associated with the crystal field splitting, Δ_{CF}, and spin-orbit splitting (Δ_{SO}) of the valence band, which is related with the splitting of the *p*-like levels in the valence band including the effects of a tetragonal crystalline field and spin-orbit interaction according to the quasicubic model. -(Δ_{CF}) and (Δ_{SO}) values are in the range of 0.28-0.24 eV and 0.24-0.28 eV in the studied temperature range, respectively. Moreover, the thermal quenching of photoconductivity was also confirmed by the variation of photoconductivity with temperature at fixed wavelengths of incident light and fixed illumination intensity.

Both types of AIS thin films exhibited the photoresponse to the light exposure having the wavelength values lying in between 400 and 900 nm. However, in the wavelength range of 500-850 nm, an effective spectral photoresponse behavior was observed for the as-grown and 200°C-annealed AIS thin films.

In this study, the Ag-In-Se thin films were shown to be a promising semiconductor material for the solar cell applications with their reasonable band gap values near the solar spectrum maximum, their high absorption coefficient values, their satisfactorily high photoconductivity values, their room temperature conductivity values and their photoresponse wavelength region which almost matches the high intensity region of the spectral irradiance distribution of the sun. Although the implementation of the post-annealing process improved the structural, optical, electrical and electrooptical properties of the e-beam deposited AIS thin films, there are major problems preventing to produce a polycrystalline, single phase ternary semiconductor thin films. These problems and the possible solution can be summarized as follows;

- the inadequate Ag content incorporated to the thin film structure during the e-beam deposition of AIS thin films from the $Ag_3In_5Se_9$ single crystal source. Due to the low Ag content in the AIS thin film structure, the formation of Ag containing ordered compounds were observed. In addition, the multi-phase structure of the deposited films were resulted from the low Ag content together with segregation of Se atoms at high annealing temperatures. Moreover, the production of a ternary chalcopyrite semiconductor thin film can be maintained by the incorporation of the stoichiometrically required amount of Ag content into the thin film structure. If this condition is met the band gap of the ternary chalcopyrite thin films will be smaller than the calculated ones of the deposited AIS thin films and the n-type electrical conductivity will turn into p-type. The problem arises mostly due to the decomposition of the source crystal powder into separate phases before the evaporation which is commonly encountered during thin film deposition by thermal evaporation technique. As an alternative deposition procedure can be developed by evaporation of Ag metal layers sandwiched between the thin film layers of e-beam evaporated $Ag_3In_5Se_9$ single crystal powder in order to obtain stoichiometric ternary semiconductor thin films.

- segregation and/or reevaporation of Se atoms in the film structure at high annealing temperatures. The requirement of the post-annealing of the as-deposited AIS thin films was demonstrated in this study in order to obtain a polycrystalline AIS thin films. However, segregation of Se prevented the annealing temperature to increase above a certain value. Otherwise, the resulting thin film structure will have a degenerate electrical property and a multi-phase structure including the undesired chemical phases. In order to prevent the segregation of Se atoms, the deposited thin films should be annealed under the Se vapor atmosphere. This atmosphere can be prepared by several methods. The thin films can be selenized by heating them to keep the temperature at or above 400°C in presence of H_2Se gas. As a result, the post-annealing process is required to obtain a polycrystalline AIS thin films, but selenization of the films is also the indispensable post-depositional process. The maximum annealing temperature that can be reached for the e-beam deposited AIS thin films without selenization is determined to be as 200°C in order to obtain polycrystalline and structurally, optically and electrically optimized thin films.

REFERENCES

[1] D. W. Aitken, L. Billman, and S. R. Bull *Renewable Energy World*, vol. 7, p. 56, 2004.

[2] J. Poortmans and V. Arkhipov, *Thin Film Solar Cells: Fabrication, Characterization and Applications.* John Wiley and Sons, 2006.

[3] S. Willoughby *Nature*, p. 303, 1873.

[4] D. M. Chapin, C. S. Fuller, and G. L. Pearson *J. Appl. Phys.*, vol. 25, p. 676, 1954.

[5] K. L. Chopra, P. D. Paulson, and V. Dutta *Prog. Photov. Res. Appl.*, vol. 12, p. 69, 2004.

[6] J. L. Shay and J. H. Wernick, *Ternary Chalcopyrite Semiconductors: Growth, Electronic Properties, and Applications.* Pergamon Press, 1975.

[7] U. N. Roy, Y. Cui, R. Hawrami, A. Burger, L. Orona, and J. Goldstein *Solid State Commun.*, vol. 139, p. 527, 2006.

[8] S. H. You, K. J. Hong, T. S. Jeong, C. J. Youn, J. S. Park, D. C. Shin, and J. D. Moon *J. Appl. Phys.*, vol. 95, p. 4042, 2004.

[9] P. G. Schunemann, S. D. Setzler, T. M. Pollak, M. C. Ohmer, J. T. Goldstein, and D. E. Zelmon *J. Cryst. Growth*, vol. 211, p. 242, 2000.

[10] L. I. Berger and V. D. Prochukhan, *Ternary Diamond-Like Semiconductors.* New York: Consultants Bureau, 1969.

[11] V. I. Tagirov, N. F. Gakhramanov, A. G. Guseinov, F. M. Aliev, and G. G. Guseinov *Kristallografiya*, vol. 25, p. 411, 1978.

[12] H. Neumann *Cryst. Res. Technol.*, vol. 39, p. 939, 2004.

[13] Y. S. Murthy, O. M. Hussain, B. S. Naidu, and P. J. Reddy *Mater. Lett.*, vol. 10, p. 504, 1991.

[14] P. P. Ramesh, O. M. Hussain, S. Uthanna, B. S. Naidu, and P. J. Reddy *Mater. Lett.*, vol. 34, p. 217, 1998.

[15] G. H. Chandra, O. M. Hussain, S. Uthanna, and B. S. Naidu *Mater. Sci. and Engineering B: Sol. State Mater. Adv. Tech.*, vol. 86, p. 60, 2001.

[16] B. M. Başol, A. Halani, C. Laidholm, G. Norsworthy, V. K. Kapur, A. Swartzlander, and R. Matson *Prog. Photovolt. Res. Appl.*, vol. 8, p. 227, 2000.

[17] L. L. Kazmerski, F. White, and G. Morgan *Appl. Phys. Lett.*, vol. 29, p. 268, 1976.

[18] S. B. Zhang, S.-H. Wei, and A. Zunger *Phys. Rev. B*, vol. 57, p. 9642, 1998.

[19] M. A. Contreras, K. Ramanathan, J. Abushama, F. Hasoon, J. Keane, D. L. Young, B. Egaas, and R. Noufi *Prog. Photov. Res. Appl.*, vol. 13, p. 209, 2005.

[20] B. J. Stanbery *Crit. Rev. Sol. Stat. Mater. Sci.*, vol. 27, p. 73, 2002.

[21] M. R. A. Bhuiyan and S. M. F. Hasan *J. Phys. D: Appl. Phys.*, vol. 39, p. 4935, 2006.

[22] K. Yamada, N. Hoshino, and T. Nakada *Sci. Tecnol Advanced Mater.*, vol. 7, p. 42, 2006.

[23] B. Tell, T. J. Shary, and M. H. Kasper *J. Appl. Phys.*, vol. 43, p. 2469, 1972.

[24] P. P. Ramesh, M. O. Hussain, S. Uthanna, S. B. Naidu, and J. P. Reddy *Mater. Lett.*, vol. 34, p. 27, 1997.

[25] H. Mustafa, D. Hunter, A. Pradhan, U. Roy, Y. Cui, and A. Burger *Thin Solid Films*, vol. 515, p. 7001, 2007.

[26] M. Kemell, M. Ritala, and M. Leskela *Crit. Rev. in Solid State and Mater. Sci.*, vol. 30, p. 1, 2005.

[27] T. Markvart and L. Castaner, "Principle of Solar Cell Operation," in *Solar Cells: Materials, Manufacture and Operation*, Elsevier, 2005.

[28] R. Klenk and M. C. Lux-Steiner, "Chalcopyrite Based Solar Cells," in *Thin Film Solar Cells: Fabrication, Characterization and Applications*, John Wiley and Sons, 2006.

[29] H. J. Möller, *Semiconductors for Solar Cells.* Boston: Artech House, 1993.

[30] N. A. Goryunova, *The Chemistry of Diamond-Like Semconductors.* Cambridge: MIT Press, 1965.

[31] L. S. Lerner *J. Phys. Chem. Solids*, vol. 27, p. 1, 1966.

[32] H. Hahn, G. Frank, W. Klinger, A. Meyer, and G. Störger *Z. Anorg. Chem.*, vol. 271, p. 153, 1953.

[33] J. L. Shay, B. Tell, H. M. Kasper, and L. M. Schiavone *Phys. Rev. B*, vol. 5, p. 5003, 1972.

[34] J. L. Shay and H. M. Kasper *Phys. Rev. Lett.*, vol. 29, p. 1162, 1972.

[35] J. L. Shay and B. Tell *Surf. Sci.*, vol. 37, p. 748, 1973.

[36] J. L. Shay, B. Tell, H. M. Kasper, and L. M. Schiavone *Phys. Rev. B*, vol. 7, p. 4485, 1973.

[37] B. Tell, J. L. Shay, and H. M. Kasper *Phys. Rev. B*, vol. 4, p. 2463, 1971.

[38] B. Tell, J. L. Shay, and H. M. Kasper *Phys. Rev. B*, vol. 6, p. 3008, 1972.

[39] V. I. Tagirov, N. F. Gakhramanov, A. G. Guseinov, and F. M. Aliev *Fiz. Tekh. Poluprovodn.*, vol. 14, p. 1403, 1980.

[40] V. I. Tagirov, A. G. Guseinov, N. F. Gakhramanov, and F. M. Aliev *Fiz. Tekh. Poluprovodn.*, vol. 17, p. 524, 1983.

[41] M. Parlak, Ç. Erçelebi, I. Günal, H. Özkan, and N. M. Gasanly *Cryst. Res. Technol.*, vol. 6, p. 923, 1998.

[42] A. G. Guseinov, V. I. Tagirov, and M. B. Dzhafarov *Zh. Tekh. Fiz.*, vol. 60, p. 190, 1990.

[43] Y. Watanabe, S. Kaneko, H. Kawazoe, and M. Yamane *Phys. Review B*, vol. 40, p. 3133, 1989.

[44] A. H. Huseynov and R. M. Mamedov *Semiconductor Physics, Quantum Electronics and Optoelectronics*, vol. 9, p. 25, 2006.

[45] S. Ozaki and S. Adachi *Phys. Stat. Sol. (a)*, vol. 203, p. 2919, 2006.

[46] W. C. Tan, K. Koughia, J. Singh, and S. Kasap, "Fundamental Optical Properties of Materials," in *Optical Properties of Condensed Matter and Applications*, John Wiley and Sons, 2006.

[47] J. I. Pankove, *Optical Processes in Semiconductors.* New Jersey: Prentice Hall, 1971.

[48] F. Urbach *Phys. Rev.*, vol. 92, p. 1324, 1953.

[49] G. Cody *Semiconductors and Semimetals B*, vol. 21, p. 11, 1984.

[50] S. Abe and Y. Toyozawa *J. Phys. Soc. Jpn.*, vol. 50, p. 2185, 1981.

[51] J. Singleton, *Band Theory and Electronic Properties of Solids.* New York: Oxford University Press, 2001.

[52] I. Zvyagin, "Charge Transport via Delocalized States," in *Charge Transport in Disordered Solids with Applications in Electronics*, John Wiley and Sons, 2006.

[53] B. L. Mattes, "Growth and Structure of Amorphous and Polycrystalline Thin Films," in *Polycrystalline and Amorphous Thin Films and Devices*, London: Academic Press, 1980.

[54] J. Orton, *The Story of Semiconductors.* New York: Oxford University Press, 2006.

[55] J. Volger *Phys. Rev.*, vol. 9, p. 1023, 1950.

[56] R. L. Petritz *Phys. Rev.*, vol. 104, p. 1508, 1956.

[57] H. Berger *Phys. Status Solidi*, vol. 1, p. 739, 1961.

[58] J. Y. W. Seto *J. Appl. Phys.*, vol. 46(12), p. 5247, 1975.

[59] L. L. Kazmerski, "Electrical Properties of Polycrystalline Semiconductor Thin Films," in *Polycrystalline and Amorphous Thin Films and Devices*, p. 84, London: Academic Press, 1980.

[60] C. Seager and G. Pike *J. Appl. Phys. Lett.*, vol. 40, p. 471, 1982.

[61] M. V. Garcia-Cuenca, J. L. Morenza, and J. Estevez *J. Appl. Phys.*, vol. 56, p. 1738, 1984.

[62] J. Simmons *J. Appl. Phys.*, vol. 34, p. 1793, 1963.

[63] R. H. Bube, *Electrons in Solids: An Introductory Survey.* San Diego: Academic Press, 1992.

[64] S. Baranovski and O. Rubel, "Description of Charge Transport in Amorphous Semiconductors," in *Charge Transport in Disordered Solids with Applications in Electronics*, John Wiley and Sons, 2006.

[65] A. Miller and E. Abrahams *Phys. Rev.*, vol. 120, p. 745, 1960.

[66] B. I. Shklovskii and A. L. Efros, *Electronic Properties of Doped Semiconductors.* Heidelberg: Springer, 1984.

[67] N. F. Mott and E. A. Davis, *Electronic Processes in Non-Crystalline Materials.* Oxford: Clarendon Press, 1979.

[68] C. Seager and G. Pike *Phys. Rev. B*, vol. 10, p. 1435, 1974.

[69] J. I. Pankove, *Semiconductors and Semimetals.* New York: Academic Press, 1984.

[70] R. H. Bube, *Photoelectronic Properties of Semiconductors.* New York: Cambridge University Press, 1992.

[71] R. H. Bube, *Photoconductivity of Solids.* New York: Wiley, 1960.

[72] J. G. Simmons and G. W. Taylor *J. Phys. C: Solid State Phys.*, vol. 6, p. 3706, 1973.

[73] J. G. Simmons and G. W. Taylor *J. Phys. C: Solid State Phys.*, vol. 7, p. 3051, 1974.

[74] N. Qamhieh and G. J. Adriaenssens *J. Non-Cryst. Solids*, vol. 292, p. 80, 2001.

[75] A. A. R. Elshabini-Riad and F. D. Barlow, "Properties of Thin Film Materials," in *Thin Film Technology Handbook*, New York: McGraw-Hill, 1997.

[76] D. M. Mattox, *Handbook of Physical Vapor Deposition (PVD) Processing.* New Jersey: Noyes Publications, 1998.

[77] A. A. R. Elshabini-Riad and F. D. Barlow, "Film Deposition Techniques and Processes," in *Thin Film Technology Handbook*, New York: McGraw-Hill, 1997.

[78] R. C. Jaeger, *Introduction to Microelectronic Fabrication.* New Jersey: Prentice Hall, 2002.

[79] D. K. Schroder, *Semiconductor Material and Device Characterization.* New York: Wiley, 1998.

[80] A. A. R. Elshabini-Riad and F. D. Barlow, "Characterization of Semiconductor Thin Films," in *Thin Film Technology Handbook*, New York: McGraw-Hill, 1997.

[81] L. J. van der Pauw *Philips Research Reports*, vol. 13, p. 1, 1958.

[82] A. S. F76-86, *Standard Test Methods for Measuring Resistivity and Hall Coefficient and Determining Hall Mobility in Single-Crystal Semiconductors.* PA: ASTM International, 2002.

[83] P. D. F. Joint Committee on Powder Diffraction Standards, "ASTM, Philadelphia, PA, Card 75-0118, Card 83-0039, Card 72-1470, Card 71-0354, Card 89-1516 and Card 27-0603, respectively," 2000.

[84] S. K. Biswas, S. Chaudhuri, and A. Choudhury *Phys. Stat. Sol. (a)*, vol. 105, p. 467, 1988.

[85] A. G. Fitzgerald *Thin Solid Films*, vol. 13, p. S5, 1977.

[86] T. Çolakoğlu and M. Parlak *Thin Solid Films*, vol. 492, p. 52, 2005.

[87] L. I. Berger and V. D. Prochukhan, *Ternary Diamond-Like Semiconductors.* New York: Consultants Bureau, 1969.

[88] S. Tougaard *Phys. Rev. B*, vol. 34, p. 6779, 1986.

[89] Y. Y. Peter and M. Cardona, *Fundamentals of Semiconductors.* Springer-Werlag, 2001.

[90] R. A. Pollak, S. P. Kowalczyk, L. Ley, and D. A. Shirley *Phys. Rev. Lett.*, vol. 29, p. 274, 1972.

[91] I. Miyake, T. Tanpo, and C. Tatsuyama *Jpn. J. Appl. Phys.*, vol. 23, p. 172, 1984.

[92] V. Brinzari, G. Korotcenkov, and V. Matolin *Appl. Surf. Sci.*, vol. 243, p. 335, 2005.

[93] D. Cahen, P. J. Ireland, L. L. Kazmerski, and F. A. Thiel *J. Appl. Phys.*, vol. 57, p. 4761, 1985.

[94] C. Clareso, V. Grasso, and L. Silipigni *Appl. Surf. Sci.*, vol. 171, p. 306, 2001.

[95] H. E. Maliki, S. Marsillac, J. C. Bernede, E. Faulques, and J. Wery *J. Phys.:Condens. Matter*, vol. 13, p. 1839, 2001.

[96] B. Canava, J. Vigneron, A. Etcheberry, J. F. Guillemoles, and D. Lincot *Appl. Surf. Sci.*, vol. 202, p. 8, 2002.

[97] O. A. Balitskii and W. Jaegermann *Mater. Chem. and Phys.*, vol. 97, p. 98, 2006.

[98] P. V. Galiy, A. V. Musyanovych, and Y. M. Fiyala *Physica E*, vol. 35, p. 88, 2006.

[99] J. S. Hammond, S. W. Gaarenstroom, and N. Winograd *Anal. Chem.*, vol. 47, p. 2194, 1975.

[100] S. Zembutsu *App. Phys. Lett.*, vol. 39, p. 969, 1981.

[101] S. W. Gaarenstroom and N. Winograd *J. Chem. Phys.*, vol. 67, p. 3500, 1977.

[102] H. Jain, A. Kovalskiy, and A. Miller *J. Non-Cryst. Solids*, vol. 352, p. 562, 2006.

[103] M. Mitkova, M. N. Kozicki, H. C. Kim, and T. L. Alford *Thin Solid Films*, vol. 449, p. 248, 2004.

[104] T. Wagner, A. Mackova, V. Perina, E. Rauhala, A. Seppala, S. O. Kasap, M. Frumar, M. Vlcek, and M. Vlcek *J. Non-Cryst. Solids*, vol. 299–302, p. 1028, 2002.

[105] T. Ueno and A. Odajima *Jpn. J. Appl. Phys.*, vol. 20, p. L501, 1981.

[106] E. Çetinörgü, S. Goldsmith, Y. Rosenberg, and R. L. Boxman *J. Non-Cryst. Solids*, vol. 353, p. 2595, 2007.

[107] L. C. Leu, D. P. Norton, G. E. Jellison, V. Selvamanickam, and X. Xiong *Thin Solid Films*, vol. 515, p. 6938, 2007.

[108] J. Gutwirth, T. Wagner, P. Bezdicka, M. Vlcek, S. O. Kasap, and M. Frumar *J. Non-Cryst. Solids*, vol. 353, p. 1431, 2007.

[109] F. Lai, L. Lin, R. Gai, Y. Lin, and Z. Huang *Thin Solid Films*, vol. 515, p. 7387, 2007.

[110] T. Çolakoğlu and M. Parlak *Appl. Surf. Sci.*, vol. 254, p. 1569, 2008.

[111] C. Kittel, *Introduction to Solid State Physics.* New York: Wiley, 1986.

[112] J. C. Manifacier, J. Gasiot, and J. P. Fillard *J. Phys. E: Sci. Intrum.*, vol. 9, p. 1002, 1976.

[113] R. Swanepoel *J. Phys. E: Sci. Instrum.*, vol. 16, p. 1214, 1983.

[114] R. Swanepoel *J. Phys. E: Sci. Instrum.*, vol. 17, p. 896, 1984.

[115] S. Özder, O. Koysal, S. E. San, and F. N. Ecevit *Thin Solid Films*, vol. 458, p. 257, 2004.

[116] O. Koysal, S. E. San, S. Özder, and F. N. Ecevit *Meas. Sci. Technol.*, vol. 14, p. 790, 2003.

[117] A. Grossman and J. Morlet *SIAM J. Math. Anal.*, vol. 15, p. 723, 1984.

[118] G. K. L. Goh, C. P. K. Liew, J. Kim, and T. J. White *J. Cryst. Growth*, vol. 291, p. 94, 2006.

[119] A. M. Nasr, H. I. A. El-Kader, and M. Farhat *Thin Solid Films*, vol. 515, p. 1758, 2006.

[120] M. Fox, *Optical Properties of Solids.* London: Oxford University Press, 2001.

[121] S. Adachi, *Optical Properties of Crystalline and Amorphous Semiconductors: Materials and Fundamental Principles.* Boston: Kluwer Academic Publishers, 1999.

[122] S. H. Wemple and M. DiDomenico *Phys. Rev. B*, vol. 3, p. 1338, 1971.

[123] T. Çolakoğlu and M. Parlak *J. Phys. D: Appl. Phys.*, vol. 42, p. 035416, 2009.

[124] A. H. Clark, "Optical Properties of Polycrystalline Semiconductor Films," in *Polycrystalline and Amorphous Thin Films and Devices*, London: Academic Press, 1980.

[125] V. V. Kindyak, A. S. Kindyak, V. F. Gremenok, and I. A. Victorov *Thin Solid Films*, vol. 293, p. 75, 1997.

[126] J. Kokaj and A. E. Rakhshani *J. Phys. D: Appl. Phys.*, vol. 37, p. 1970, 2004.

[127] D. V. K. Sastry and P. J. Reddy *Thin Solid Films*, vol. 105, p. 139, 1983.

[128] R. A. Street and N. F. Mott *Phys. Rev. Lett.*, vol. 35, p. 1293, 1975.

[129] D. Redfield and R. H. Bube, *Photoinduced Defects in Semiconductors.* New York: Cambridge University Press, 1996.

[130] A. Thakur, V. Sharma, G. S. S. Saini, N. Goyal, and S. K. Tripathi *J. Phys. D: Appl. Phys.*, vol. 38, p. 1959, 2005.

[131] N. Suri, K. S. Bindra, and R. Thangaraj *J. Phys. D: Appl. Phys.*, vol. 18, p. 9129, 2006.

[132] T. Çolakoğlu, M. Parlak, M. Kulakci, and R. Turan *J. Phys. D: Appl. Phys.*, vol. 41, p. 115308, 2008.

[133] R. R. Philip, B. Paradeep, and T. Shripathi *Appl. Surf. Sci.*, vol. 250, p. 216, 2005.

[134] T. Çolakoğlu, M. Parlak, and S. Özder *J. Non-Cryst. Solids*, vol. 354, p. 3630, 2008.

[135] J. R. Tuttle, D. Albin, R. J. Matson, and R. Noufi *J. Appl. Phys.*, vol. 66, p. 4408, 1989.

[136] R. R. Philip and B. Pradeep *Thin Solid Films*, vol. 472, p. 136, 2005.

VITA

PERSONAL INFORMATION

Surname, Name: Çolakoğlu, Tahir
Nationality: Turkish (TC)
Date and Place of Birth: 26 January 1979, İzmir
Marital Status: Married
Phone: +90 312 210 43 29
Fax: +90 312 210 50 99
email: cetahir@gmail.com

EDUCATION

Degree	**Institution**	**Year of Graduation**
MS	METU Physics	2003
BS	METU Physics Education	2001

WORK EXPERIENCE

Year	**Place**	**Enrollment**
2001-2008	METU Department of Physics	Teaching and Research Assistant

FOREIGN LANGUAGES

Advanced English

PUBLICATIONS

1. **T. Çolakoğlu**, M. Parlak, "*Electrical and photoelectrical properties of Ag-In-Se thin films evaporated by e-beam technique*", Journal of Physics D: Applied Physics, **42**, 035416, (2009).

2. E. Bacaksiz, M. Tomakin, M. Altunbaş, M. Parlak, **T. Çolakoğlu**, "*Structural, optical and magnetic properties of* $Cd_{1-x}Co_xS$ *thin films prepared by spray pyrolysis*", Physica B, **403**, 3740, (2008).

3. **T. Çolakoğlu**, M. Parlak, M. Kulakci, R. Turan, "*Effect of boron implantation on the electrical and photoelectrical properties of e-beam deposited Ag-In-Se thin films*", Journal of Physics D: Applied Physics, **41**, 115308, (2008).

4. **T. Çolakoğlu**, M. Parlak, S. Özder, "*Investigation of optical parameters of Ag-In-Se thin films deposited by e-beam technique*", Journal of Non-Crystalline Solids, **354**, 3630, (2008).

5. **T. Çolakoğlu**, M. Parlak, "*Structural characterization of polycrystalline Ag-In-Se thin films deposited by e-beam technique*", Applied Surface Science, **254**, 1569, (2008).

6. **T. Çolakoğlu**, M. Parlak, "*Anisotropic behaviors in polycrystalline Cd-doped GaSe thin films*", Journal of Materials Science: Materials in Electronics, **17**, 1017, (2006).

7. **T. Çolakoğlu**, M. Parlak, "*Effect of Cd-doping level on the electrical, structural and photoconductivity properties of GaSe thin films*", Thin Solid Films, **492**, 52, (2005).